5-28-2009

The Neuron-Silicon Carbide Interface: Biocompatibility Study and BMI Device Development

Christopher L. Frewin
University of South Florida

The Neuron-Silicon Carbide Interface: Biocompatibility Study and BMI Device Development

by

Christopher L. Frewin

A dissertation submitted in partial fulfillment
of the requirements for the degree of
Doctor of Philosophy in Electrical Engineering
Department of Electrical Engineering
College of Engineering
University of South Florida

Major Professor: Stephen E. Saddow, Ph.D.
Edwin Weeber, Ph.D.
Andrew M. Hoff, Ph.D.
Mark J. Jaroszeski, Ph.D.
Ashok Kumar, Ph.D.
Karl Muffly, Ph.D.
Jing Wang, Ph.D.

Date of Approval:
May 28, 2009

Keywords: cubic silicon carbide, nanocrystalline diamond, implantable neuronal prosthetics, mammalian cell biocompatability, neural action potential

Dedication

I would like to dedicate this work to my whole committee. Each and every one of them has been involved closely with this research, and will continue to do so as we enter the next stage. Your knowledge, assistance, mentorship and friendship have been invaluable to me. Secondly, I would like to thank my current associates and my friends: Chris Locke, Alexandra Oliveros, Norelli Schettini, Gene Short, and Eduardo Murphy-Perez. Your help, patience and all the good times after work have kept me sane and moving forward. I also thank my many associates who have moved on or have returned to their countries: Dr. Jeremy "the raging' Cajun" Walker, Dr. Andrea Severino, Patrizia Pappalardo, Dr. Massimo Camarda, Dr. Ulrich Starke, and Sebastian Schoell. Your hospitality and friendships are much appreciated. I would like to give a special thank you to the one who means a lot to me: Dr. Camilla Coletti. She started our group onto the path of biotechnology, and was a very good friend of mine. Thank for being there when I needed you. To my parents and family, thanks for helping me get through the years of school and putting up with me not being around. Thanks also to my many fiends: Steve Bradshaw, Frank Pytel, Chris Coules, Steve Short, and the whole Hollis Clan. Now you have read this, perhaps you understand what I was doing all the time.

Finally, thank you to the original 'Dr. Evil', Stephen Saddow. Thanks for giving a misfit a chance to change the world, and for pushing me harder each year (can it get a little better now?). I will be forever in debt for your mentorship and support. We will carry on and seize the day until the bitter end.

Acknowledgements

I would like to thank the Max Planck Institut in Stuttgart, DE, and Dr. U. Starke for the opportunity to work alongside them on two occasions. Specifically, I would like to thank M. Hetzel and Dr. C. Virojanadara, and C. Riedl for their expertise with LEED, STM, and XPS and our work in (§ 2.3). Next, I would like to thank IMM-CNR in Catania, IT, and Dr. F. La Via for hosting me twice during our SiC collaboration. I would like to thank Dott. G. D'Arrigo for teaching me how to generate masks, C. Bongiorno for his excellent TEM work [(§ 2.2), (§ 5.2)], and M. Italia for his SEM imaging (§ 2.2). I would like to thank the Walter Schottky Institut in München, DE, and Dr. M. S. Brandt, for our collaborative work into surface modification of SiC. I would like to thank Dr I. D. Sharp and M. Hoeb for their work on surface functionalization and ATR-FTIR measurements in (§ 4.2). A special thanks goes to Dr. P. Spagnol and Dr. J. Bumgarner of SRI International in Largo FL for their collaboration work in (§ 2.2.3) and their financial support. At USF, I would like to thank the NNRC facilities and staff for their assistance over the years of SiC film growth and characterization and A. Oliveros and Dr. Saddow for fabricating the first SiC NAD devices (§4.4). At the Johnnie B. Byrd Sr. Alzheimer's Center & Research Institute, I would like to thank Dr. J. Rogers and Dr. M. Peters for their assistance with the cell lines in (§3) and the NAD device activation in (§4.4). I also thank Dr. M. L. Selenica at the Byrd Institute for her primary mouse cortical cells and our work in (§4.3). I thank H. Gomez and Dr. J. Sathyaharish for their NCD deposition on 3C-SiC substrates (§2.4). I wish to acknowledge the Office of Naval Research, Dr. C. Wood, for many years of financial support. Finally, I thank the USF FMMD fellowship and Dr. T. Vickerson for her kindness and support.

Table of Contents

List of Tables

List of Figures

The Neuron-Silicon Carbide Interface: Biocompatibility Study and BMI Device Development

Christopher L. Frewin

ABSTRACT

Damage to the central nervous system (CNS) leads to the generation of an immune response which culminates with the encapsulation of the damaged area. The encapsulation, known as a glial scar, essentially breaks neural signal pathways and blocks signal transmissions to and from the CNS. The effect is the loss of motor and sensory control for the damaged individual. One method that has been used successfully to treat this problem is the use of a brain-machine interface (BMI) which can intercept signals from the brain and use these signals to control a machine. Although there are many types of BMI devices, implantable devices show the greatest promise with the ability to target specific areas of the CNS, with reduced noise levels and faster signal interception, and the fact that they can also be used to send signals to neurons. The largest problem that has plagued this type of BMI device is that the materials that have been used for their construction are not chemically resilient, elicit a negative biological response, or have difficulty functioning for extended periods of time in the harsh body environment. Many of these implantable devices experience catastrophic failure within weeks to months because of these negative factors. New materials must be examined to advance the future utilization of BMI devices to assist people with CNS damage or disease.

We have proposed that two semiconductor materials, cubic silicon carbide (3C-SiC) and nanocrystalline diamond (NCD), which should provide solutions to the material biocompatibility problems experienced by implantable BMI devices. We have shown in this study that these two materials show chemical resilience to neuronal cellular processes, and we show evidence which indicates that these materials possess good biocompatibility with neural cell lines that, in the worst case, is comparable to cell-treated polystyrene and, in most cases, even surpasses polystyrene. We have utilized 3C-SiC within an electrode device and activated the action potential of differentiated PC12 cells. This work details our initial efforts to modify the surfaces of these materials in order to improve cellular interaction and biocompatibility, and we examine our current and future work on improving our implantable BMI devices.

Chapter 1: Introduction

1.1 Research Objective and Motivation

For humans and mammals, the central nervous system (CNS) processes incoming data from the senses, controls muscles and organs, and is a storehouse for acquired knowledge. Unfortunately, damage to this system from disease or trauma does not readily repair itself because scar tissue is formed in the damaged area that blocks the normal flow of CNS electrical signals. The effect of this scarring is to block signaling between the CNS and the organs/muscles it serves, leaving the individual with decreased or no functionality in the blocked systems. Extreme damage can cause paralysis of the motor system, blindness or deafness, while certain diseases, such as Alzheimer's and Parkinson's, cause malfunctions in the signaling capabilities of the brain. Brain machine interface (BMI) devices, also known as the brain computer interface (BCI) devices, is a burgeoning technology developed by engineers, neurologists, and computer scientists that has the potential to offer hope and possible cures for many problems associated with the central nervous system (CNS) [1-3]. BMI devices allow communication between the signals generated by neurons in the brain and external devices, and implantable BMI devices allow for the potential of two way communication [1-3]. A BMI with two way communication allows the device to act as a bridge that potentially restores neural pathways damaged by a glial scar, or intercepted signals are utilized to control external

devices which in turn could send information back to the brain. This technology has the potential to allow motor restoration to paralyzed individuals or those with diseases such as Parkinson's. In particular, with so many affected by injuries from war, amputee victims will be able to use their mind to control a motorized prosthetic and receive sensory information back from this device.

Interaction with biological processes at the cellular level is an important component of implantable BMI devices. Micro-electromechanical systems (MEMS) are one method that opens an avenue for this interaction to be realized. Electrical interaction with muscle and nerve cells is possible using the MEMS systems, and MEMS micro-fluidic devices potentially can allow targeted delivery of drugs or cellular enzymes to the brain [4, 5]. Although MEMS technology offers many new possibilities to interact with the cellular environment, current-generation neural prosthetic devices require indefinite long term chronic implantation to perform their designed functions. Extended interaction with the body requires that the materials used have a high degree of biocompatibility which must be considered for the design of the devices. Biocompatibility generally refers to the ability of a device and its component materials to perform their desired functions, maintaining beneficial cellular and tissue responses, and not eliciting undesirable local or systemic effects in the body [6]. This biocompatibility requirement therefore places significant restrictions on the design of implantable MEMS devices, and each part of the body possesses slightly different factors of biocompatibility.

Silicon, Si, has been long used in the construction of MEMS devices as the material possesses the hardness of steel, is relatively inexpensive to produce, and can be

easily fashioned into complex mechanical devices using techniques developed by the semiconductor industry [3-5]. Si is a primary constituent of many MEMS devices because it is a semiconductor, a material which can be electrically insulating or conductive depending on both its properties as well as the stimulus that is applied to the material. Hence semiconductor materials can be used to electronically sense stimuli which allows for the realization of complex electrical devices. These devices allow for the precise control of electrical potential fields (voltages) and currents, and can be combined to make complex devices like sensors, microprocessors, and radio transmission devices. Complex electrical devices are the backbone for the functionality of many of the MEMS devices used for cellular interaction [3-5]. Unfortunately, the material properties of Si that allow for the construction of these complex devices provide a complex problem which complicates the biocompatibility of Si. Si is not chemically resilient, possessing a high reactivity to numerous acids and bases as well as allowing chemical diffusion into the crystalline lattice, and it has been shown to actively react with many biological enzymes and fluids [7-11]. Silica, SiO_2, is the native oxide of Si and is also the primary dielectric component of field effect devices, but it is easily contaminated with metallic ions, many of which are found commonly within the body [12]. SiO_2 also hydrolyses into silicic acid, $Si(OH)_4$, a compound that is found as a trace element throughout the body in blood plasma and connective extracellular tissues; however, the exact purpose this compound serves with respect to cellular metabolic process is still being investigated [7-11]. Some studies show that silicic acid reacts with Al-containing compounds to produce substances that may contribute to Alzheimer's and Parkinson's disease [11]. Also,

minute silicate particulates have been known to be carcinogenic to many organs and cells and these materials usually cause initiation of the body's inflammatory response which activates phagocytes and eventually escalates into material encapsulation [9, 10]. Once a Si-based sensor, for example, is encapsulated it clearly ceases to be a sensor and becomes a useless foreign object, and further body reactions can lead to cell mortality [9-12]. Because of this bioreactivity, Si is not a material that can directly interact with the biological environment and must rely on other materials for this interaction as well for its own protection.

Mechanical interaction can be achieved through physical coatings added over Si, such as polymers or ceramics. Electrical interaction with the cells and the body's constituents is achieved through extensions of conductive electrodes [3, 13, 14]. Although many of the physical coatings, especially polymers, allow the MEMS devices increase their biocompatibility and interact more specifically with the body environment, the electrodes are very susceptible to changes in impedance caused by biofouling or encapsulation, and many materials used for these electrodes, like platinum, iridium, iridium oxide, and conductive polymers have Faradic reactions at the current levels required for cellular interaction and, therefore, suffer physical damage and degradation over time [14]. Field effect devices such as capacitors and field-effect transistors would be able to react with the environment through capacitive instead of Faradic reactions, but would require a biocompatible and bioresistive semiconductor material to achieve this interaction [14, 15].

One material that has been used in direct interactions with the body environment is silicon carbide, SiC. Silicon carbide is a physically strong material and is chemically inert making it ideal for interaction with the harsh body environment. Amorphous and polycrystalline forms of silicon carbide, a-SiC and poly-SiC, have been used as coatings for many implantable biomedical devices, and clinical studies for bone prosthetics and heart stents have confirmed the biocompatibility of these forms of SiC [16-19]. Single crystal SiC has an additional advantage in that it is a semiconducting material like Si, which enables the creation of complex electrical devices and utilizes many of the device processing techniques available to Si. Two polytypes of Si, 4H-SiC and 6H-SiC, have been available commercially as substrate wafers and have shown good biocompatibility, non-toxicity, and low biofouling [20]. Cubic silicon carbide 3C-SiC, the only polytype of silicon carbide with a zinc blended atomic structure, can be heteroepitaxially grown on other zinc blende crystals like silicon and diamond, or it can be heteroepitaxially grown on the hexagonal forms of SiC, namely 4H-SiC and 6H-SiC [21-24]. 3C-SiC possesses superior strength, excellent electrical properties, and chemical resilience when compared with other semiconductor materials, and would make an excellent platform for the creation of an implantable MEMS neural interface for BMI devices.

This chapter is organized to serve as an introduction to biological systems and physical concepts involved with a man-made neural interface. First, the central nervous system (CNS), how it is organized and functions, and its major cellular constituents are described and detailed (§ 1.2). Next, the concepts behind neural bioelectricity and how electrical based device could interact with them are explained (§ 1.3). BMI device

operation, both non-invasive and invasive operation forms, is explained in (§ 1.4). Finally, the semiconductor materials 3C-SiC (§ 1.5) and nanocrystalline diamond (NCD) (§ 1.6) are explored with respect to their unique material properties and biocompatibility with mammalian cells as possible construction media for BMI devices.

1.2 The Basic Central Nervous System

The nervous system serves as the control center and signal transport for vertebrate organisms, and monitors all sensory input, motor functions, and information processing. Anatomically, this system is composed of two distinct subdivisions, the CNS and the peripheral nervous system (PNS). The CNS is composed of the brain, the brain stem, and the spinal cord, while the PNS contains all the connection pathways from the CNS to sensory and motor actuators.

The CNS is a complex organ system whose operation is just beginning to be understood. The human brain, shown in Figure 1.1, composes the majority of the CNS and has four primary systems each with different functions. The first system is the cerebrum which is composed of two cerebral hemispheres connected through the corpus callosum and represents 85% of the brain's weight. This part of the brain controls voluntary actions, processes sensory information, and is involved in thinking, learning, and decisions. The second part of the brain, composing about 10% of the weight, is the cerebellum which processes sensory information, and is linked closely with the motor system. This system also maintains balance and learning associated directly with motor functions. The third part of the brain, the limbic system, links the higher brain functions

from the cerebrum with the automatic systems of the brain stem. The limbic system is composed of four parts: the amygdala processes strong emotions; the hippocampus processes short term memory into long term memory; the thalamus controls sensory information; and the hypothalamus regulates body secretions and temperature. Finally, the brain stem is the fourth system of the brain which controls all automatic functions, like breathing and heart rate, and provides a signal pathway to the spinal cord. The second system of the CNS, the spinal cord, provides a pathway for signal transmission to sensory and maintenance organs as well as controls reflexive actions.

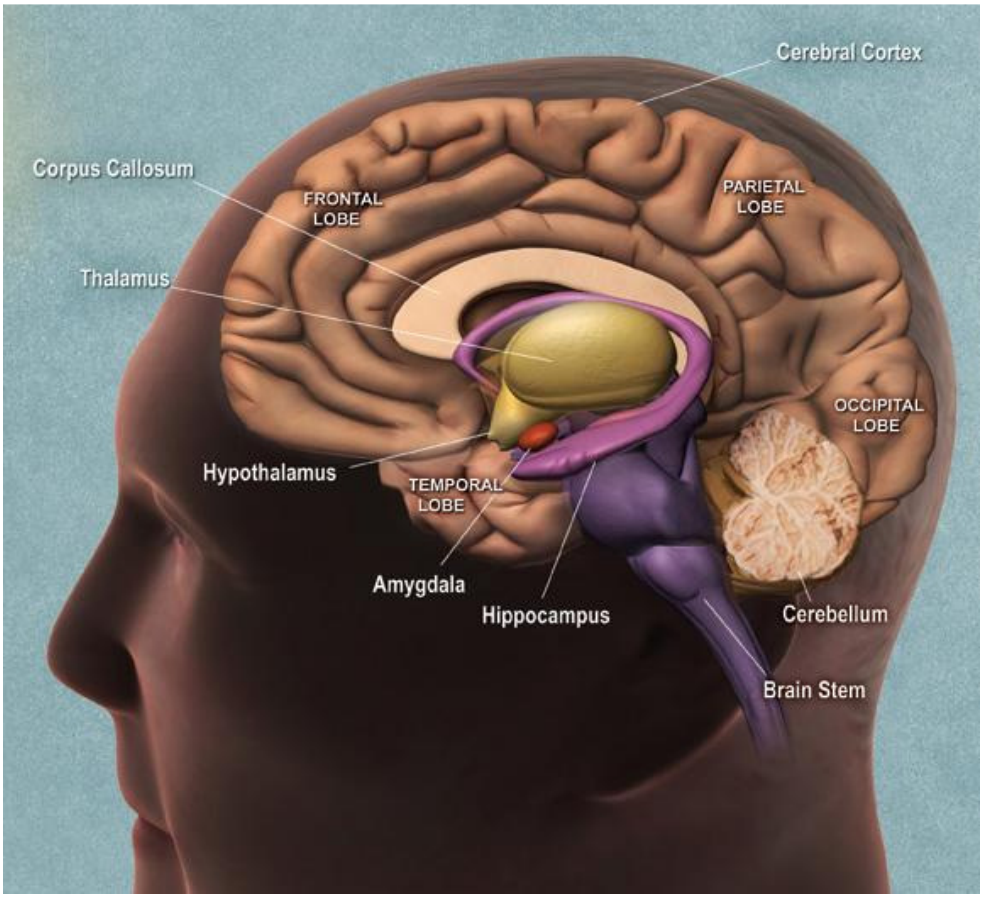

Figure 1.1: A cutaway cartoon representation of one hemisphere of the human brain. The major components of the brain are indicated. [25].

Like other complex organs in the body, the CNS is composed of a multitude of specialized cells that allow it to complete its tasks efficiently. This cellular diversity complicates interaction with this organ from an implantable device as each cell can potentially react differently. (§ 1.2.1) and (§ 1.2.2) will explore the basic cells involved with an implantable device while (§ 1.2.3) details the cellular response to damage and foreign materials.

1.2.1 The Neuron Cell

The main workhorse of the CNS is the neuron which is displayed in Figure 1.2. The neuron cell produces the signals that control body functions and is the target cell for an implantable BMI device. This cell is composed of three main parts. The soma, or cell body, contains the nucleus and other cell organelles common to all cells and regulates specialized enzymes and neurotransmitters. The short, fibrous dendrites extend from the soma and contain specialized receptors that intercept incoming chemical or electrochemical signals from other cells. Although the dendrites mainly are utilized for the reception of signals, some actually have two-way signaling functionality. The longer, fibrous axon is mainly utilized to transmit signals to other neurons or cells. Specialized protein-gated channels along the axon allow the transmission of electrical signals, and the long microtubule-filled structure provides a pathway for the transport of organelles and vesicles to the synapse.

Neurons are not directly connected to other cells in the neural network, but the axon termination is located near a receiving dendrite or cell and the space between them

is called the synapse. Two types of synapses are found within the CNS system, an electrical synapse and a chemical synapse. A neuron can generate or transfer electrochemical signals called an action potential which is the product of electrical potentials created by the movement of ions through membrane channels, and these potentials in turn generate diffusion current that is propagated through the axon. As the AP reaches the terminal button in the axon containing an electrical synapse, cell pores open and ions travel freely between a very small synaptic gap between the cells. The gap is very tight and isolated from the extracellular medium as to prevent loss of the signal due to leakage, and some of the cell pores are activated electrically, allowing for some rectification of the signal.

Neurotransmitters are special chemicals generated within the cell that are designed to either suppress or excite the electrical excitation in a neighboring cell. Neurotransmitters are packaged in vesicles and transported down the axon. When an action potential excites a terminal button containing a chemical synapse, calcium permeable channels open allowing Ca^{2+} to enter the membrane. The high level of calcium activates proteins in the vesicles walls and they move toward the synapse. As shown in the inset in Figure 1.2, the vesicles dock with the synaptic membrane and release the neurotransmitter into the gap. Receptors in the neighboring cell bind some of the neurotransmitters, which cause a change in ion permeable channels. The open ionic gates allow ions to move into or out of the cell and modulate its transmembrane potential, and can depolarize the membrane if the transmitters are excitatory or hyperpolarize the membrane if the transmitters are inhibitory.

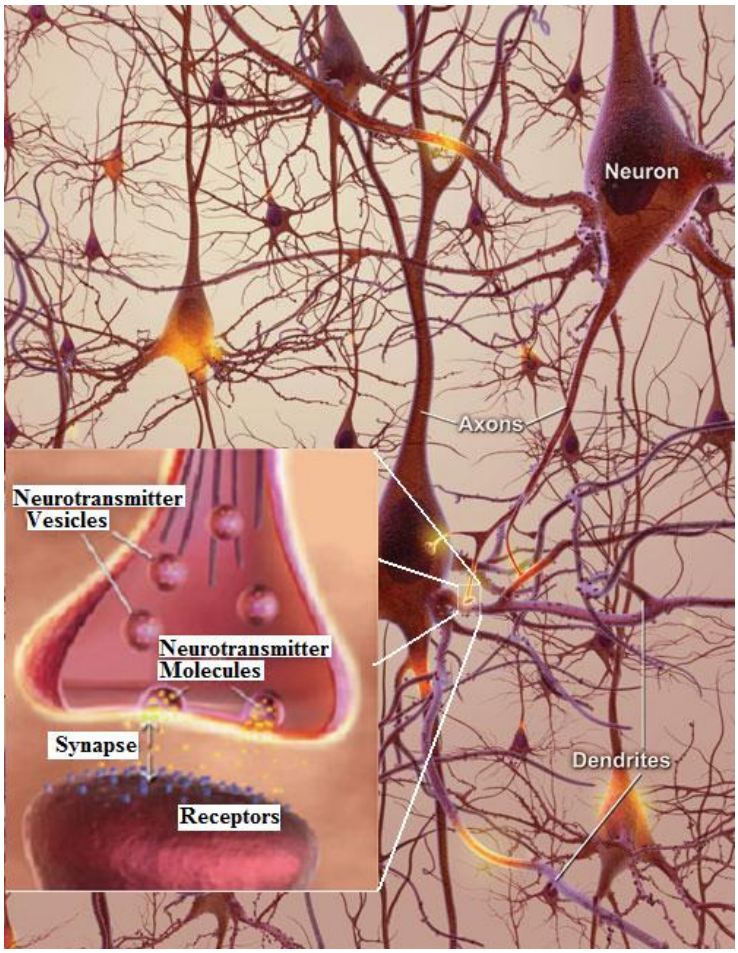

Figure 1.2: A representation of a neuron displaying the soma, dendrites, and axon. The inset displays one synapse and details how neurotransmitter molecules are transmitted from one neuron to another [25].

1.2.2 The Glia Cell

The glia are a group of cells that outnumber the neurons in the CNS by as much as 50 to 1, and they provide a regulatory role by maintaining nutrition, structural support, aid signal transmission, and form the brain-blood barrier. The first cell that a BMI implant would encounter is the astrocyte, also known as astroglia. The astrocyte, a cell that is now beginning to be considered very important in the CNS system, are the most abundant and variable glial cell in the CNS. First, they provide structural support for the

other cells in the CNS [26]. Secondly, they maintain the synapse and extracellular space by clearing expended neurotransmitters and excess ions, and modulate signals through the release of neurotransmitters [27]. These cells also promote axonal guidance and myelination from oligodendrocyte cells [28, 29]. Astrocytes help maintain the blood-brain barrier, the barrier formed by endothelial cells that prevents blood from contacting CNS tissue directly [26]. Finally, astrocytes play an important role in CNS repair, which will be covered in more detail in (§ 1.2.3), a fact that places this cell in the interface path of an implantable device.

Another very important glial cell is the oligodendrocyte which produces the myelin sheath around the axon. The myelin prevents the AP from being dissipated into the space surrounding the axon, allows the current to 'hop' down the system instead of traveling in a wave, and provides a pathway for regeneration of the axon if it is severed. The myelin creates a depolarization at a node of Ranvier which is sufficient to elevate the neighboring node to threshold potential and thus increasing the speed of signal propagation.

Microglia are a form of macrophage, or cell eater, which responds to injury in the CNS. These cells make up 20% of the glia population and are located throughout the CNS at all times unlike regular blood derived microphages. They are vigilant sentinels which are inactive for the most part, but monitor the CNS for damaged neurons, infectious agents, or foreign body invasions [30, 31]. Their exact role in the inflammatory process will be covered in more detail in (§ 1.2.3). Another important glial

cell that would encounter an implantable device is the ependyma cell which generates and transports cerebrospinal fluid throughout the CNS.

Another group of cells that is encountered by implantable devices comes from the meninges which is a protective membrane sheath consisting of the dura matter, the arachnoid matter, and the pia matter. The Dura matter is a thick, fibrous, leather-tough layer which is infused with the major veins and arteries for the brain. This layer is the layer that must be pierced before a device can interact with the cells of the brain. The arachnoid matter possesses a spider-web appearance and acts as a shock absorber for the brain. The pia matter is firmly anchored to the brain and is intertwined with capillaries that deliver the blood to the brain matter. An implantable device must prevent damage to this layer to preserve the blood-brain barrier.

1.2.3 Glial Scarring

The reaction of the CNS to injury is a complex and little understood process. Injury, almost independent of source, causes a similar reaction that permanently leaves the recipient with decreased function. It has been shown by Santiago Ramón y Cajal in the late 19th century that neurons *in vitro* have the ability to regenerate damaged axons, but neurons *in vivo* do not regenerate and therefore do not reconnect signal pathways [32]. Instead, a process called reactive gliosis, more commonly referred to as glial scarring, is the reaction of the CNS to injury from trauma, disease, or long term inflammation [30, 31]. Although the exact purpose of this reaction is unknown, glial scarring essentially isolates and encapsulates the damaged portion of the brain and

restores the blood-brain barrier. Unfortunately the glial scarring process also has a downside in that it prevents the regeneration of axons across the breach [31]. The final scar is created by the presence and injury responses of the glial cells, namely astrocytes, microglia, and oligodendrocytes, and if the meninges was compromised during the process that initiated the glial scarring response, these cells are also react to the injury [31].

The process begins with the activation of the sentinel microglia cells, which begin to divide and migrate to the injury site, and if the blood-barrier was broken, white blood cell macrophages will also migrate to the site to assist the microglia cells [31]. The activated microglia and macrophages work to clean the site of myelin, which is inhibitory to axon growth, and necrotic tissue, but they also can produce cytotoxic responses for the purpose of destroying pathogenic organisms if they are present. The cytotoxic responses can, over time, poison the damaged area and inhibit regeneration of the axon [31]. If the meninges were damaged, meningeal cells rush to the site of the injury to reestablish a new continuous covering for the CNS, however these cells do not provide a substrate that is conducive to growth of new axons [31]. The oligodendrocytes and the myelin that they produce are present at the site, especially in the case of trauma, and the oligodendrocytes usually collapse regenerating growth of axon cones that contact with them [31]. Oligodendrocytes do not seem to promote axon growth or the generation of new myelin sheaths [31].

The majority of the glial scar is caused by the actions of the astrocytes. The injury changes the cell into a reactive astrocyte which has an increase in filament and

general cell size. The cell becomes phagocytic and ingests necrotic cellular material and it also releases inhibitive molecules that are non permissive to axon growth [31]. Although these cells seem to have the ability to initiate neurogenesis in adult stem cells, the activated cells instead undergo cell division and fill the extracellular space around the damage [26]. The final scar is tissue composed of tightly packed hyperfilamentous astrocytes, many of which have processes that oppose one another, and have tight junctions that forms a barrier to fluid. The tight junctions restore the blood-brain barrier, but the tight mesh of cells prevents all further attempts from surviving neurons to form axons.

1.3 Theory of Bioelectricity

Many cells in the body use electrical signals for communication or activation of functionality. Neurons are the major transport pathway of these signals, and their main function is to generate and relay signals to actuators of the body. Actuator cells include muscle cells and many sensory associated cells. The generation of signals is a complex action derived by the difference of inorganic ionic concentrations outside and inside the cell, and the electric potential created by these ionic concentrations. (§ 1.3.1) begins with detailing the cellular membrane theory, followed by the parallel conductance model in (§ 1.3.2) and the quantification of the action potential in (§ 1.3.3). External stimulation of muscles and nerves was first observed and recorded by L. Galvani in 1783. (§ 1.3.4) and (§ 1.3.5) detail how an implantable device can interact electrically with a neuron at a cellular level.

1.3.1 Cellular Membrane Theory

The cell membrane is composed of a lipid bilayer which organizes itself so the hydrophilic polar head faces the water environment and the non-polar hydrophilic tails face away from the water. Within this lipid membrane are various highly selective pumps and channels, some of which serve as transport for various ionic components. If these channels are opened, the ions within the extracellular and intracellular matrix flow along both the ionic gradient and the changes in the electric field generated by the ions on either side of the insulating lipid bilayer. The Nernst-Planck equation describes the current density vector in an electrochemical cell:

$$\overline{J_p} = -D_p F Z_p \left(\nabla C_p + \frac{Z_p C_p F \nabla \Phi}{RT} \right) \tag{1.1}$$

In this equation the electric current density, J_p, measured in coulombs per second per cm^2, is a function of the diffusion coefficient D_p, the concentration C_p, the sign of the force, Z_p, Faradays constant, F, the gas constant, R, and the temperature, T. The Nernst-Planck equation can be used to derive the Nernst equilibrium which describes the electrical potential difference across a membrane, Φ_i - Φ_e, or the interior potential minus the external potential. This difference simply equates to the membrane voltage, V_m, and is obtained through an integration of terms using the capacitance-voltage relationship as described by Ohms law. The resulting equation is as follows:

$$V_m = \Phi_i - \Phi_e = \frac{-RT}{Z_p F} \ln\left(\frac{[C_p]_i}{[C_p]_e}\right) \tag{1.2}$$

This model successfully explains the action of a single ion concentration brought into equilibrium across the membrane, but does not take into consideration that all the other ionic species in the electrochemical solution have different concentrations and equilibrium levels. There are also many ionic channels with different conditions along a single membrane. A new model would have to be developed to describe the membrane voltage.

1.3.2 Parallel Conductance Model

The parallel conductance model was developed by David Goldman, Alan Hodgkin, and Bernard Katz to describe the dynamic mechanisms that are interacting across a cell membrane. The formulation of their model is a direct solution of the Nernst equation (1.2). The overall total potential across the membrane, E_m, is a product of three main channels, potassium (K), sodium (N), and chlorine (Cl). The membrane capacitance is placed in parallel with these three channel circuits to complete the model and the current through the membrane is then given by the Goldman-Hodgkin-Katz (GHK) equation:

$$V_m = \frac{RT}{F} \ln\left[\frac{P_K[K]_e + P_{Na}[Na]_e + P_{Cl}[Cl]_i}{P_K[K]_i + P_{Na}[Na]_i + P_{Cl}[Cl]_e}\right] \text{ where } P_q = \frac{D_q \beta_q}{d} \tag{1.3}$$

$$I_q = g_q (V_m - E_x)_q \tag{1.4}$$

$$I_c = C\frac{\partial V_m}{\partial t} \tag{1.5}$$

$$I_m = I_C + I_K + I_{Na} + I_{Cl} \tag{1.6}$$

For each of the equations, q is the index for the ion type, β is the force sign constant, d is the thickness of the membrane, and D is Fick's coefficient. The parallel conductance model gave a mechanism for the combination of various ionic channels to explain the dynamic voltage across the membrane; however the conductance's for the model proved to perform in a nonlinear manner and also to change drastically over time. It was noticed that if a membrane was sufficiently excited, a significant change would occur in the membrane channels that would elicit a large voltage response. At this voltage, known as the threshold voltage, V_t, most of the ionic channels would activate and the combination of their actions would create a large potential known as the action potential, and below this value, the membrane channels would display no statistical change.

1.3.3 Hodgkin's and Huxley's Equations

In 1952, Alan Hodgkin, Andrew Huxley, K. C. Cole, and the squid Loligo, investigated the nature of the action potential through the non-linear conductance of K^+ and Na^+ [33-36]. Their work, which was rewarded with a Nobel Prize, used a combination of a mechanism known as the space clamp to hold the voltage potential of the squid axon membrane at a experimentally determined level and modification of the ions in the media concentration [33-36]. The combination of these methods enabled the elimination of a particular channel's influence from the Goldman-Hodgkin-Katz equation

so that each individual type of channel conductance could be evaluated separately [33-36]. This experimental approach allowed the quantification, and later mathematical modeling as a function of time and of the membrane voltage, of the action potential with its relationship to the changing conductance of the K^+ and Na^+ channels and the effect of a leakage current [33-36]. The action potential was determined to be caused by a large change in the conductance of sodium followed by a slower change in potassium conductance and a slow reduction in sodium conductance caused by channel inactivation [33-36]. The experimentally obtained conductance was modeled statistically through curve fitting and correlated mathematically to the probability of the channel to be open or inactivated [33-36]. The probabilities were labeled (n) for potassium channel activation, and (m, h) for sodium activation and inactivation, respectively [33-36]. By using these probabilities, the total membrane voltage could be evaluated numerically through the use of the following equations [33-36]:

$$\Delta v_m = \frac{\Delta t}{C_m}\left[I_d - \bar{g}_K n_i^4 \left(V_m^i - E_K\right) - \bar{g}_{Na} m_i^3 h_i \left(V_m^i - E_{Na}\right) - g_l \left(V_m^i - E_i\right)\right] \tag{1.7}$$

$$I_d = I_K + I_{Na} + I_l + C\frac{\delta V_m}{\partial t} \tag{1.8}$$

$$g_K(t) = \frac{I_K(t)}{\left(V_m - E_K\right)} \tag{1.9}$$

$$g_{Na}(t) = \frac{I_{Na}(t)}{\left(V_m - E_{Na}\right)} \tag{1.10}$$

$$g_K(t, v_m) = \bar{g}_K n^4(t, v_m) \tag{1.11}$$

$$g_{Na}(t, v_m) = \bar{g}_{Na} m^3(t, v_m) h(t, v_m) \tag{1.12}$$

$$I_l = g_l(V_m - E_l) \tag{1.13}$$

These equations relate the membrane voltage, V_m, to the exciting current, I_d, the currents for the K^+, Na^+, and L (leakage or the Cl^- channel), and the membrane capacitance, C_m [33-36]. The action potential of a membrane can be modeled using these equations and a computer simulation based on this model is displayed in Figure 1.3 for polarizing and hyperpolarizing exciting currents.

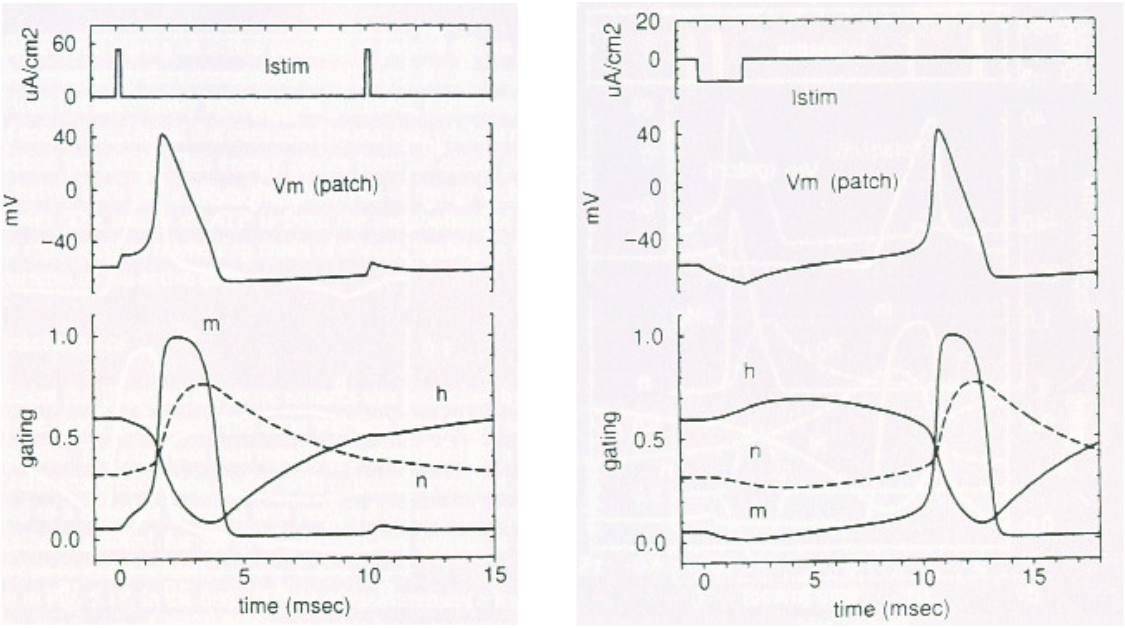

(a) (b)

Figure 1.3: Computer simulations of the action potential using the Hodgkin-Huxley equations for (a) a polarizing current and (b) a hyperpolarization current. (a) displays the polarizing stimulating current, I_{stim}, the membrane voltage, V_m, and the gating variables (m, n, h) as a function of time variations as well as displaying the concept of absolute refractory period with the addition of a second excitation current. (b) displays the temporal variations of the same factors as a response to a hyperpolarizing current [37].

The equation not only models the action potential as a function of the exciting current, but displays the concept of a refractory period. If an action potential is activated, a period of time is required for the ionic channels to reset to resting state before another action potential can be executed no matter the level of the stimulus, and this time period is known as the absolute refractory period. However, there is a time at which sufficient channels have returned to the resting state and the action potential can be excited again with an abnormally high stimulus. This time period is known as the relative refractory condition and both of the refractory periods can be determined from the Hodgkin-Huxley equations.

1.3.4 Microelectrode Device Interaction

The methods developed by Hodgkin, Huxley, and Cole to activate and measure the electrical activity of a neuron required a large instrument called the space clamp [33-36]. Due to technological limitations of the late 1940's, the wire electrodes required large membrane areas, like the one provided by the large nerves of the giant squid, and the signaling electronics were restricted to vacuum tube technology. In the late 1950's, new fabrication techniques were enabling the creation of glass microcapillary electrodes, later known as the patch clamp, that worked along similar principals to the space clamp to investigate the intracellular properties of small cells [38]. Although this method is excellent for understanding the neurophysiology of individual neuron cells, the method is limited to *in vitro* methodology and generally can only be utilized for a short time.

A parallel line of research developed around the same time utilized insulated metal electrodes to investigate populations of cells [39]. This type of electrode was further refined in 1970 by utilizing techniques for microfabrication developed by the burgeoning Si semiconductor manufacturers. K. Wise *et al.* developed a planar microelectrode using a Si substrate, glass, and gold [13]. An advantage of this electrode is it can interact and target specific cells instead of generalized populations and had a very low profile of approximately 15 μm [3, 4]. Although other, more biologically compatible materials are utilized for the modern planar microelectrode, it remains the most popular style of electrode device as it is easily, inexpensively produced to exacting and repeatable standards and can be utilized *in vivo* for extended times [3, 4].

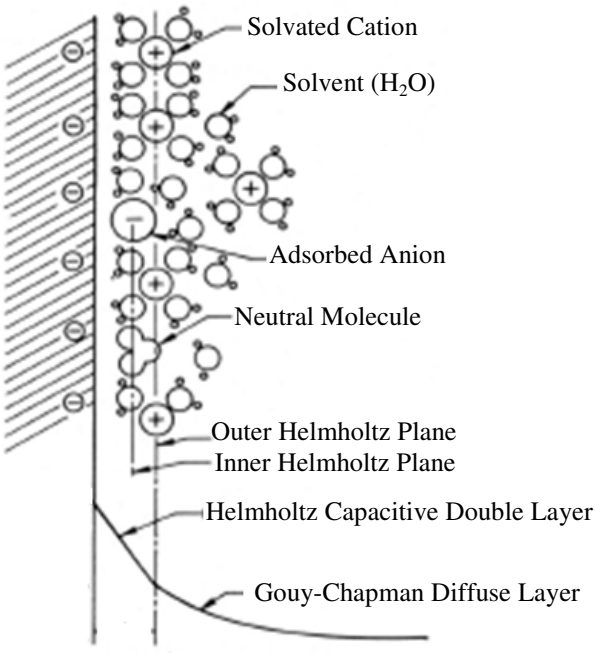

Figure 1.4: A depiction of the capacitive double layer formed at the surface of a metal in an electrolyte [13].

Generally, a metal inserted into an electrolyte will undergo oxidation, thereby extruding an electron and becoming a positively charged ion and is depicted in Figure 1.4 [13, 14]. The electrons are forced to the surface of the metal by the repulsive forces from the abundant electrons in the bulk, and the surface electrons in turn attract ionic species in the electrolytic solution. The ions gathered to the surface form the Helmholtz plane, a double layer consisting of the inner Helmholtz plane which is mainly solvated water molecules surrounding a cation, and outer Helmholtz plane which is composed of the solvated cations themselves. At surface equilibrium, a Gouy-Chapman diffuse layer is generated beyond the Helmholtz layer by thermal motion.

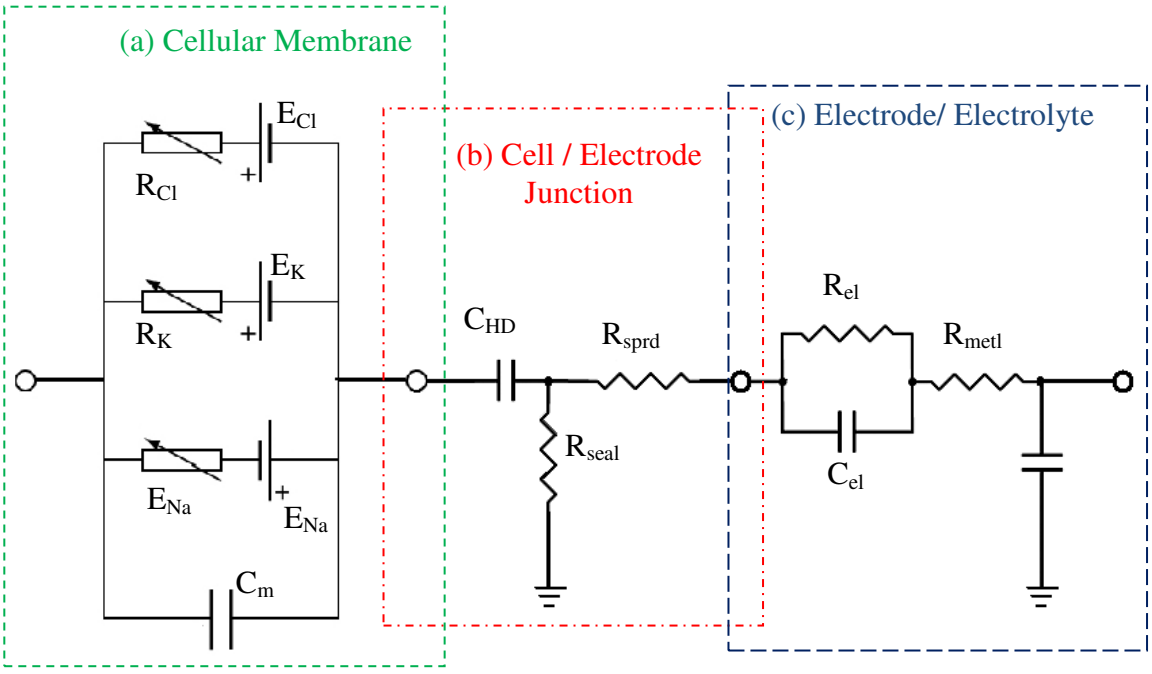

Figure 1.5: A circuit model of the electrode-cell interface. The cell membrane (a), coupling (b), and electrodes (c) are separated by dotted boxes [40, 41].

The electrode-electrolyte to cell interface can be described by modeling the double layer interaction with the GHK membrane model. The combined circuit is shown in Figure 1.5 [40 -42]. The metal-electrode junction is modeled as a resistor, R_{metl}, in parallel to a shunt capacitance, C_{sh}, which accounts for all parasitic capacitances from the tip of the electrode to the external electronics [40]. The double layer capacitance from the electrolyte / metal junction is modeled as a parallel capacitor and resistor in series with the metal, R_{el} and C_{el} [40]. The cell-electrode junction is modeled as a resistor, R_{sprd}, or the voltage drop due to the distance of the cell from the electrode [41]. R_{seal} is the voltage drop across the cleft between the cell membrane and the electrode, and C_{HD} is the capacitance effects of the double layer on the cellular membrane [41]. The cellular membrane can be electrically modeled as a capacitance generated across the lipid membrane in parallel with the major semipermeable channels. Each channel is modeled as a battery in series with a variable resistor which is linked to the equations developed by Hodgkin and Huxley (§ 1.3.3- 1.3.4).

Although this model explains both transmission and reception of signals by a planar microelectrode, there is a problem with these devices. Instead of working within the capacitive regime of the double layer, many of the materials used to date for electrode construction experience irreversible oxidation or reduction reactions at high charge-injection levels required for neuron activation, known commonly as Faradic electrode reactions [14]. Platinum, iridium, and conductive polymers experience Faradic reactions at the charge injection levels required for neuron activation, and the resulting chemical reactions degrade the electrodes over time, produce chemical byproducts which can lead

to a foreign body response from the immune system, or produce hydrogen or oxygen that attack cells [14]. Another problem with electrode based neural implant devices is they require relatively large geometrical areas to generate the appropriate level of charge injection. One method to alleviate this difficulty is to use at least two electrodes to complete the circuit loop when signaling a neuron to allow a balance in the ionic current flow required for neuron membrane depolarization [3, 14]. Implantable neural devices must be designed as small as possible to decrease evasiveness, and the space requirements for electrode wiring feed-through to onboard electronics create major limitations in the amount of active interaction locations due to this small size. Finally, electrodes are highly sensitive to changes in impedance levels, which elevate the resistances, R_{sprd} and R_{seal}. One of the causes of this factor originates from the chronic foreign body response, glial scarring, covered in (§ 1.2.3), which eventually produces device encapsulation or the electrodes become biofouled with adsorbed biological material [14].

1.3.5 Field Effect Device Interaction

An alternative to electrode interaction with neurons was developed by P. Fromherz *et al.* from the Max-Planck-Institut which has shown that Si metal-oxide-semiconductor capacitors (MOScap) can stimulate neuron membrane depolarization and Si metal-oxide-semiconductor field effect transistors (MOSFET) can receive action potential signals from neurons [15, 42-45]. The major advantage of MOS or metal-insulator-semiconductor (MIS) devices is they interact with the cell through capacitive

field effects without using electroporation or electrochemistry. Also, these devices are not as susceptible to changes in impedance as their electrode counterparts [15, 42-45]. Another advantage for FET devices is they can be interlinked into arrays by combining common connections, thereby reducing the amount of feed-through wiring required and allowing more active interaction areas on the neural interface [45, 46]. FET capacitor stimulation, unlike the electrode device, requires only one monophasic pulse to maintain charge balance, as charge dissipates gradually through RC parasitic losses [15, 43-44].

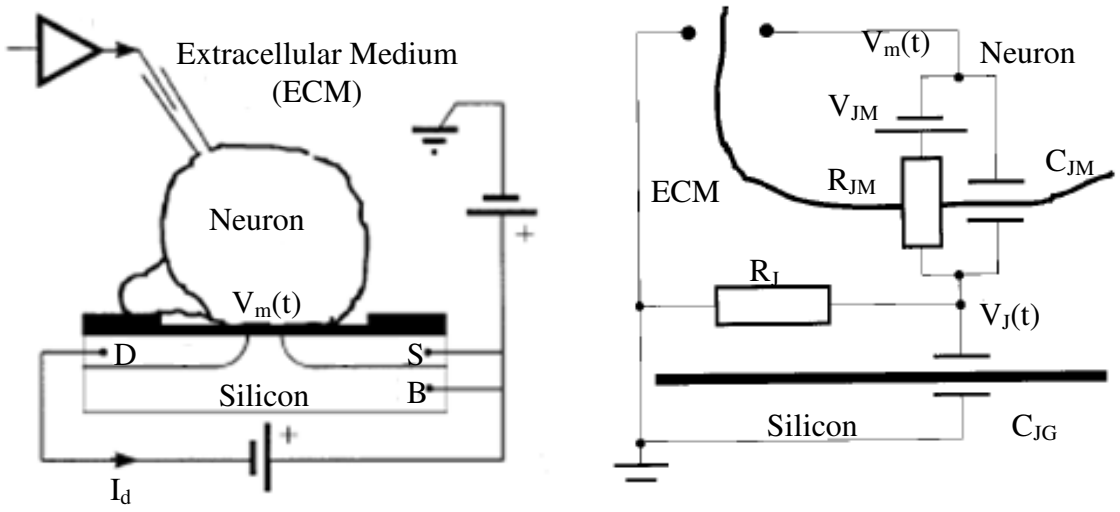

Figure 1.6: A cartoon representation of a neural cell on a MOSFET device where the cell membrane forms the gate metal. (a) shows a representation of the neuron acting as a gate for the MOSFET biased in saturation. (b) shows a circuit representation of the neuron on a transistor based of the membrane effects modeled by Hodgkin and Huxley (§ 1.3.3-1.3.4) [42].

To receive signals from the cell, Fromherz *et al.* utilized a MOSFET with no gate metal [42]. Figure 1.6(a) shows the concept that a neural cell essentially forms the gate metal through the coupling between the gate oxide and the cell membrane which they

called the transductive extracellular potential but is also known as the sealing resistance in (§ 1.3.4) [42]. The MOSFET driven into saturation, or active mode, with $V_{sd} > |V_{gs} - V_{th}|$, $V_s = V_b = VDD$, and $VDD >> V_{sd}$, provides a constant current flow through the device [42]. In saturation, the MOSFET drain current is directly controlled by the gate voltage. Activation of the action potential within a neuron will generate an influx of ions into the space between the membrane and the gate oxide, which leads to changes in ionic and displacement currents. This current modulates the transductive extracellular potential above the oxide, which in turn modulates the drain current within the MOSFET device [42]. Figure 1.6(b) displays a representation of the electrical circuit formed by the neuron and the MOSFET with discrete elements indicated [42]. The membrane voltage, $V_M(t)$, as a function of time is a product of the membrane channel with capacitance, C_{JM}, in parallel with the series combination of the variable channel resistance, R_{JM}, and channel potential, V_{JR}, all factors derived from the Hodgkin and Huxley equations. The membrane voltage is coupled to the specific capacitance of the gate oxide, C_{JG}, and the sheet resistance of the extracellular medium, R_J. The transductive extracellular voltage, $V_J(t)$, is the time dependent response to changes in the membrane voltage as influenced by sealing resistance R_J.

The stimulation of an action potential in a neuron can also be achieved through a field effect device, the metal-oxide-semiconductor capacitor, MOScap, or metal-insulator-semiconductor capacitor, MIScap [43, 44]. Fromherz *et al.* used the neuron membrane as the device metal, which formed the junction over an oxide on a semiconductor as with his transistor experiments [43, 44]. The MOScap is stimulated

with a voltage, V_{ST}, which gives rise to ionic and displacement currents in the junction. The currents would modulate the transductive extracellular voltage, and if this voltage was greater than the threshold voltage of the neuron, V_t, it would depolarize the membrane and generate an action potential [43, 44]. The advantage of using this stimulation over the electrode stimulation is that a single monophasic square pulse would lead to charge balance due to the charge dissipation of the capacitor [43, 44].

1.4 Brain Machine Interface (BMI)

As discussed in (§ 1.2.3), injury to the CNS does not readily regenerate but is instead isolated and encapsulated with a glial scar. The inability of the brain to send and receive signals leads to loss of function of muscles and sensory organs. However, undamaged portions of the CNS continue to function as before, and one proposed method to provide therapy is through the use of the brain machine interface (BMI). The broad concept of a BMI is to interface with undamaged nerves and then intercept, interpret, and transmit these signals to a machine or even another neuron in the body [1, 2]. This section is dedicated to giving a brief explanation of the current technology involved in BMI devices. (§ 1.4.1) will cover the non-invasive BMI devices which are currently in use by many patients suffering from amyotrophic lateral sclerosis (ALS), and (§ 1.4.2) details the BMI devices which utilize implantable neural microelectrode devices and the difficulties associated with them.

1.4.1 Non-invasive Neural Prosthetics

The indirect neural signal recording technology consists of electroencephalography (EEG), electrocortiography, (ECoG), galvanic skin response, near infrared recordings, and functional MRI [47]. EEG is a popular method of obtaining the input signals for a BMI device and has been used for well over 20 years. EEG based BMI devices consist of electrodes placed on specific locations of the scalp of the patient or subdermally directly over the cerebral cortex [48, 49]. The uses of EEG in neurological medicine have generated many methods for extracting signals related to action potentials. The device samples the electrical currents produced by post-synaptic potentials of many neurons, and can be adjusted to detect slow cortical potentials, α, μ, and β rhythms, or responses to "oddball" stimulus, commonly known as the P100 potential [49, 50]. The cortical area of interest is sampled electrically through current or voltage reception by the electrode, the sample is filtered through the use of electrical filtering and common spatial patterns. Spatial pattern filtering is the use of physical separation of electrodes, a method which weighs each electrode as to its importance to the signal discrimination, and correlations between neighboring electrodes [50]. The signals are then averaged and the appropriate pattern is extracted from the signal, and if the EEG is used as a BMI interface, this pattern takes the form of a command [49]. The extracted information is then transferred to a computer or robotic interface which acts on the desired command.

The use of EEG has many obvious advantages to people who would require the BMI device. First, it is purely non-invasive and does not require surgery, with the

exception of subdermally implanted EEG electrodes [49]. The device can extract many different types of potentials, and the positioning of the electrodes for collection of the potentials is well established [50, 51]. However there are many drawbacks to the use of EEG BCI devices. They are usually cumbersome, require multiple electrode attachments, require a long time for electrode to scalp application, and are uncomfortable for extended periods of time [49]. The potentials read by the system are combinations of a large number of neurons which need to generate a significant spike in activity that will not be eliminated due to electronic filtering, signal averaging or by the power drop across the highly resistive scalp [49]. Real-time execution of actions is further complicated by the extraction paradigms which limit execution of commands to only a few times per minute [49]. Finally, the patient must learn to generate an arbitrary signal and relate it to the appropriate command for the BMI device to function [51]. The generation of this arbitrary brain signal requires a great deal of conscious effort which requires a long training period, and both emotional and external environmental situations can interrupt the patients concentration which can lead in errors in signal interpretation by the EEG BMI device [51]. Even with all of these problems, the EEG indirect BMI has provided many solutions for people who suffer from paralysis, and its use has developed many invaluable methods for extracting information from neural activity.

Individuals with neuron degradation due to disease have a reduced signal output which lowers to a level that can no longer be ascertained with EEG devices. Galvanic skin response (GSR) is caused by a change in electrical conductivity of the skin by increased activity in sweat glands and can be measured by electrodes attached to the skin

[52]. The response was first documented by Carl Jung and is used as a biofeedback mechanism for evaluating emotional states, and has been used in the polygraph lie detection machine [52]. The GSR can only produce a binary response, and requires a long training period when used as a BMI device [52]. Unlike the EEG, it requires only two electrodes for operation, thus increasing the comfort level and decreasing application time. However, it suffers many of the same problems associated with the EEG. Drastic changes in visual input can create artificial spikes in the extracted signal, but auditory stimulation seems to stabilize the GSR response [52]. Another problem is that the "off/ no" signal is easier to maintain 80% of the time, while raising the GSR above threshold for an "on/ yes" signal is only 30% effective [52]. Operator fatigue, anticipation of response, and GSR stabilization also provide difficulties to achieving the desired response 100% of the time [52].

1.4.2 Invasive Implantable Prosthetics

Whereas the non-invasive BMI is based on the post synaptic electrical current averaged from relatively large areas of neurons, implantable devices can directly target single neurons to collect their action potential signals, or can collect local field potentials, which is a measure of dendritic synaptic activity for all neurons in the immediate vicinity [48]. Implantable BMI devices possess many advantages, and disadvantages, that must be accounted for if these devices are to become a viable therapeutic solution for restoration of the damaged CNS. Implantable BMI devices can collect signals in real-time and manipulate the signal without long term averaging required from non-invasive

techniques [49]. The ability to target specific areas of the brain, like motor neurons that control the movement of the arm, allows specific signals to be recorded so potentially the device needs no abstract signal generation or 'oddball' stimulus that is required by indirect BMI devices [49]. Experimental BMI devices have been shown to allow rats to control mobile robots, monkeys to control a robotic arm, and a human with ALS could control a computer by thought alone [53-55].

The greatest advantage of the implantable device is that they do not only allow reception of signals, but it can be used to induce action potentials in neurons allowing sensory input restoration for patients with somatic sensory loss [49]. This innovative technology has seen many successes such as the Cochlear implant, which assists people who have nerve damage associated with hearing, and the vagus nerve implant, which alleviates depression levels for people who are resistant to conventional antidepressant drug therapies [56, 57]. This factor also allows sensors integrated with robotic devices to relay information back to the brain to allow improved operation and provide sensory awareness of the prosthetic [2]. The two-way communication ability of an implantable BMI would allow for the construction of a device that could bridge signals over damaged neural areas thereby restoring natural functionality [2].

The implantable BMI device offers many solutions for the repair of the CNS system, but there are a few problems that must be surmounted. The selectivity of the devices is a major problem, and multiple signals captured by the neural implant creates difficulties in real-time filtering, sorting, and decoding of the signal into usable commands [49]. Complex, computationally intensive algorithms are required to sort

these signals, and the speed at which signals are generated requires digitization speeds greater than 20 kHz [49].

The CNS response to chronic implantation is one of the greatest difficulties facing the widespread incorporation of BMI devices and prevents its use in long term clinical studies [49]. The implantation of these devices, and subsequent activation of the healing process, lead to a "foreign body" response from the support cells in the CNS, the glia, whose actions escalate the levels of harsh chemicals in the implant area and lead to the encapsulation of the device [31]. Not only is this reaction medically unsuitable, but the BMI electrode devices are extremely vulnerable to changes in impedance and fail to function typically within months after encapsulation [31, 58-60]. Non-biocompatibility of the construction materials with the CNS tissue has been linked to this adverse reaction [31]. Si has been a favored construction material for BMI devices, but this material has long been known to elicit a negative response from chronic implantation, and Si is not chemically resistant to many biological chemical processes [31, 58-60]. Also, as these devices require an insulation material to electrically isolate the electrodes, and this layer contacts more tissue area than the substrate and electrode materials, the biocompatibility of that layer is paramount to acceptance of the device by the CNS [31]. Many of the devices using SiO_2 and Si_3N_4 as insulators have shown a incompatibility with the CNS, but polyimide, a chemically resistive polymer material which also incorporates many existing microfabrication techniques used for the construction of microelectrode devices, has shown the it has excellent biocompatibility [31, 61-63]. This material has been used as an insulating coating and substrate material for many BMI device designs which have

worked for extended periods without total encapsulation [61-63]. Although this material offers excellent biocompatibility, displaying a fibroblast adherence, growth, and spread comparable to polystyrene, it has major drawbacks that hinder its acceptance as the material of choice for BMI devices [64]. The material has a relatively high water uptake which decreases electrical impedance, and it is a very flexible material [31]. Although this flexibility alleviated the issue of micromotion, a problem associated with stiff BMI devices where the device's relative motion causes additional penetration and injury response cycles, the material is difficult to implant requiring deposition on a stronger material or complex surgical implantation techniques using wires or scalpels [31].

As stated in (§ 1.1), a semiconductor material, silicon carbide, may offer a different approach to the generation of implantable neural MEMS devices. The advantages of using this material will be covered in more detail in the next section.

1.5 Cubic Silicon Carbide (3C-SiC)

Silicon carbide is a physically strong material and is chemically inert making it ideal for interaction with the harsh body environment. Amorphous and polycrystalline forms of silicon carbide, a-SiC and poly-SiC, have been used as coatings for many implantable biomedical devices, and clinical studies for bone prosthetics and heart stents have confirmed the biocompatibility of these forms of SiC [16-18]. A recent application for a-SiC was to use it as a thin film coating for the Utah Probe neural prosthetic constructed from silicon [65]. The advantage of these forms of SiC is that they can be deposited at lower temperatures than single crystal SiC, but have strictly insulating

properties because of the large amount of crystalline defects present in the material [16-18, 21, 65].

Silicon carbide is a semiconducting material like Si, which enables the creation of complex electrical devices. SiC also is able to utilize many of the device processing techniques available to Si [21]. Unlike many semiconductors, SiC is a polymorphic material, having approximately 170 different crystal organizations, but sharing a common stoichiometry (i.e., all forms contain bi-layers of Si and C) [21]. Table 1.1 summarizes some of the physical and electrical properties of a few of the SiC polytypes alongside with Si. Two of the hexagonal polytypes of SiC, 4H-SiC and 6H-SiC, have been available commercially as substrate wafers, and have been fashioned into devices [66]. Light emitting diodes, LEDs, high power Schottky Diodes, and metal-insulator-semiconductor field effect transistor, MISFET, devices are all commercially available which utilize 4H-SiC and 6H-SiC [66]. These materials have been formed into electrode myocardial biosensors, and have shown good biocompatibility, non-toxicity, and low biofouling [19, 20]. However, 4H-SiC and 6H-SiC are much more difficult to fabricate into complex devices because of their chemical inertness and physical strength. The hexagonal forms of SiC require temperatures upward of 1600 °C for epitaxial growth, which makes incorporation with other materials very difficult [67]. As there is no ability to diffuse chemical dopants into the crystalline structure, SiC doping must either be done during the growth process or through ionic implantation and subsequent activation [21]. Etching of SiC is achieved using dry etching methods like reactive ion etching [21]. The effects of these difficulties mean that complicated integrated circuits that would be

necessary for the amplification, filtering, and radio transmission of neural signals is difficult at best to reproduce in hexagonal SiC.

Table 1.1: Electrical, thermal and physical properties of SiC and Si [70-72].

	3C-SiC	4H-SiC	6H-SiC	Si
Band Gap (eV)	2.36	3.23	3.0	1.12
Breakdown Field (MV cm^{-1})	1	3-5	3-5	0.25
Electron Mobility (cm^2 $V^{-1}s^{-1}$) at 300K	<800	<900	<400	1500
Hole Mobility (cm^2 $V^{-1}s^{-1}$) at 300K	<320	<120	<90	450
Thermal conductivity (W/cm-K)	5	4.9	4.9	1.5
Thermal expansion @300 K @1500-1600 K (10^{-6} K^{-1})	3.8 5.5	NA	4.3 $\perp$ *c* axis 4.7 $\parallel$ *c* axis	2.6 4.56-4.6
Young's Modulus (GPa)	300 to 700			47
Elastic Modulus (GPa)	433	424		170

Cubic silicon carbide, 3C-SiC, is the only polytype of silicon carbide with a zinc blended atomic structure [21]. With this cubic crystal structure, it can be heteroepitaxially grown on other cubic structure substrates, like silicon or diamond. Although 3C-SiC has an overall cubic structure, it is still formed by stacking alternating hexagonal bilayers which gives this structure the ability to be growth on the hexagonal forms of SiC [68, 69]. 3C-SiC offers an alternative to processing not available in other forms of SiC in that it can be grown on Si substrates which are affected by cheaper wet chemical machining techniques. The generation of free-standing mechanical structures such as springs, diaphragms, and cantilevers is easily achieved by etching through the 3C-SiC epitaxial layer to the Si using reactive ion etching and then releasing the structure

with wet chemical etching of Si. Etch stops can be added to the Si by p^{++} doping, ion implantation and activation of oxygen to create imbedded SiO_2, or the use of silicon on insulator (SOI) substrates [70]. 3C-SiC can also grown at much lower temperatures, approximately 1200 °C, which is much lower than the hexagonal forms of SiC and can allow integration with multiple material devices [71].

This material has many properties that make it ideal as a construction material for a neural interface device. SiC is much harder than Si and would offer the same strength with less material. This would mean that the ~ 15 µm thicknesses limitation for planar electrode shanks constructed from Si could be drastically reduced to a size limited by the amount of electrical components on the device [3]. As this material is a semiconductor and chemically resistant, interaction with neurons could be achieved through field effect devices instead of the electrode thereby ensuring capacitive interaction and reducing or eliminating metal contacting the body. Electrically, 3C-SiC possesses a wider band gap greater than twice that of Si and the highest hole mobility of the SiC polytypes which enables the production of field effect devices that have superior inversion characteristics and greater reliability than other SiC polytypes [70, 71]. 3C-SiC forms heterojunctions with Si and diamond which can be used to create bipolar transistors or MISFET devices with superior reliability and lower on-state voltages. As stated previously, generation of complex interconnected circuits would be required for an implantable neural interface, and 3C-SiC, like other forms of SiC, possesses the same doping limitations. However, as 3C-SiC is linked physically to Si through a heterojunction, the integration of the two materials electrically would only require the addition of conductive interconnects. This

would mean that the complex devices could still be generated in the Si and the neural device would be constructed on the interconnected thin film layer of 3C-SiC.

1.6 Nanocrystalline Diamond (NCD)

One problem with the use of FET devices is that they require an insulator to function. Silicon dioxide, SiO_2, has been the traditional insulator of choice as it is the native oxide of the dominant semiconductor Si. Silicon carbide also has SiO_2 as a native oxide, although the quality of the oxide is less than for Si [21]. This insulator has a large problem in that it is contaminated easily with metallic ions, like sodium, Na, potassium, K, and iron, Fe [12, 73-75]. Within minutes from being immersed in an electrolytic solution containing solvated ions like Na or K, the mobile ions are absorbed onto the surface of SiO_2 and begin to diffuse into the material [73, 74]. The speed of the diffusion is increased when an electric field is applied, and the ions are transported to the semiconductor surface where they are trapped [75]. Na or K ions trapped at the intersection between the semiconductor and the oxide attract electrons and make devices turn on prematurely and change the threshold voltage [76]. This problem would be even greater for a device that had no metal protection over the gate oxide, like one of Fromherz neural interaction FET's, as the oxide is exposed constantly to an electrolytic environment. Coating the silicon dioxide with another material that resists diffusion, for instance polyimide or phosphosilicate glass, is a possible solution to this problem. Unfortunately addition of materials can modify capacitance and Fromherz has shown that thin, high K materials are most desirable for the devices [15]. Also, it has been shown

that many types of glass do not possess a high level of biocompatible and can initiate foreign body immune response [77].

Table 1.2: Electrical, thermal and physical properties of diamond and SiO_2 [78-82].

	Diamond	SiO_2
Band Gap (eV)	5.47	~ 9.0
Breakdown Field (MV cm^{-1})	10	60
Resistivity (Ωcm)	10^{-3} to 10^{14}	10^{13}
Relative Dielectric Constant	5.68	3.9
Thermal conductivity (W/cm-K)	$20 - 150_{max}$	0.014
Thermal expansion @300 K	0.9	$5x10^{-7}$
Young's Modulus (GPa)	110	14.4 – 18

Diamond has been drawing interest for many applications due to its chemical, mechanical, and electrical properties. As a semiconductor that is composed of only carbon, an element common to biology, this material has been shown to have good biocompatibility [78]. As an extreme wide band gap semiconductor, diamond has the possibility of being both a good insulator and a good conductor depending on doping levels. Many of the properties of diamond are displayed in Table 1.2 with silicon added as a contrast. Diamond has the best thermal properties of any material and it provides superior material strength being the hardest substance known to man [78, 79]. Diamond, unlike silicon dioxide, is virtually chemically inert would not suffer the trap incorporation by ionic diffusion experienced by silicon oxide when placed in an electrolyte, so it could be utilized as a possible insulator in a FET device. Single crystalline diamond is expensive and difficult to produce, but nanocrystalline diamond, NCD, can be deposited

on many materials using plasma assisted chemical vapor deposition at relatively low temperatures, approximately 700 °C [78]. This would be a good insulator for a MISFET device that would include NCD as the insulator and 3C-SiC as the substrate base.

Although NCD provides potential solutions as an insulator, its hardness and chemical resistivity make it difficult to process into devices. One method of etching diamond is to use oxygen plasma which also provides some selectivity as this would oxidize the SiC substrate which could be removed with HF [83]. The wide band gap of diamond makes it difficult to produce low resistance Ohmic contacts with metals, but this problem is not applicable to insulating NCD used for a Fromherz FET device which has a metal free gate [84]. To achieve a surface suitable for biological devices, the nucleation density must be greater than 10^{11} cm^{-2} to ensure that pinholes in the film are minimized and a low surface roughness is achieved [78].

1.7 Summary of Chapter

Damage to the CNS initiates the process known as glial scarring that essentially isolates and encapsulates the damaged area with a thick layer of cells (tissue). The effect of this is often the loss of motor or sensory abilities, and without the prospect of regeneration, this loss is permanent. One proposed therapy is to utilize a BMI device which would read signals from undamaged portions of the CNS, process the signal, and relay the signal to either a mechanical or computerized device or even to another undamaged neuron or electrically active cell. Two types of the devices have been developed. The first is a non-invasive device which reads signals through the scalp or

skin, but the reactions of these devices are slow and prone to error. Invasive, implantable devices have been developed that can use either conductive or capacitive coupling to the neural membrane to receive and send electrical stimulations called action potentials. These devices are much faster and targetable, but have a major biocompatibility issue that leads to glial scar encapsulation of the device. We propose that the two materials, 3C-SiC and NCD, may be possible biocompatible material platforms for the construction of an implantable neural device. In the next chapter, we will explore various methods of growth and deposition that were developed to achieve this type of device.

Chapter 2: Cubic Silicon Carbide and Nanocrystalline Diamond Material Development

2.1 Introduction

The construction of planar neural prosthetic probes requires the formation of sharp shanks through processes which require sacrificing large amounts of bulk material, or the epitaxial growth of a material upon bulk wafer materials and the subsequent removal of the thin film. Cubic Silicon carbide, also known as β-SiC and 3C-SiC, is a thin film that can be grown epitaxially on Si through chemical vapor deposition (CVD). Unfortunately, unlike other forms of SiC polytypes, mainly the hexagonal forms 4H- and 6H-SiC, material development for this particular polytype is a work in progress and still requires more research in order to demonstrate electronic device viability. The reason for this situation is that the power and radio-frequency (RF) device industry has focused on the development of the 4H-SiC and 6H-SiC polytypes because the larger band gaps inherent with these materials was more desirable for their applications. Even with a lower band gap of 2.36 eV, 3C-SiC's major strength is it is the only form of SiC that has a cubic lattice, can be directly grown on Si substrates which are considerably less expensive than the hexagonal SiC substrates, and would allow for a straight forward electrical connection between devices on the 3C-SiC film with devices constructed in the silicon substrate.

3C-SiC, like its hexagonal and rhombohedral counterparts, is difficult to grow because of the high temperatures and lack of a stable liquid form of SiC, but has an additional burden of being one of the metastable forms of SiC [70, 71, 85]. SiC has equilibrium states with 2H-SiC and 6H-SiC forms but not with the 3C-SiC polytype. 3C-SiC is metastable over a large temperature range, from ~ 1000 °C to temperatures greater than its sublimation point of 2700 °C, which makes it difficult for single crystal epitaxy [85]. Using Si substrates limits the temperature profile due to its melting point of 1410 °C and limits many of the SiC polytype formations, but this substrate material adds another set of difficulties for the growth of crystalline 3C-SiC. In 1959, W. G. Spitzer *et al.* was the first to document growth of 3C-SiC on Si by heating a Si substrate to 1300 °C in a mixture of methane and argon [86]. This method of growth, known as the chemical vapor deposition (CVD) method, which was developed by Spitzer *et al.,* is still the most widely used today for the heteroepitaxial growth of 3C-SiC on Si substrates [86-88].

The 3C-SiC heteroepitaxially grown on Si by Spitzer *et al.* included a wide array of crystalline defects due to differences in the atomic stacking structures and physical properties of the two materials [86]. Many of these crystalline defects still pose a problem to the quality of 3C-SiC grown using this method. A large, 22% lattice mismatch (α_{SiC} = 0.436 nm; α_{Si} = 0.543 nm) and the 8% thermal expansion coefficient difference between Si and 3C-SiC leads to island growth formation which can generate many major planar and linear defects within the 3C-SiC crystal structure [87]. A major planar defect is the stacking fault where one of the 3 Si-C bi-layers that form 3C-SiC polytype does not follow the regular stacking order during crystal growth [90]. This

defect leads to the planar twin, where the stacking fault defect does not correct itself immediately but becomes the new stacking order over many crystalline layer depositions [90]. For a FCC oriented crystal, these features tend to align along the {111} direction, and can be eliminated or reduced by using that crystalline direction for growth [87]. Another planar defect common with island growth is the anti-phase domain (APD) boundary. These defects occur where growth islands deposit along the same planar orientations but deposition occurs rotated about their planar axis with respect to one another, and a boundary will form when the islands grow together [90]. The 22% lattice mismatch creates a major linear defect known as the edge misfit dislocation where a linear group of atoms does not align with the lattice of the other crystal to relieve stress in the crystal [90]. This type of defect is surrounded by areas of tensile stress in the smaller lattice, like the 3C-SiC crystal, and compressive stress in the larger crystal lattice, like Si [90].

The temperature for the growth of 3C-SiC gives rise to three dimensional defects, namely the interface hollow void and the 'hillock' defect. Within the temperature range of 1300 – 1400 °C, which is close to the melting point of Si and commonly the optimal temperature for the growth of 3C-SiC, Si tends to diffuse from the substrate and is either incorporated into the developing 3C-SiC film or lost due to evaporation [91-93]. The missing material, or void, can give rise to many linear and planar defects further degrading the quality of the 3C-SiC crystal [91-93]. One major defect associated with the resulting interface void is the formation of defective, polycrystalline material on the

edge of the interface voids [93, 94]. This defect, commonly known as the hillock defect, propagates through the crystal as it continues to grow and emerges at the surface [93-94].

Although many of these defects do not hinder the physical strength of the 3C-SiC crystal, they will affect the electrical performance of the device [72, 90]. This chapter is dedicated to detailing the work that was done to reduce the defects in 3C-SiC through novel methods, improve the surface quality of 3C-SiC, and grow NCD on 3C-SiC. (§ 2.2) is dedicated to detailing the methods and processes developed for the heteroepitaxial growth of 3C-SiC on Si and the use of a poly-silicon on oxide layer stack to assist in decreasing the defects caused at the interface. (§ 2.3) describes methods of SiC surface modifications using hydrogen etching which were developed at the University of South Florida in collaboration with Max-Planck-Institut. Finally, (§ 2.4) will detail the deposition and characterization of NCD on 3C-SiC substrates.

2.2 Chemical Vapor Deposition Growth of 3C-SiC

The growth of 3C-SiC on Si substrates performed at the University of South Florida (USF) occurs within a low pressure chemical vapor deposition (CVD) reactor called MF2 which is based off the design of Kordina *et al.* [94, 95]. The MF2 reactor is constructed with the reaction tube in a horizontal position which allows gasses to flow laterally over the substrate. Susceptor (and thus substrate) heating is provided through magnetic induction by an induction coil excited with high power RF current produced at a frequency of 10 KHz. The harsh conditions of the reaction chamber and the high temperatures require an infrared pyrometer for the measurement of the susceptor (and

thus growth) temperature. The hot-wall reaction chamber is an amorphous SiC-coated graphite susceptor which is not actively cooled and instead supported carbon graphite foam insulation to maximize heating efficiency [95]. The reactor nominally runs at pressures from 50 – 400 Torr under the flow of a palladium purified hydrogen carrier gas, H_2, which transports the silane, SiH_4, and propane, C_3H_8, precursor reactants to the growth zone [95]. Nitrogen, N_2, hydrogen chloride, HCl, and methyl chloride, CH_3Cl, gasses are also available for growth processing, while argon is used as the purge and cooling gas [94].

2.2.1 Establishing a Low Pressure Process for CVD 3C-SiC Growth

Thin layers of high quality crystalline 3C-SiC are required for the generation of a neural prosthetic device, so our material research focused on the goal of improving the crystalline quality of 3C-SiC grown on Si by improvement of the carbonization process. To achieve this purpose we examined growth of 3C-SiC on different orientations of the Si crystal, namely (100), (111) and (110), under both atmospheric and low process pressures [96]. Prior to 2007, the carbonization stage of the epitaxial growth of 3C-SiC was conducted at 760 Torr which was followed by growth at low pressure (~ 100 Torr) [22]. Apart from the obvious hazards of performing this CVD process at atmospheric pressure, some improvements reported in the literature justified the investigation of lower pressure for carbonization [89, 91-93]. At atmospheric pressure, the elevated partial pressure slows the evaporation of Si as the temperature is increased, decreasing the generation of interface voids, however the voids are much larger than found at lower

pressures as the growing 3C-SiC parasitically removes more material from the substrate [92]. Although void generation is much greater at lower pressures as evaporation tries to establish a saturated vapor pressure, the voids are smaller than those generated at atmospheric pressure [92]. The slower removal of reaction products at atmospheric pressure increases the generation of defective materials which deposit onto the surface of the crystal and become hillock defects, a defect that is rarer at lower pressures [92]. Atmospheric carbonization allows for enhanced three dimensional growth, otherwise referred to as island nucleation that was covered in (§ 2.1), whereas lower pressure allows for more two dimensional growth, known as step flow growth where the growth occurs in cohesive layers across the entire growth surface (plane) [89]. Island growth produces a larger quantity of stacking faults, twins, and dislocation defects which only begin decreasing in number with thick films greater than 17 µm, whereas lower pressure carbonization and growth decreases the planar and linear defects and reduction occurs within 5 µm of the growth films [89].

Our group at USF uses a modification of the original three stage process created by Nishino *et al.* in 1987 which consisted of a separate surface etch process followed by a single carbonization and growth stage [88]. Figure 2.1 shows the current growth process developed at USF for the growth of 3C-SiC on Si substrates. Removal of the native oxide is critical as 3C-SiC will not develop on any oxidized surface [86-88]. Nishino's process used an initial HCl etching stage to remove the oxide and clean the surface of the Si substrate, but we have discovered that we could combine this stage with the carbonization stage without affecting crystal growth [22, 88].

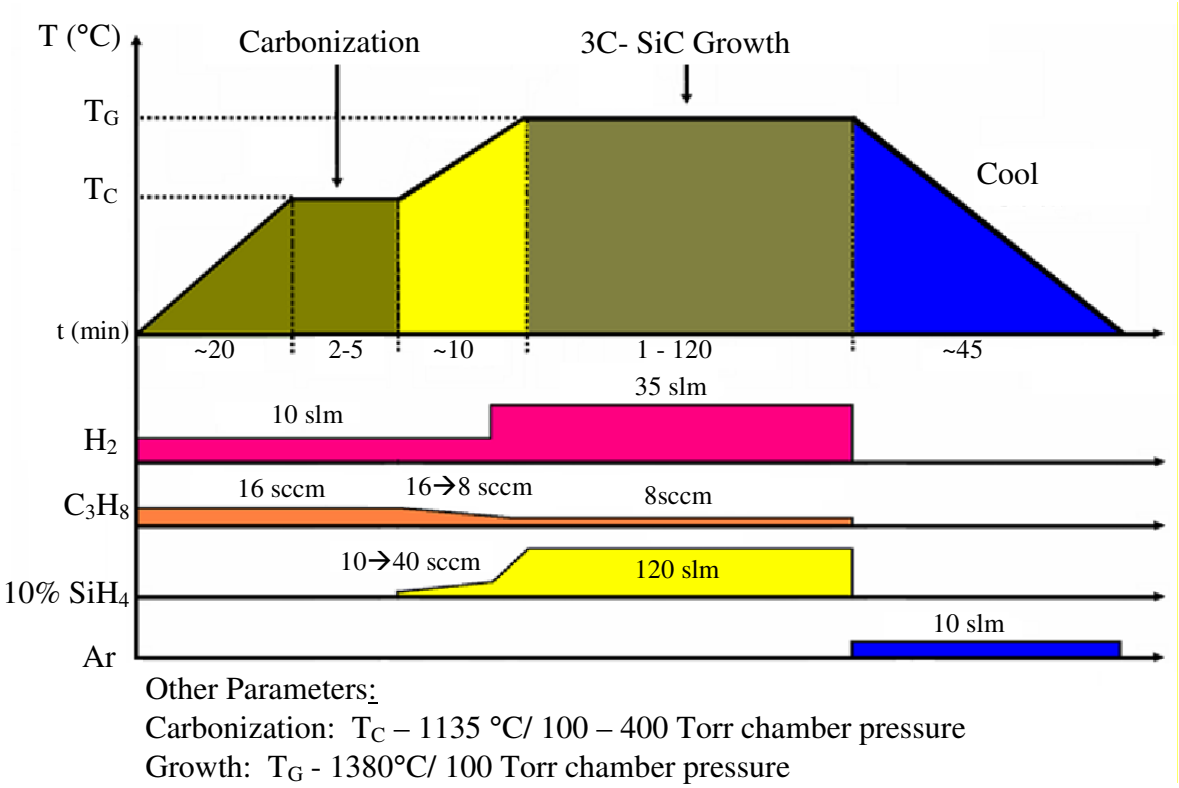

Figure 2.1: A generalized graph displaying the general process schedule developed at USF for the growth of 3C-SiC on Si substrates. Two distinct stages are indicated, namely the carbonization and the growth stage. Gas flow, temperatures, time, and pressure for each stage are indicated.

The USF process begins by cleaning the Si substrate utilizing the well known RCA process with hydrofluoric acid, HF, immersion to remove adsorbed surface metals, organics, and the defect filled native oxide. The carbonization stage begins by evacuating the reaction chamber of gasses and refilling the chamber with H_2 to a pressure of 400 Torr [96]. The RF induction is started and the substrate is heated under a flow of H_2 and C_3H_8 [96]. Unlike the runs at atmospheric pressure, the carbon precursor had to be drastically increased to maintain the proper partial pressure above the substrate at the decreased carbonization pressure [96]. The etching provided by H_2 in the initial heating

and the increased temperatures allow for the removal of the few nanometers of oxide that have formed since the wafer chemical cleaning. Heating ramp speed can be modified by increasing or decreasing the power of the RF generator, but the normal time for this ramp is 20 minutes [95]. When the carbonization temperature is reached, which is normally 1135 °C, gas flow, pressure and temperature are maintained for two to five minutes [22, 95, 96]. The carbonization temperature, which is much lower than that for the optimal growth, is optimized to prevent the evaporation of the Si surface but high enough to allow C_3H_8 to undergo sufficient pyrolysis (i.e., molecular cracking). Propane pyrolysis produces reactive carbon species that travel to the surface of the Si substrate, react with the Si atoms there, and forms the initial layer of 3C-SiC [22, 86, 95, 96].

After the carbonization step has been completed the temperature is increased to the growth temperature, nominally around 1380 °C. Our new process deviated from the previous process in a few aspects. Although SiH_4 is still added to the reactor and the flow is slowly increased during the temperature ramp from the carbonization to growth temperature, our modification additionally regulates propane by slowly decreasing the flow as the temperature increases [95, 96]. Our rationale for this change is that propane requires much more energy to pyrolyze than other carbon containing gasses. The higher flow required at the lower carbonization temperature which maintains the proper partial pressures and carbon molar species will produce excess carbon species as the temperature approaches the growth temperature. The excess carbon does not have enough silicon to react with, as Si is the rate limiting species of the reaction, and will form C-C bonds to create graphitic carbon. Graphitic carbon becomes particulates which deposit on the

surface of the growing 3C-SiC crystal. The defects become incorporated within the crystal unless the flow, and therefore the amount of available carbon, is reduced [95, 96]. The addition of silane and subsequent flow is increased to provide enough Si to react with the increase in carbon species. Void defects at the interface which are not coated by the growing 3C-SiC film become a source of Si from the substrate, as 3C-SiC does not allow diffusion of molecules [22, 95, 96]. The Si for the reactions in the second ramp would be parasitically provided from the void defects discussed in (§ 2.1) without the additional Si provided by SiH_4 [22, 95, 96]. At 30 - 50 °C before the growth temperature, the SiH_4 flow is accelerated quickly to the final level required for optimal growth, the H_2 precursor flow is increased to push the reactive species to the optimal growth zone located over the substrate, and the pressure is further reduced to 100 Torr [22, 95, 96]. At growth temperature, optimally 1380 °C, the gas flow rates and reactor temperature remain constant for 1 to 120 minutes, where the latter is a limitation due to the exhaustion of the H_2 carrier gas bottle. At the end of the growth time, all process and carrier gas flows are ceased and replaced by Ar and the RF generator is powered down [22, 95, 96]. The Ar gas serves as a cooling mechanism by pulling heat away from the hot zone, and the cooling process is inherently slow due to the heat retention by the hot wall carbon foam insulation. The slow cool down is desirable as the thermal expansion coefficient mismatch will cause stress between the films if the temperature is lowered quickly resulting in film cracking.

2.2.2 Low to Atmospheric Pressure Carbonization Comparison

The epitaxial growth process for 3C-SiC detailed in (§ 2.4) was used for film growth on Si substrates with three different orientations: (100), (111), and (110). The quality of the films was compared for the carbonization stage using a PSIA XE-100 scanning atomic force microscope, AFM, and X-ray photoelectron spectroscopy, XPS.

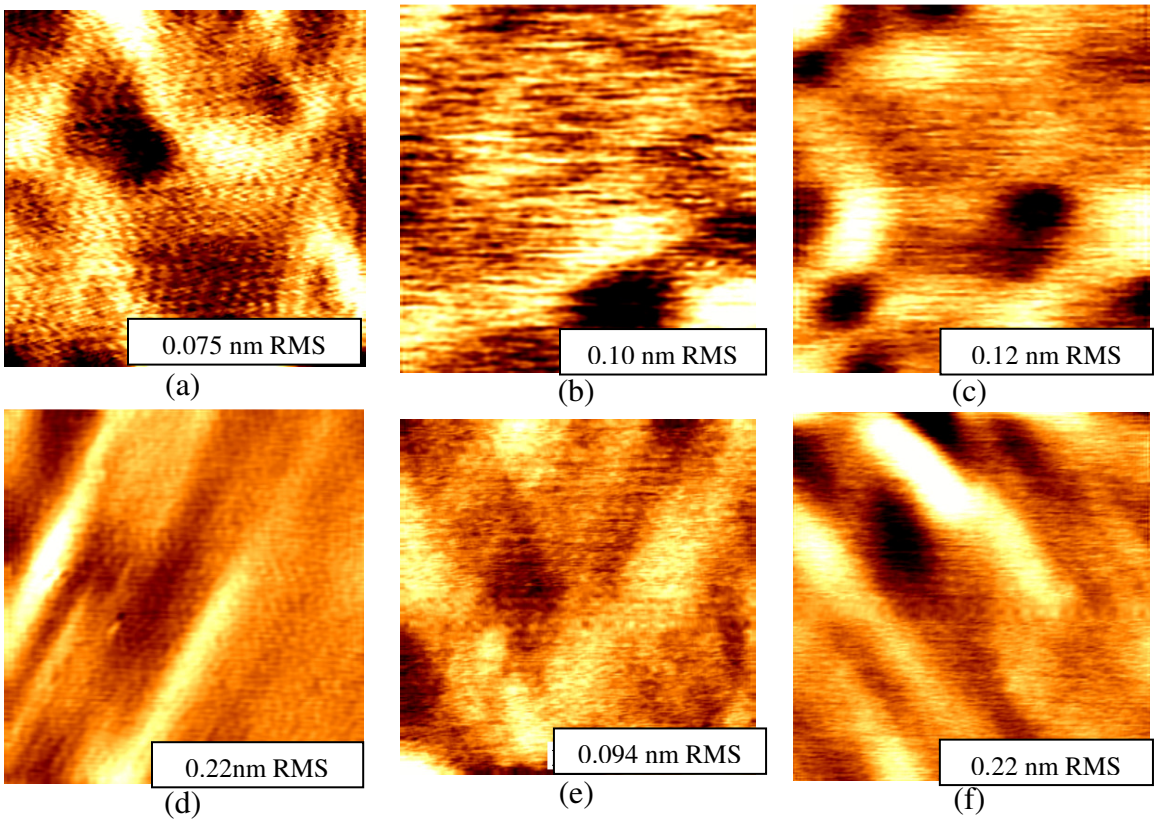

Figure 2.2: AFM micrographs of 3C-SiC on Si surfaces after the carbonization growth stage. (a-c) were performed at atmospheric pressure and (d-f) were performed at 400 Torr pressure. 3C-SiC samples (a) and (d) were grown on Si (100), (b) and (e) on Si (111), and (c) and (f) on Si (110). Surface roughness root mean square (RMS) values are located in the lower right corner. AFM performed in tapping mode with Al coated silicon cantilevers (2 x 2 μm).

The growth stage was characterized using AFM and transmission electron microscopy, TEM. Figure 2.2 shows selected AFM micrographs from the carbonization stage of the process. The upper row displays the results of atmospheric carbonization on Si (100), Si (111), and Si (110) from left to right, and the lower row shows scans for the same substrates at the lower 400 Torr pressure. Although the surfaces all have a similar surface roughness, r_q, immediately noticeable is that the three substrates have ~250 nm wide voids which are squared on the (100)Si and (110)Si surfaces and triangular on the (111)Si surface. The AFM micrographs of the low pressure carbonized (100) surfaces do not appear to have large void features, but are also not devoid of surface features. Small voids on the order of 25 – 50 nm are present on the surface and are difficult to see with these scans due to their shallow depth. The (111) and (110) substrates did not display a large change from carbonization between atmospheric and low pressure.

Table 2.1: XPS data of 3C-SiC films grown on various Si surfaces after 400 Torr carbonization.

		Binding Energy (eV)	(100)Si	(111)Si	(110)Si
C 1s	Survey	284.5	67.9%	42.2%	44.2%
	SiC (carbide)	283.5	15.8%	21.1%	18.1%
	Graphite	284.6	26.8%	14.5%	12.7%
	C-O complex	285-287	25.3%	6.6%	5.6%
Si 2p3	Survey	103.3	16.1%	31.3%	28.3%
	SiC (carbide)	101.4	15.0%	23.3%	20.9%
	Silica	103.4	1.1%	5.8%	6.0%
	Si	99.7	---	2.2%	1.4%
O 1s	Survey	---	16.0%	26.5%	27.5%
	Si/C ratio	---	0.95	1.10	1.15

XPS utilizing an aluminum source was used to gather the data shown in Table 2.1able 2.1. All samples show peaks associated with silicon carbide: C 1s, Si $2p^3$, and O 1s. The C 1s peak can be broken down into 3 components, SiC, graphite, and C-O complexes, and the Si $2p^3$ peak is composed of SiC, silica, and Si. The O 1s peak is associated with oxides. The table suggests that the 3C-SiC film grown on (100)Si contains much more graphite and carbon-oxygen complexes on the surface as compared to the other surfaces which contain much less quantities of these species. The (111) and (100) surfaces reveal a greater percentage of surface atoms in SiC bonds, but also have considerably more silica and Si remaining on the surface. As voids provide a pathway to the Si substrate, this result and the AFM micrographs confirm the presence of more voids on the surface. The (100) orientation displayed no appreciable value for natural silica on the surface and may indicate that the entire surface is covered in SiC or other carbon species. Finally, the oxide percentage is larger on the (110) and (111) surfaces, than on the (100) surface. The XPS survey values were utilized to determine the optimal silicon to carbon ratio, Si/C, at the lower pressures. The ratio for the 3C-SiC on (100)Si is the same as utilized in the atmospheric growth process, and worked almost as successfully for subsequent growths using the low pressure process obtaining a growth rate of 15 µm/ hr. Later experimentation for the growth on (111)Si substrates show that the Si/C ratio of 1.10 is optimal for the growth on this substrate as well. A good process for growth on (110) Si wafers had never been developed before at USF.

Figure 2.3 shows AFM micrographs of the surfaces of the three Si substrates after one minute of processing at the growth stage. The (100) and (111) surfaces show an r_q

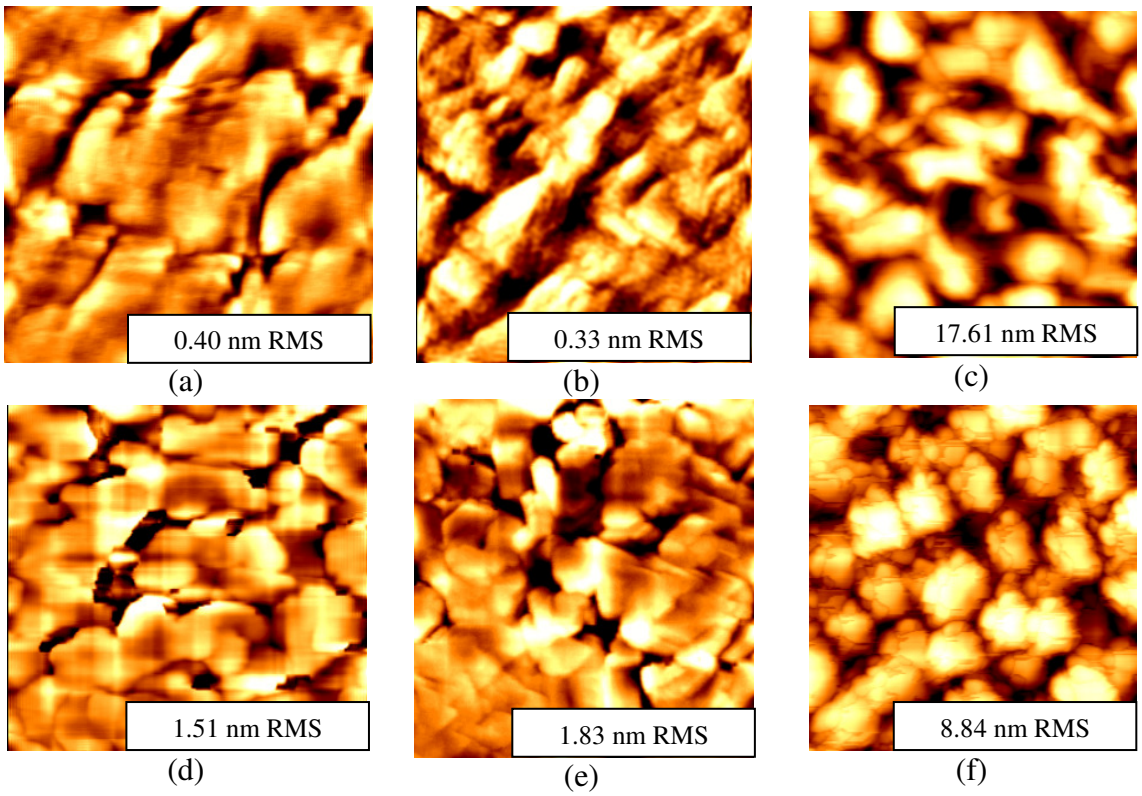

Figure 2.3: AFM micrographs of 3C-SiC on Si surfaces after 1 minute of the growth stage. All growths were performed at 100 Torr following carbonization of 760 Torr for (a-c) and 400 Torr for (d-f). 3C-SiC samples (a) and (d) were grown on Si (100), (b) and (e) on Si (111), and (c) and (f) on Si (110). Surface roughness root mean square (RMS) values are located in the lower right corner. AFM performed in tapping mode with Al coated silicon cantilevers (2 x 2 μm).

which is considerably less than that for the samples grown at low pressure; however the surface morphology does not differ much between the growths from the two carbonization pressures. The (100) 3C-SiC shows a surface with a square mosaic growth pattern accompanied with the crack-like antiphase boundaries arising from anti-phase domains in the crystal. The (111) 3C-SiC shows the beginning of the regular triangular step pattern with edges bounded by the {110} direction. Both films grown on (110) substrates show groups of rounded clusters indicating that the film is not single

crystalline 3C-SiC. As indicated by the XPS, the growth was performed at a Si/C ratio of 0.94, which is not the optimal ratio for 3C-SiC growth on Si (110).

Although the AFM micrographs do not indicate many differences between the two processes, the TEM analysis confirms that the defect levels are decreased with lower pressure carbonization processes, as indicated by the literature in (§ 2.1). The plan view TEM micrograph shown in Figure 2.4(a) is for 3C-SiC grown using the atmospheric pressure carbonization process and displays very large and deep voids at the interface and the accompanying problem of increased defects in the area surrounding the voids. The large dark area above the voids indicates a highly defective crystal there and could indicate hillock feature formation. Planar and linear defects, which are abundant at the interface, continue extending through the crystal without a large level of reduction. On the other hand, the 3C-SiC crystal grown on (100)Si using the lower pressure carbonization process shows a different interface and defect concentration. Voids are much smaller at the interface, and large area defective material is not present around the void areas. The planar and linear defects are reduced in concentration much faster, many within 100 nm, generating larger areas of almost defect free material. Finally, the concentration of defects is confirmed by the selected area diffraction images. Both images show that the films are 3C-SiC, but the film grown with the atmospheric carbonization process is more diffuse, indicating some scattering effects from defects, while the image obtained for the low pressure carbonization process is very sharp and clear, indicating a higher quality crystal had been grown.

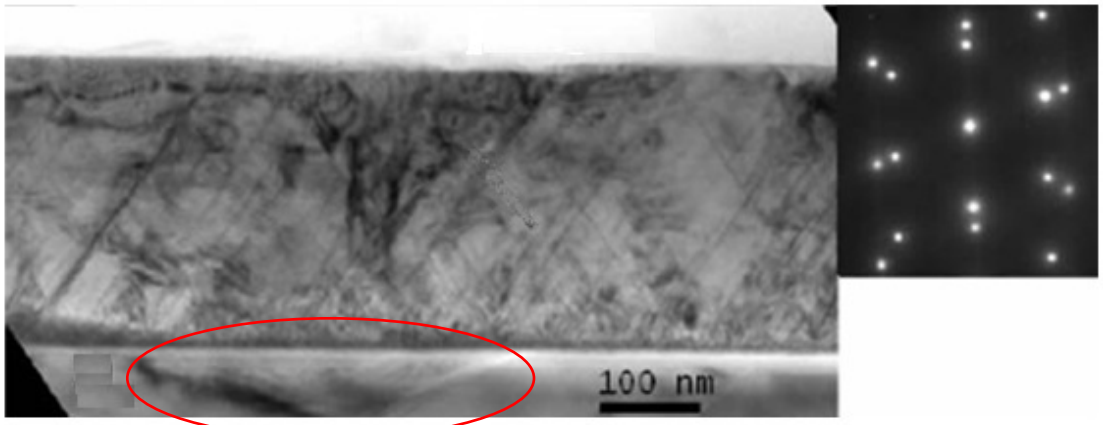

(a)

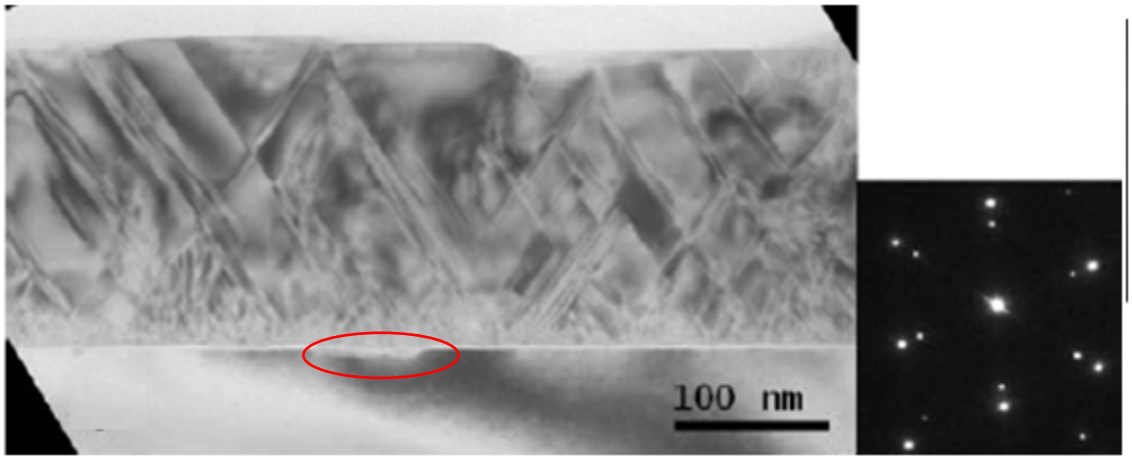

(b)

Figure 2.4: TEM plan view micrographs displaying growth of 3C-SiC on (100)Si using carbonization at (a) atmospheric pressure, and (b) 400 Torr. Interface voids on each substrate are circled in red. Selected area diffraction patterns of the crystal structures located to the right of the plan view micrographs show that the films are 3C-SiC, but that the growth associated with atmospheric pressure carbonization is more defective as evidenced by the more diffuse diffraction spots. TEM courtesy of Dr. Dr. C. Bongiorno of IMM-CNR in Catania, IT.

The low pressure carbonization process has led to a decreased amount of defects within the thin films of 3C-SiC grown on Si substrates. Crystal quality from the epitaxial growth using atmospheric carbonization, as measured by Phillips X'Pert Panalytical X-ray diffractometer, XRD, had the lowest full width of half maximum (FWHM) value reported at the time. The X-ray rocking curve taken on the SiC (002) diffraction plane

had a FWHM of 360 arcsec [22]. Using modifications of the low pressure carbonization developed by Frewin *et al.*, C. Locke *et al*. has reduced the defect level further and has reported the lowest FWHM value for any 3C-SiC film presently of 219 arcsec [96, 97].

2.2.3 Growth of 3C-SiC on Poly-Si/ SiO_2/ (111)Si

Growing a high quality thin film of 3C-SiC is only one of the necessary steps in the development of a planar neural interface system. The necessary electronic devices must be incorporated into the 3C-SiC film, and these electronics are constructed on the sharp needle-like shank probes that will interface with the neurons in the CNS system. SiC's resistance to wet chemical etching requires the use of dry etching through deep reactive ion etching/ reactive ion etching (DRIE/RIE) to achieve the release of these neuronal shanks [98]. Utilizing the Si substrate as a sacrificial layer for the creation of freestanding 3C-SiC structures is one common method to release the 3C-SiC layer [99-101]. We have worked on the generation of cantilevers constructed from 3C-SiC which were extremely resilient when released from the Si substrate, displaying only 9 µm bow (bending) over a 700 µm long, 20 µm wide and 2 µm thick cantilever [100]. Unfortunately, there were many problems associated with the controlled release of the cantilevers as many remained connected to unetched Si material below the structure [99, 100]. Earlier, our group had looked into forming other mechanical devices using 3C-SiC grown into Si molds, but epitaxial growth at reasonable growth rates within the mold and sidewalls would have eventually led to keyhole generation [101]. A further complication to this process is that recipes used to etch Si with DRIE/RIE have a similar etch rate with

SiC, thereby excluding selectivity and reducing accuracy for the desired structure [98, 102].

SiO_2 has been traditionally used as a release layer for Si MEMS technology and also serves as an etch stop for processing involving DRIE/RIE [103]. Unfortunately SiO_2 inhibits the growth of 3C-SiC thus 3C-SiC cannot be directly formed on oxide release layers (indeed SiO_2 has been used as a mask for selective 3C-SiC growth). Therefore another method is required that would allow the inclusion of an oxide release layer for 3C-SiC MEMS structures using Si substrates [86]. Silicon on insulator, SOI, substrates provide an excellent media for the creation of freestanding 3C-SiC devices by providing not only an oxide for the etch-stop for DRIE/RIE, but also a single Si crystal seed layer for the heteroepitaxial growth of the 3C-SiC.

SOI provides some additional benefits for the growth of 3C-SiC as shown in previous studies [104, 105]. The high temperatures required for the growth of single-crystal 3C-SiC softens the SiO_2 layer, allowing dispersion of stress caused by the 20% lattice mismatch, and the oxide provides mechanisms for the suppression of the formation of voids caused by Si evaporation at the 3C-SiC/Si interface [104]. The work at USF has shown that SOI seed layers (>50 nm) have produced 3C-SiC films that are as defective when compared to 3C-SiC films grown on single-crystal Si substrates [105]. The theorized benefits of the epitaxial growth of 3C-SiC on SOI were displayed when 3C-SiC is deposited on a thin (<50 nm) seed layer of Si, and the final product was excellent quality 3C-SiC [104, 105]. However, a major drawback of using SOI for the production

of 3C-SiC devices is the fact that it requires extensive processing techniques which add to the overall production cost of the device [104, 105]

For our experiments, we replaced the expensive SOI wafer with a stack of poly-Si/ SiO_2/ (111)Si, where the poly-Si would serve as the seed layer for the growth of poly-SiC. After the growth, we saw that our normal poly-SiC was not produced, which has a dull grey appearance, but Newton fringes were seen which usually indicated that we had achieved mono-crystalline 3C-SiC material. The resulting growth was nearly single-crystalline 3C-SiC that was comparable in quality to 3C-SiC grown on single-crystal Si in both the <111> and <100> directions. We theorized that the poly-Si was sufficiently thin and possessed an abundance of a particular crystalline orientation which would allow the 3C-SiC to completely convert the poly-Si into 3C-SiC. The oxide beneath it would serve as a stress release layer and allow the 3C-SiC to relieve defects at the interface level. This section details our new growth process using low process pressure and temperature and the resulting characterization of the 3C-SiC film with optical microscopy, AFM, scanning electron microscopy (SEM), XRD, and TEM.

Substrate preparation for the growth experiments was as follows. A (111)Si wafer was RCA cleaned, followed by the deposition of 5500 Å of thermally deposited silicon dioxide. After oxidation, a 20 to 50-nm-thick film of poly-Si was deposited by LPCVD at a temperature of 610°C and a pressure of 300 mTorr [106]. This process was chosen from the various poly-Si recipes for many reasons. The first is that a compressive stress is produced between the resulting poly-Si film and the oxide layer, which should help bring the Si crystal lattice into greater compliance with the 3C-SiC crystal lattice

[107]. A secondary reason for the growth of poly-Si at this temperature is that it generates large columnar Si grains textured in the <110> direction with a minor presence of grains textured in the <111> and <311> directions [106, 107]. The resulting thin poly-Si film was characterized by both AFM and XRD to ascertain the starting growth surface properties.

The AFM micrograph displayed in Figure 2.5(a) shows a surface with grains of average area ~5.5 nm^2, having an average surface roughness of 0.49 nm rms, but also indicated the presence of pinholes in the surface. The XRD measurements were performed on a Phillips X'Pert Panalytical Diffractometer operating at the Cu-Kα line, and the measurements indicated alignment of the grains along the <110>, <111>, and <311> directions, as was expected from the literature [106, 107]. The pinholes created difficulties during the deposition of 3C-SiC by creating a pathway for the softened glass to flow onto the growth surface thus destroying the 3C-SiC film morphology. This problem, displayed in Figure 2.5(a), existed on all growth attempts until the growth temperature was reduced to eliminate this problem, resulting in a maximum growth temperature for 3C-SiC on the film stack of 1200°C.

The final optimized growth process is explained as follows. The poly-Si/ SiO_2/ (111)Si wafer stack was placed in the MF2 horizontal, hot-wall reactor heated by the RF induction of a SiC-coated graphite susceptor. The wafer was loaded into a molded poly-SiC plate to fix the position of the wafer within the reactor hot zone. This polyplate was then seated into a recess in the susceptor and the chamber was sealed and evacuated of residual gases. The chamber was then filled with palladium-purified hydrogen to a

pressure of 400 Torr. The remaining process is a modification of the same process covered in (§ 2.2.1). The pressure for the carbonization process was 400 Torr, and growth pressure was 100 Torr. The standard gases used for 3C-SiC growth were: palladium-purified hydrogen, H_2, which is used as the transport gas; propane (C_3H_8), which is the carbon precursor; and a 10% silane (SiH_4) premixed in hydrogen, which is the silicon precursor.

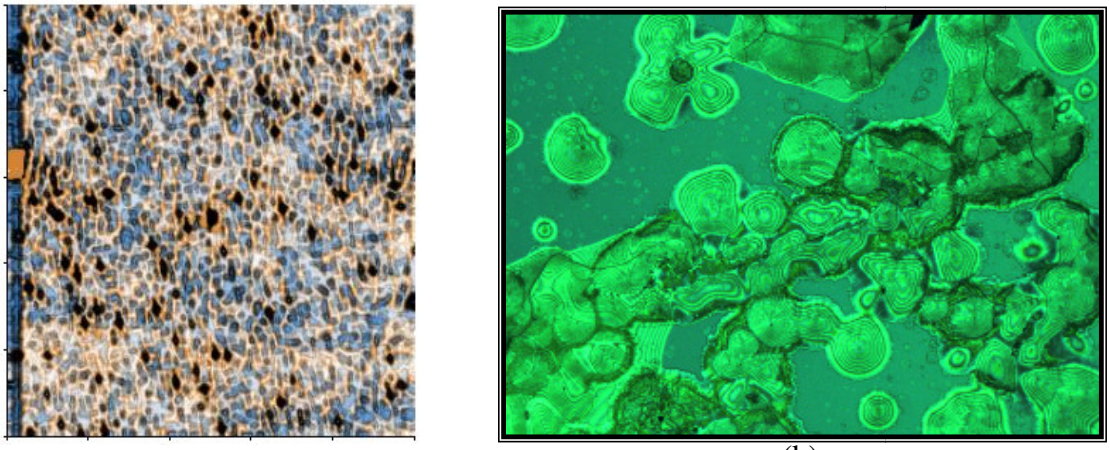

(a) (b)

Figure 2.5: (a) An 5 x 5 µm AFM micrograph of the surface of the poly-Si/ SiO_2/ (111)Si stack showing the pinholes in the thin film, and (b) shows an image from optical microscope obtained at 25X displaying the 3C-SiC growth on the poly-Si substrate stack using a growth temperature of 1250 °C. (b) shows the glass that became soft enough to flow through the pinholes in the poly-film and onto the surface.

The carbonization stage occurred while the sample temperature was ramped to 1000°C at a rate of ~ 35 °C/min. Throughout the ramp a flow of 16 sccm of C_3H_8 was maintained with a mass flow controller (MFC), and the H_2 carrier gas flow was maintained at 10 slm. Once the carbonization temperature was reached, the temperature was maintained for 3 min to attempt a full conversion of the poly-Si surface into 3C-SiC.

After carbonization and creation of the 3C-SiC template layer, the temperature was ramped a second time at a rate of 35°C/min to the growth temperature of 1200°C. During this ramp, we decreased the flow of C_3H_8 while simultaneously introducing and increasing the flow of SiH_4. At the growth temperature the input gas silicon to carbon ratio, Si/C, for the growth stage was 1.2. H_2 flow was maintained at 10 slm until 30°C before the ramp was completed, where it was increased to 25 slm, and the pressure was reduced from 400 Torr to 100 Torr. The temperature and gas flows were then held constant, allowing the continued epitaxial growth of 3C-SiC on the carbonized poly-Si template layer. The lower temperature process parameters produced a growth rate of 3.0 µm/ h near the front (upstream side) of the wafer, and 2.5 µm/ h at the rear (downstream side) of the wafer due to precursor depletion and the lack of in-situ wafer rotation. The growth rate was measured using an Accent QS-1200 FTIR system. Using the same low temperature and pressure process, the growth rate was also verified using samples of 3C-SiC grown on single-crystal Si oriented in the <100> and <111> directions.

2.2.4 Characterization of the 3C-SiC on the Poly-Si Stack

AFM surface analysis was used to further characterize the films as shown in Figure 2.6. The growth of 3C-SiC on the poly-Si/ SiO_2/ (111)Si substrate was compared with 3C-SiC grown directly on (100) and (111)Si substrates. The morphology for the surface of the 3C-SiC on the poly-Si stack is similar to that of the 3C-SiC grown on Si (111), showing large triangular domains with boundaries created by stacking fault and grain boundary defects. The AFM micrograph on the 3C-SiC grown on (100)Si has

smaller and more disassociated island growth, possessing square grain morphology. Improvements to the lower pressure process made by Locke *et al*. improved the quality of the 3C-SiC grown on (111)Si at the lower 1200 °C temperature [108]. The AFM data of this process show that 3C-SiC on (111)Si morphologically resembles 3C-SiC growth performed at 1380 °C, but Figure 2.6(a) resembles the morphology obtained with Figure 2.6(e) unfortunately indicating that the process is not single crystalline.

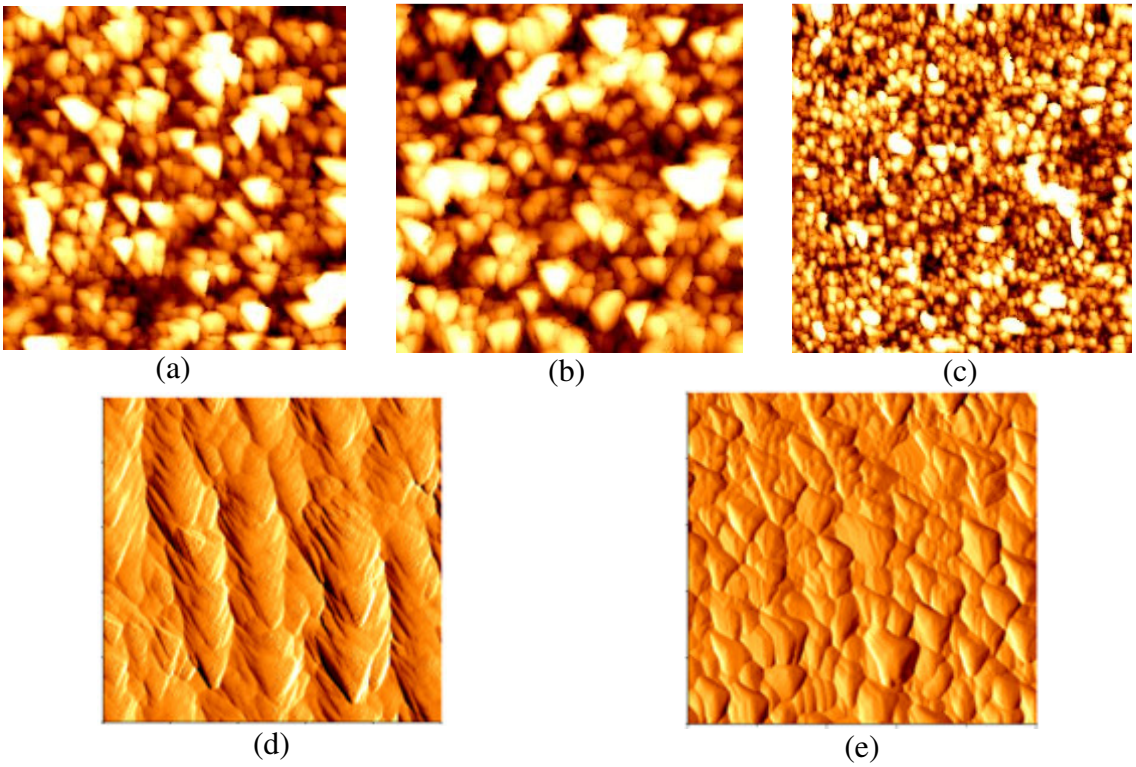

Figure 2.6: AFM micrographs showing a comparison of 3C-SiC grown on the surfaces of (a) poly-Si/ SiO_2/ (111)Si, (b) (111)Si, and (100)Si. Data taken in contact mode using a silicon nitride tip and a scan area of 5 μm by 5 μm. The average surface roughness, r_q, of the samples is: (a) 17.9 nm rms; (b) 26.5 nm rms; (c) 6.57 nm rms. AFM micrographs of (d) 3C-SiC on (111)Si and (e) 3C-SiC growth on p-Si/ SiO_2/ (111)Si utilizing the improved lower temperature process developed by Locke *et al.*, [108]. .Note that the grown film on the poly-Si substrate stack exhibits triangular surface morphology typical for 3C-SiC on (111)Si films. Growth of films (d) and (e) is courtesy of C. Locke, USF SiC group.

A cross-section SEM micrograph, obtained from a Hitachi 4800 microscope, displays the growth of 3C-SiC on the poly-Si stack is shown in Figure 2.7. This cross-section micrograph shows that the thickness of the 3C-SiC film grown for 20 min on the poly-Si stack is ~1.3 μm, which supported the film thickness measurements made by FTIR. An important aspect of this growth process is that the oxide remained perfectly intact and appeared to be unaffected during the growth of the 3C-SiC.

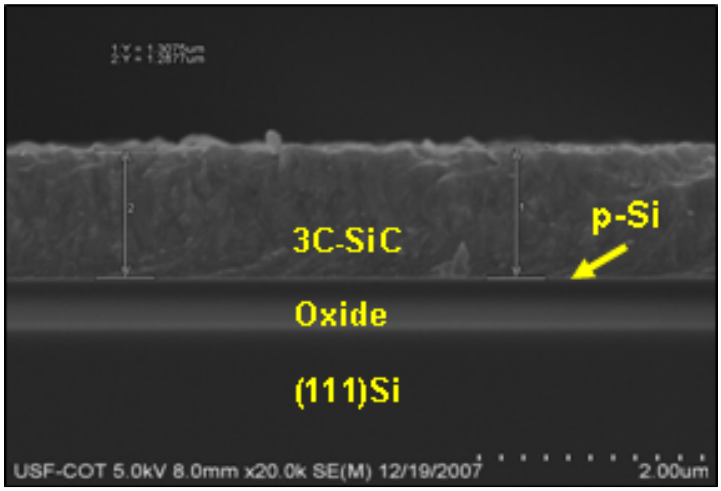

Figure 2.7: Cross-section SEM micrograph of the 3C-SiC film on the poly-Si/ SiO_2/ (111)Si stack (20 min growth time). The 3C-SiC grown has a thickness of ~1.3 μm and the SiO_2 a thickness of 0.55 μm. The thickness of the poly-Si, measured by a Rudolph AutoELIII ellipsometer (prior to 3C-SiC growth), was 20 nm. Note that the growth of 3C-SiC on the thin poly-Si seed did not affect the oxide layer.

Figure 2.8 shows the XRD θ-2θ diffraction surveys and high-resolution rocking curves performed for the 3C-SiC films grown on poly-Si/ SiO_2/ (111)Si, (111)Si and (100)Si substrates, and the resulting data is utilized for determination of the crystal orientation and quality of the 3C-SiC layer. Two scans were obtained for the 3C-SiC film grown on the poly-Si/ SiO_2/ (111)Si stack. The first scan, shown in Figure 2.8(a), is

from the film of the wafer grown near the gas inlet of the reactor where the film had a cloudy appearance. This film shows a strong peak observed at 35.6º and a weak peak at ~71.894º. The peaks indicate the reflections from the (111)3C-SiC and (311)3C-SiC planes, respectively. A comparison of the relative peak intensities suggests a preference for grain alignment in the <111> direction, little growth oriented along the <311> direction grains, and an absence of growth along the <110> direction.

Figure 2.8(b) shows a survey from the downstream half of the 50 mm wafer. This wafer has only the peak observed at 35.6º indicating the reflections are from the (111)3C-SiC oriented grains. This film has no appreciable reflections from the <311> and <110> grains. The surveys of the 3C-SiC film grown on (111)Si and (100)Si, displayed in Figure 2.8(c) and Figure 2.8(d) respectively, show dominant peaks at 35.6° for the (111)3C-SiC and 41.4° for (100)3C-SiC which indicate monocrystalline film growth.

The rocking curves were taken at the primary Bragg peak of the 3C-SiC epitaxial films and can be used to determine general film crystallinity. The insets displayed in Figure 2.8 show the results of the rocking curves obtained for each substrate type. The rocking curve for the 3C-SiC films on the poly-Si/ SiO_2/ (111)Si substrate displayed a FWHM of 0.192º (691″) upstream and 0.115º (414″) downstream. The FWHM evaluated from the 3C-SiC on (111)Si was 0.134º (482″). The rocking curve for the 3C-SiC on (100)Si displayed a slightly better result than the film grown on (111)Si, with a FWHM value of the 41.4° peak of 0.128º (460″). The correlation of the FWHM values from the growth performed on poly-Si/ SiO_2 / (111)Si versus the growth performed on single-crystal Si appears to suggest that all films have relatively comparable crystallinity. This

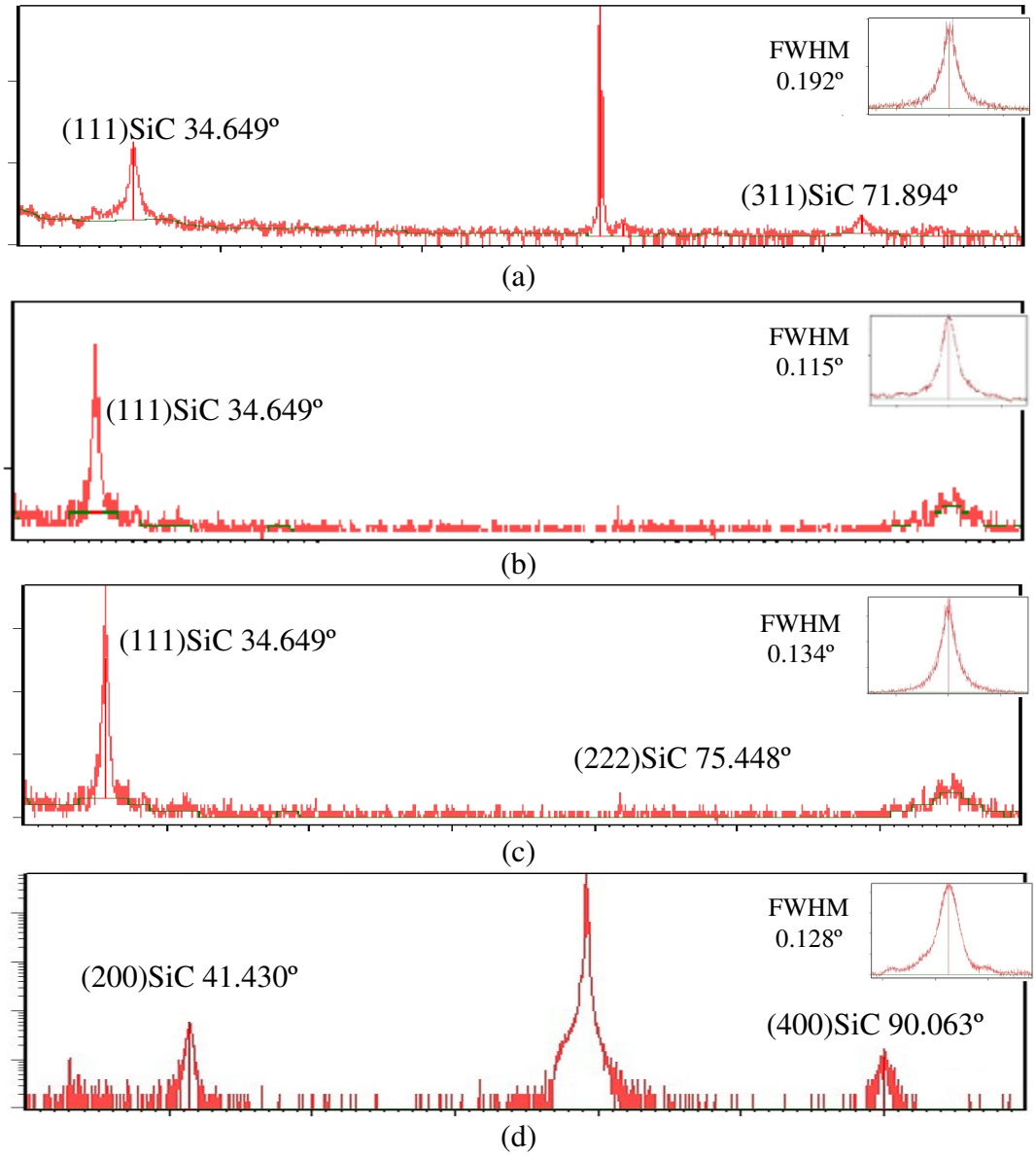

Figure 2.8: XRD θ-2θ diffraction surveys for the 3C-SiC films grown on (a-b) poly-Si/ SiO_2/ (111)Si, (c) (111)Si, and (d) (100)Si substrates. The XRD θ-2θ diffraction surveys show that (a-c) possess a primary peak at 35.6°, and (d) possesses a primary peak at 41.4°. Insets: rocking curves for each of the 3C-SiC films taken at their respective primary Bragg peaks. The FWHM values are 0.192º (691″), 0.115º (414″), 0.134º (482″) and 0.128º (460″), respectively. XRD courtesy of C. Locke, USF SiC group.

correlation proves to be very interesting because the growth of the 3C-SiC film on the poly-Si/ SiO_2 / (111)Si stack began on a poly-Si seed layer. When compared to 3C-SiC

films grown on SOI of similar Si seed layer thickness (50 nm) and 0.5 μm of SiO_2, the reported FWHM value was 0.20° (720″) [104],which is almost double the FWHM of the 3C-SiC grown on the poly-Si seed reported in this work. One aspect of the XRD data opened up some questions about the results obtained. The peak intensities of the 3C-SiC film grown on the poly-Si/ SiO_2/ (111)Si substrate had unusually low counts as compared to the 3C-SiC films grown on single crystal Si substrates. TEM was consulted to examine the films in more detail so as to try and understand the origin of this reduced XRD signal intensity.

TEM analysis performed at IMM-CNR in Catania, Italy by C. Bongiorno is displayed in Figure 2.9. The selected area electron diffraction pattern shown in Figure 2.9(a) does not show the clear 3C-SiC diffraction pattern displayed in Figure 2.4(b), but shows multiple rings which is indicative of polycrystalline material. The bright field plan-view of Figure 2.9(b) indicates a large amount of different grains present at the surface of the sample. TEM indicates that the samples are actually polycrystalline in nature, and explains the results of the AFM surface scan displayed in Figure 2.5(e).

The data from all of the analysis made seems to indicate that the growth of 3C-SiC on the poly-Si/ SiO_2/ (111)Si substrate is not single crystalline as first thought, but polycrystalline. However, the results of growth on this substrate suggest some interesting dynamics that should be explored at a later date. First, the poly-Si utilized for this growth had an overwhelming amount of grains along the <110> direction, with only minor grains along the <111> and <311> directions, however the growth was almost exclusively observed to be along the <111> direction and possessed no <110> grains as indicated by

AFM and XRD. Even though TEM data indicates the film is polycrystalline, the XRD indicates a weak single peak for (111)3C-SiC. This result may be explained by the fact that the {111} family when oriented about a fixed axis has eight different directional positions. The 3C-SiC crystals growing on the surface may align along any of these directions which explains the TEM bright field view and the AFM surface scan which show a surface full of many different individual crystal grains.

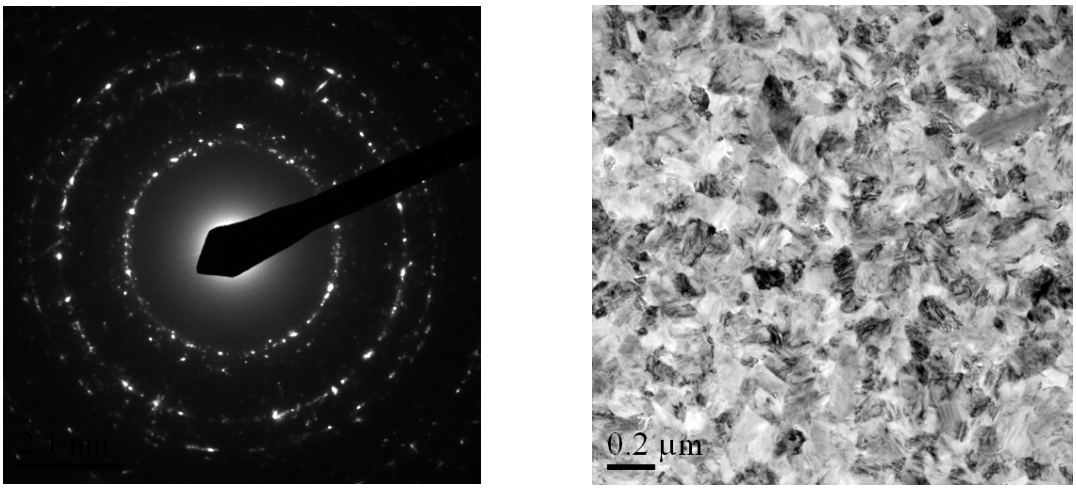

(a) (b)

Figure 2.9: TEM data taken in plan-view from sample USF2-07-170B, which is a 3C-SiC film grown on the 20 nm thick poly-Si substrate stack. The resulting (a) selected area diffraction and (b) plan-view are displayed. Unfortunately this data shows the film is polycrystalline in microstructure. Note this is not an issue for the MEMS application but for possible use in electronic devices. Data provided by C. Bongiorno, IMM-CNR, Catania, Sicily (IT).

In summary, a single crystalline film of 3C-SiC has been successfully grown on a poly-Si/ SiO_2/ (111)Si wafer and the process results verified multiple times. This process was developed to create a true 3C-SiC on oxide, or 'SiCOI' process, where the thin seed layer is completely converted into SiC for use in MEMS applications. The resulting films

were thought to be single crystalline in structure and their quality assessed using AFM, SEM, and XRD analysis. The analysis suggested that the films were single crystalline, but the addition of data from TEM analysis showed the resulting films were polycrystalline. Although this process will not allow for the incorporation of the electronics required for an implantable neural interface which utilizes field effect devices, we believe this process will have great importance for implantable electrode MEMS applications utilizing the SiC material solely for mechanical purposes. The cost-effectiveness and relative ease for the deposition of the oxide, poly-Si, and even poly-SiC layer make this process superior to the methods that utilize fabricated SOI substrates. Indeed if the neuronal implant electronics are realized within the Si substrate itself, then there appear to be no drawbacks to using this technology to create a fully-functional BMI device in the near future.

2.3 Hydrogen Etching of SiC Polytypes

Previously (§ 2.2) new techniques utilizing a CVD reactor for the epitaxial growth of 3C-SiC on Si substrates was discussed. These growth techniques were focused in generating a superior material for the fashioning of MEMS devices. 3C-SiC is an excellent material for this application due to its superior material properties, but as a semiconductor, it offers the bonus of being an 'all in one' MEMS material. Unlike other semiconductor materials, like Si, this material has only been researched scientifically within the last 50 years. This section is dedicated to the improvement of this extraordinary material for electrical devices.

An important consideration for electronic devices is the maintenance of the integrity of the material during processing so as to gain optimal yield from the finished device [109]. The surface of the semiconductor plays an integral role in device statistics, as it is the interconnection point of a device in contact with other materials, like epitaxial layers or metal conductors required for the device. Defects present at the surface must be reduced or eliminated for maintenance of electrical integrity and to avoid electrical traps generation, and atomically flat surfaces present a surface with available bonds ready for material integration [109]. However, these dangling bonds actively want to react with other materials present in the environment, which adds parasitic charge to the surface/interface or potentially traps defective material within layers of the device during fabrication and decreases the device efficiency [109]. 3C-SiC and Si will actively react with oxygen in the environment to create an oxide on the surface of the semiconductor. Surface passivation is a technique that places another atom or molecule on these dangling surface bonds to prevent oxide formation thus leaving the surface pristine for subsequent layer formation [109]. More importantly for this work, surface passivation has been a method used to attach complex organic molecules to the surface of semiconductors [20].

Crystals grown using the methods discussed in (§ 2.2) show mesa or terraced structures that are not completely flat. The atomic steps are produced by the alternating layers of carbon and silicon molecules on the surface. One method utilized by the semiconductor industry to maintain the flat surface required for integration of layers within a multiple layer device is chemical-mechanical polishing. CMP uses mechanical grinding, usually with diamond grit, alongside a chemical etching to equalize the levels

of features on a surface. Polishing has been used for the hexagonal forms of SiC for many years to achieve a mirror like surface, but as there is no wet chemical etchant for SiC, the surfaces remain scratched and highly defective. One method of removing polishing damage and creating an atomically flat, well ordered and passivated surface suitable for device fabrication is to etch the surface of the semiconductor using hydrogen gas etching [110]. Our group has also recently discovered that (100)3C-SiC can be passivated for long periods of time using hydrogen etching [111].

This section presents a comprehensive etching study, part of a collaborative effort between the University of South Florida and the Max-Planck-Institut in Stuttgart, Germany, that covers the three major polytypes of SiC. This work examines the previous techniques developed for 4H- and 6H-SiC, at both atmospheric and low pressure [112], as well as the work on (100)3C-SiC at atmospheric pressure [113], and reports a new low pressure etching regime for (100) and (111)3C-SiC.

2.3.1 Low Pressure Hydrogen Etching Process

We have developed processes which successfully etch the surface of the three commonly used polytypes of SiC through the use of an inductively heated hot-wall CVD reactor. First, all the samples were cleaned using the "piranha" clean followed by an HF dip and DI rinse. The CVD reactor was loaded with a hot zone specifically dedicated for H_2 etching , a requirement which was found to be critical in eliminating particulates from depositing on the substrate surface during the etch which originated from hot zone components previously used for growth processes [113]. The specifics for the etching

processes developed are summarized in Table 2.2. After etching, the samples were allowed to cool in a hydrogen flow of 10 slm until the temperature was well below 400 °C, which had been previously established as a necessity for stable surface passivation [111].

Table 2.2: Summary of hydrogen etching parameters for SiC surfaces [110-113].

SiC Polytype	Crystal Orient.	Wafer Axis	Polishing Type	Etch T [°C]	Etch P [Torr]	H_2 [SLM]	T [min]*
4H-SiC	(0001)	On- (Off-)	Optical	1400	760	10	20 (30)
4H-SiC	(000-1)	On- (Off-)	Optical	1500	760	10	20 (30)
6H-SiC	(0001)	On- (Off-)	Optical	1550	760	10	20 (30)
6H-SiC	(000-1)	On- (Off-)	Optical	1500	760	10	20 (30)
4H-SiC	(0001)	On- (Off-)	Optical	1400	150	3	5 (15)
4H-SiC	(000-1)	On- (Of)	Optical	1500	150	3	5 (15)
6H-SiC	(0001)	On- (Off-)	Optical	1550	150	3	10 (15)
6H-SiC	(000-1)	On- (Off-)	Optical	1500	150	3	10 (15)
3C-SiC	(100)	On-	As grown	1200	760	10	30
3C-SiC	(100)	On-	As grown	1200	100	5	10
3C-SiC	(111)	On-	As grown	1275	100	5	10

* First number listed is for on-axis substrates and number in parenthesis is for off-axis substrates.

2.3.2 Characterization of Hydrogen Etched SiC Surfaces

The experiments show that the surface damage caused by the mechanical polishing of 4H- and 6H-SiC wafers can be removed and an ordered surface of atomic steps revealed. Work on these substrates has been previously reported and Figure 2.10 shows two examples of etching using the parameters in Table 2.2 [110, 112]. For all hexagonal SiC samples, polishing damage was removed and the resulting surface displayed atomic steps of ~ 10 Å heights for 4H- and ~15 Å for 6H-SiC.

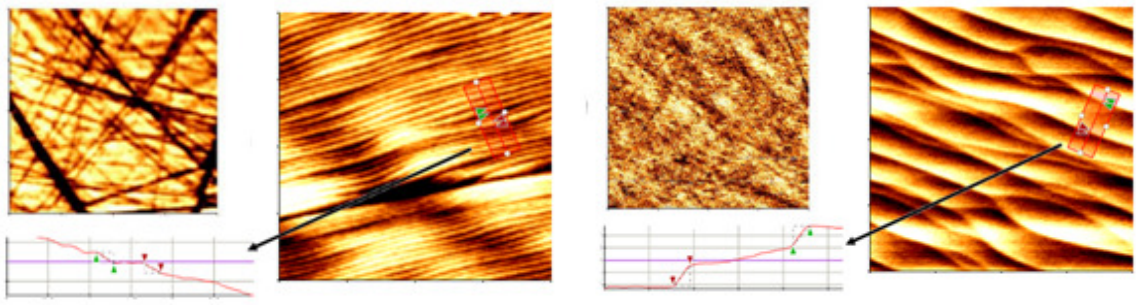

(a) (b)

Figure 2.10: 10 x 10 µm AFM micrographs of SiC surfaces displaying the surface before (left) and after (right) H_2 etches using the parameters from Table 2.2. Included is a measurement of the step height after etching. (a) On-axis 4H-SiC (0001) sample with a roughness of r_q = 0.396 nm. (b) On-axis (000-1) 6H-SiC sample with a roughness of r_q = 0.502 nm. AFM was performed in tapping mode on a Park Systems XE-100 AFM. Note that there are no morphological differences between atmospheric etching and LP etching.

Experiments were also performed on 3C-SiC epilayers which were grown on (100) and (111)Si using the CVD process described in (§ 2.2.1). The surfaces of the 3C-SiC crystals exhibited atomic-scale steps directly after growth. The (100)3C-SiC morphology displayed an inhomogeneous surface characterized by mesa growth within antiphase domains (APD), however within the APD's there were atomically flat terraces with small, wavy steps loosely aligned along the [110] and [-110] low-Miller indices.

Figure 2.11(a) shows an AFM micrograph of the surface of as-grown (100)3C-SiC which possesses steps of ~ 100 nm length and heights of ~2.5 Å, i.e. layers corresponding to the bi-atomic (2.18 Å) lattice of Si-C bonds, indicating a polar surface termination with either C or Si atoms. The APD's are measured to fall within 2 - 4 nm in height and 25 - 50 nm in width, and the surface roughness, r_q, was 6.38 nm. The surface of (111)3C-SiC displays a much more homogenous surface as seen in Figure 2.11(b). The regular terrace steps are loosely aligned along the [110] and equivalent directions.

One major difference of the surface is that, unlike (100)3C-SiC, APD's are not generated during epitaxial growth because (111)Si is the polar face of the 3C-SiC, although there are many linear defects that occur from twinning along the {111} crystal plane [114]. As noted before with (100)3C-SiC, the steps are not sharply aligned along the [110] Miller indices direction, but appear wavy and disorganized. The step heights measure ~ 8 or 16 Å along the tips of the terraces triangles and measure ~ 16 or 24 Å along the boundaries indicating step bunching occurring during the growth of the crystal. The surface roughness is r_q = 6.80 nm.

As we have previously developed an atmospheric pressure 3C-SiC H_2 etching process, we dedicated the final part of this study to develop and characterize a low pressure etching process [113]. Utilizing the previous study as a starting point for process etching temperature, (100) and (111)3C-SiC samples were etched at temperatures of 1200 °C, 1250 °C, and 1300 °C and the sample surfaces characterized via AFM to determine the effect of the etching. Figure 2.11(a) shows the 2.5 µm x 2.5 µm AFM scans of the (100)3C-SiC etched surfaces performed at each of these temperatures. Etching at 1200 °C shows steps that have increased order along the low-Miller indices, and the step edges are more squared and straight than the as-grown steps. The step heights on the surface were measured at ~ 1.8 – 2.5 Å and terraces ~ 75 - 100 nm long indicating that the surface still displays the atomic bi-layer surface characteristic of the as grown surface. Over etching of 3C-SiC surface defects is a large problem for H_2 etching, but the APD trenches were not affected significantly at this temperature, measuring ~ 2 – 4 nm in depth and ~ 25 - 75 nm in width. Overall the surface became more flat between

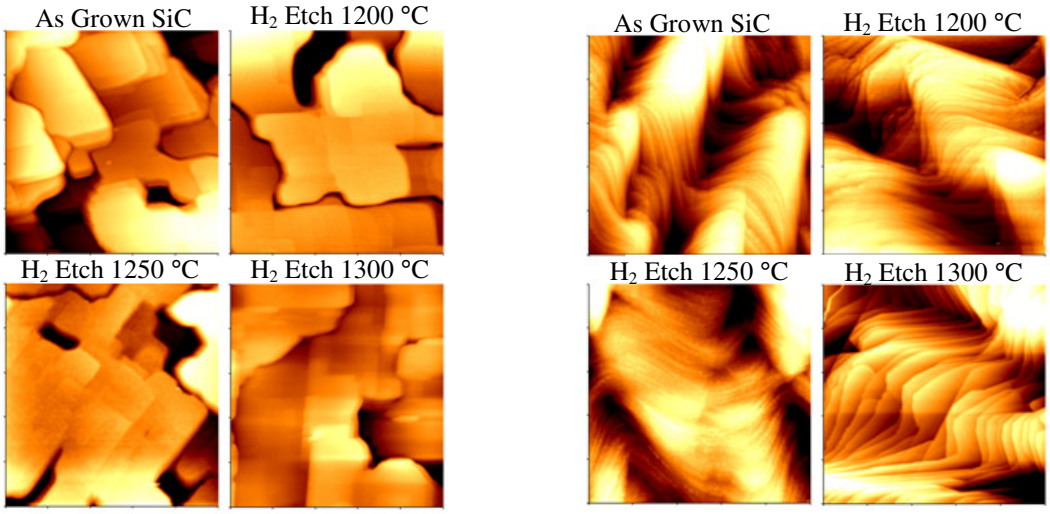

(a) (b)

Figure 2.11: AFM micrographs of (100)3C-SiC surfaces (a) epitaxially grown on (100)Si after subsequent H_2 etches at the temperatures indicated, and (b) AFM micrographs of (111)3C-SiC surfaces epitaxially grown on (111)Si after subsequent H_2 etches. All scans are 2.5 x 2.5 µm, and were done with silicon nitride tips using contact mode.

the varying surfaces as the r_q has been reduced to 5.7 nm. The (100)3C-SiC etch at a temperature of 1250 °C resulted in even more squared edges with steps along the same Miller indices; however many interior steps were measured at ~ 4 – 5 Å intermingled with steps of 2.5 – 3.0 Å, indicating that step bunching of the bi-layer steps was beginning to occur. Also noted was the appearance of inverted square pyramidal pits 3 - 5 nm deep, and the APD trenches have a slightly increased depth of 3 – 4 nm and width of 60 – 100 nm. However the etching further flattened the surface reducing the surface roughness to 4.93 nm. The (100)3C-SiC etched at a temperature of 1300 °C became more mosaic, was completely squared, and possessed step heights of ~ 4 – 12 nm and lengths of 200 – 400 nm. The etch pits increased in size and depth, many measuring over 100 nm wide and 7 nm deep. The APD trenches increased in width to 100 – 300 nm, but

have a reduction in depth to ~ 0.5 – 2.5 nm. This over-etched surface displays a great reduction in the surface roughness to 1.45 nm.

The H_2 etching of (111)3C-SiC results are shown in Figure 2.11(b). At 1200 °C, the steps on the surface still appear wavy and loosely aligned along the low-Miller indices. Steps along the apex of the step edge show a reduction in step height to ~ 7 – 8 Å or ~ 10.5 – 12 Å and steps along Miller index boundaries were reduced to ~ 11 – 12 Å or ~ 16.5 to 18 Å. Most terraces have a width of 25 – 50 nm, but there are some larger terraces present with widths of 75 – 200 nm. The surface roughness was only slightly improved with an r_q of 6.37 nm RMS. The H_2 etch at 1250 °C reveals a great number of steps measuring ~ 2.5 – 3.7 Å intermingled with ~ 4.8 to 6.7 Å steps along both the triangular apex and the edges of the terraces; however the step morphology still remains wavy and loosely aligned to the Miller-index boundaries. The terraces have relatively uniform with widths of 10 – 30 nm and the r_q is 3.77 nm RMS. At a temperature of 1300 °C, the morphology changed to straight steps with low-Miller indices alignment. Steps of heights ~ 6.5 – 8.2 Å, ~15.2 – 19.4 Å, and 22.3 – 26.6 Å appeared on all edges of the terraces, indicating a return to the step bunching as seen in the as-grown material. The terrace widths were increased along the Miller-index borders to 20 – 40 nm, and many of the widths along the triangular apex were increased to 150 – 400 nm in width. The surface roughness also increased to 4.78 nm RMS.

The results of this study show that the three major polytypes of SiC can be etched successfully at low pressure, which establishes a safe and more controlled process. The study did not electrically evaluate the surface band bending as was done by Coletti *et al.*;

however this process will eventually be quantified in the same manner by new members of the SiC group at USF [111].

2.4 NCD Deposition on 3C-SiC/ Si

The unique material characteristics of the two materials, 3C-SiC and NCD, present some unique solutions for the generation of high temperature, power, and high frequency MEMS devices. As semiconductor materials, 3C-SiC and NCD have very good electrical properties that can be utilized for the creation of electrical devices. The band gap difference and high carrier mobility for both of these materials generates a heterojunction that can become part of an extremely efficient and fast switching bipolar junction device [24]. As both of these materials are potentially biocompatible, the generation of permanently implantable MEMS devices is also a possibility. Single crystal 3C-SiC is normally heteroepitaxially grown on silicon using CVD methods previously discussed in (§ 2.1 - 2.2) and the process is extremely sensitive to both growth and substrate conditions. NCD, on the other hand, can be deposited on any material which is stable at the deposition temperature by using microwave plasma enhanced chemical vapor deposition (MPECVD) [115]. NCD deposited on Si substrates have many additional defects from the stress caused by the relatively large lattice mismatch [115]. Because the lattice mismatch is slightly less between NCD and 3C-SiC, deposition of NCD on 3C-SiC substrates has been proposed to help alleviate stress defects caused by the lattice mismatch (α_{Si} = 0.543 nm, α_{SiC} = 0.436 nm, and α_{NCD} = 0.357 nm).

The focus of this section is to characterize the deposition of NCD on 3C-SiC which has been homoepitaxially grown on (100) and (111)Si substrates and to evaluate the quality of the interface between the different layers. The characterization of the materials was performed using FTIR, SEM, TEM, AFM, XRD, Raman spectroscopy, and near edge x-ray absorption spectroscopy (NEXAFS).

2.4.1 NCD Deposition Process

The deposition of NCD on another material using a commercial IPLAS Cyrannus I MPECVD reactor requires some preparation stages. First the Si substrate is seeded with diamond nanoparticles. This seeding involves adding the deposition substrate to a slurry solution containing 1.2 g of titanium nanopowder, 1.2 g of diamond nanopowder, and 100 ml of methanol or acetone. The solution and substrate are left in an ultrasound bath for 20 minutes followed by two 20 minute cleaning cycles within only methanol. The samples are then removed and died with a N_2 gun. The diamond seeded substrates are placed within the MPECVD reactor where an Ar plasma is struck. The pressure of the deposition is 135 Torr, a temperature of 750°C and the microwave power is maintained at 1.8 KW. Methane, CH_4, is used as the carbon precursor and H_2 is used to control the size of the NCD grains. To grow intrinsic NCD, the CH_4 is 0.5%, the H_2 is1%, and Ar provides the balance of the gas used for the deposition which has a rate of ~0.17 µm/ hr. Samples of (100) and (111)Si as well as (100) and (111)3C-SiC were seeded and NCD was deposited for 3 hours. Measurements using FTIR showed an uneven deposition with film thickness ranging from 400 – 600 nm.

2.4.2 Material Characterization

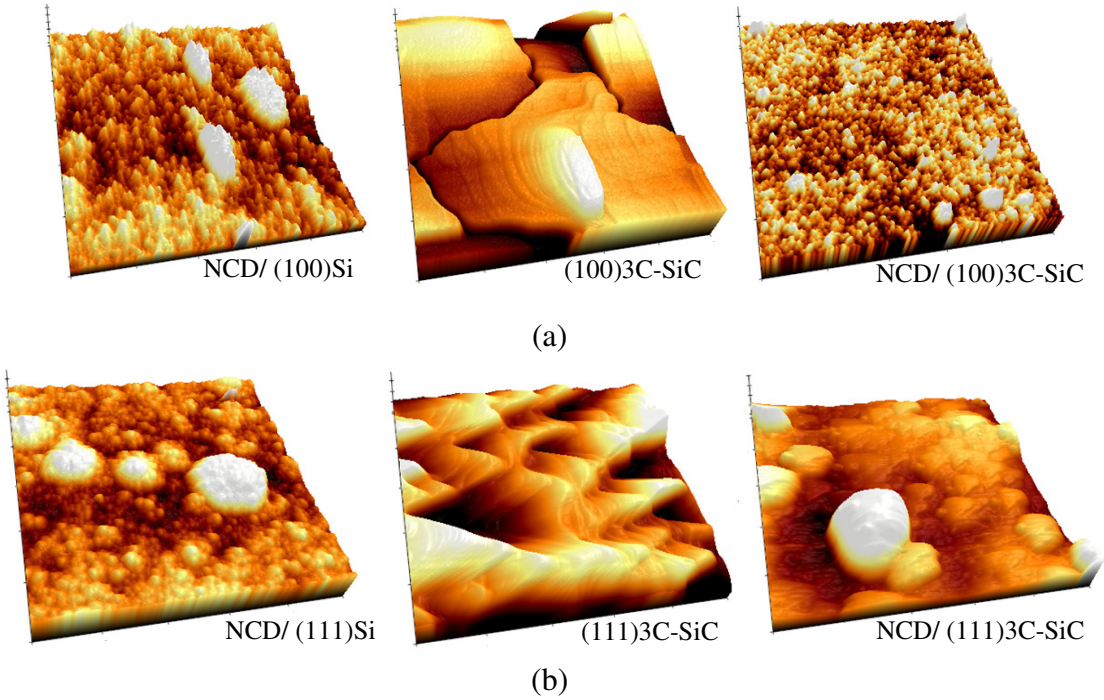

Figure 2.12: Three dimensional AFM micrographs of NCD growth on various substrates. The micrographs in (a) depict from left to right NCD on (100)Si, 3C-SiC grown on (100)Si, and (c) NCD deposited on (100)3C-SiC. The micrographs in (b) depict from left to right (111)3C-SiC grown on (111)Si, 3C-SiC grown on (111)Si, and NCD grown on (111)3C-SiC. Note that the NCD on (100)Si has larger micro-grain defects that are not present within the NCD film deposited on (100)3C-SiC and that the rough mesa surface of as-grown 3C-SiC does not affect the structures of the NCD whereas the defective clusters are about the same on the (111) face. The triangular morphology of the (111)3C-SiC is apparent through the NCD deposited on that face.

Figure 2.12 depicts AFM analysis of the surface morphology of NCD deposited on (100) and (111)Si, the initial surface of the 3C-SiC grown on these two Si faces, and NCD deposited on the two 3C-SiC surfaces. NCD deposited on (100)Si shows a regular, cubic grains ranging from 100 – 500 nm in perimeter and 1,000 nm^2 – 10,000 nm^2 in area. However, the surface is marked with craters and the presence of many large, oval shaped defects which measure approximately 5 µm in perimeter and 1μm^2 in area. The

difference between these features on the NCD surface increased the roughness, r_q, to 17.0 nm RMS. The initial (100)3C-SiC, which was 3.45 µm thick measured by FTIR, shows the characteristic mesa growth pattern, atomic step terraces, and APB crevices. The initial surface has an r_q, of 7.25 nm RMS. The NCD grown on the (100)SiC surface shows a relatively even, flat surface with many small cubic grains 75 - 300 nm in perimeter and 500 nm^2 – 7,500 nm^2 in area. This surface does not show the large grain inclusions displayed by the NCD on (100)SiC but instead has round inclusions with approximately 2 µm perimeters and 75,000 nm^2 area. The relatively flat surface and similar grain have surface roughness of 7.30 nm RMS, which is a little over half the roughness of the NCD on (100)Si.

NCD grown on (111)Si displays a much different surface morphology than that seen with NCD on (100)Si. The grains on this surface possess rounded surfaces and show a wider range of size differences with measurements ranging from 500 nm – 2 µm in perimeter and 15,000 nm^2 – 100,000 nm^2 in area. The surface is littered with large circular clump-like inclusions 2- 8 µm in perimeter and areas up to 1.8 μm^2. The large defects and differences in grain size increase the r_q to 37.9 nm RMS. 3.35 µm of 3C-SiC grown on (111)Si shows a regular atomic step, triangular terraced surface and possesses an r_q of 10.6 nm RMS. NCD deposited on this surface is similar to the NCD deposited on (111)Si in that there are irregularly sized grains and many large circular defects. The difference is the grains on this surface are triangular and much larger than the NCD grains on (111)Si with an average perimeter of 1.5 – 3 µm and area of 150,000 nm^2 – 500,000 nm^2. The larger, circular defects are measured approximately possessing 5µm

perimeters and 1.5 μm^2 areas. The roughness of this surface is almost equivalent to NCD deposited on (111)Si which was 27.7 nm RMS.

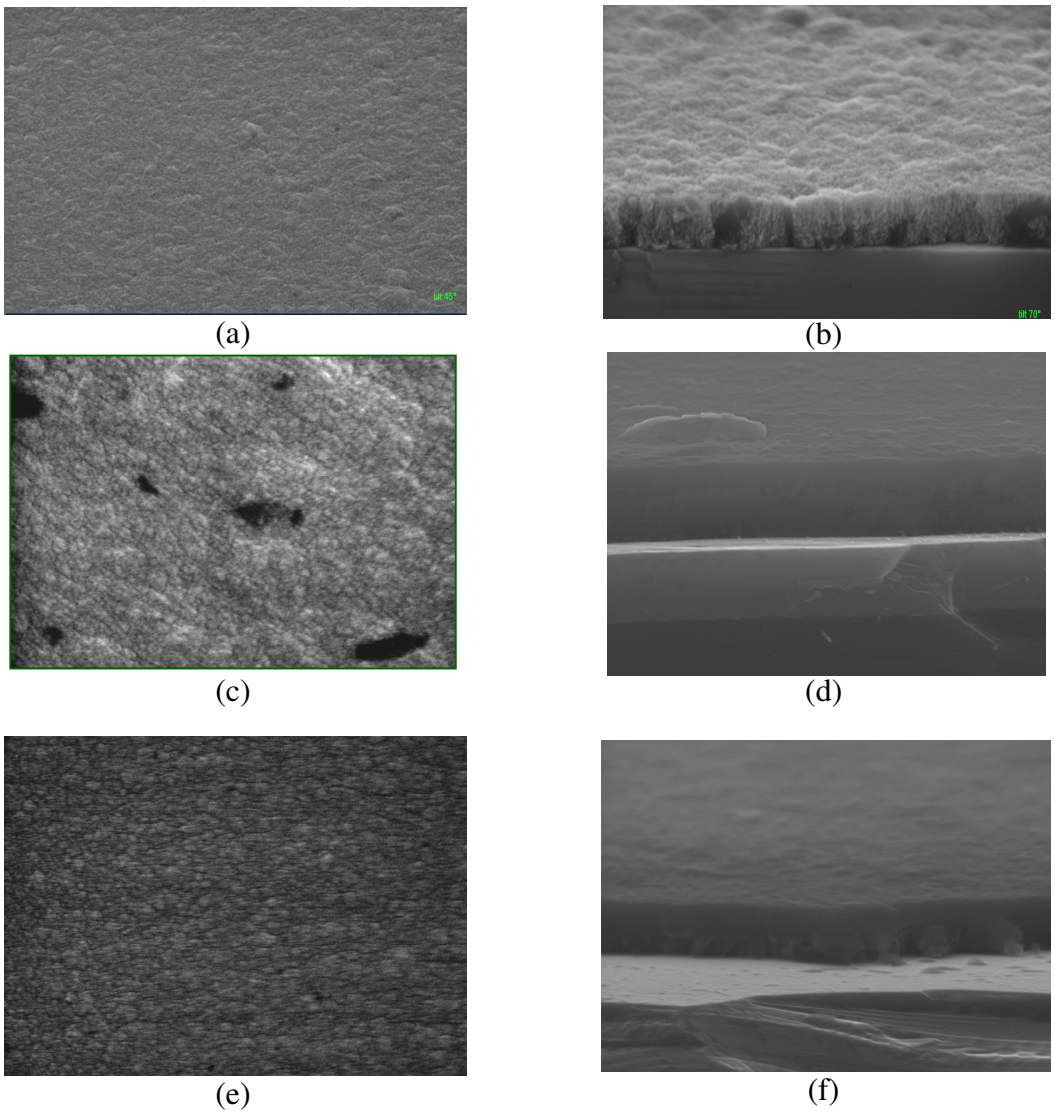

Figure 2.13: SEM plan view (column 1) and cross-section (column 2) micrographs of the NCD deposited on the various tested substrates. NCD deposited on (100)3C-SiC is displayed in (a-b), on (111)3C-SiC in (c-d), and on (100)Si in (e-f). 3C-SiC that indicates the NCD and 3C-SiC interface is not completely integrated. SEM data (a) and (b) courtesy of M. Italia, IMM-CNR, Catania (IT).

Figure 2.13 shows further examination of the morphology of the samples through the use of SEM. (100)3C-SiC, shown in Figure 2.13(a-b), shows a relatively smooth surface which has small grain and very small large grain defects. The cross section shows that the film is highly granular, possessing many random grain boundaries. Figure 2.13(c-d) show the morphology of the NCD film deposited on (111)3C-SiC. This film is very rough and has many large, dark defects, indicating that these defects are more conductive than the film around them. The cross sectional view indicates that these mound-like defects extend far above the nominal NCD surface. The cross section also shows that the NCD film is not as granular as the NCD deposited on (100)3C-SiC, and tends to align in sheets 45° normal to the surface. Figure 2.13(e-f) show NCD deposited on (100)Si. This film shows a surface which possesses small grains with intermixed larger grains, much like was seen with the AFM. A difference in this film when compared to the other NCD films is film is very defective close to the NCD/ Si interface, but the defects decrease with increasing film thickness. NCD does not appear to have good adhesion with any of the films, as indicated within the cross section views. The film is broken back and uneven as compared to the Si and 3C-SiC which are even with the cleaved surface.

The crystal quality of the NCD deposited on these various substrates was examined next. Figure 2.14 shows Raman and NEXAFS measurements of the NCD film deposited on (100)3C-SiC. Raman peaks indicated at 1333 cm^{-1} and 1380 cm^{-1} in the D band as well as 1580 cm^{-1} in the G band are indications of sp3 bonds of diamond. The band at 1172 cm^{-1} is an indicator of the presence of NCD. The Raman measurement in

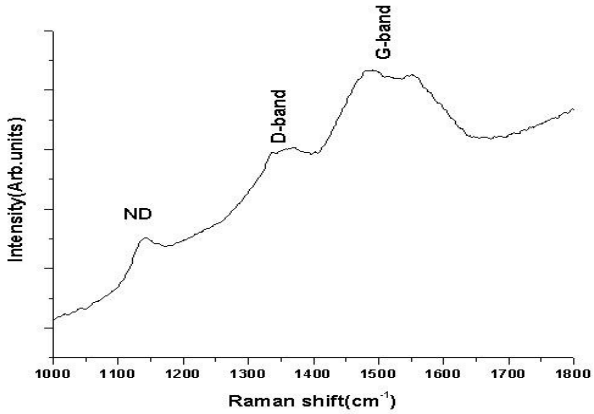

(a)

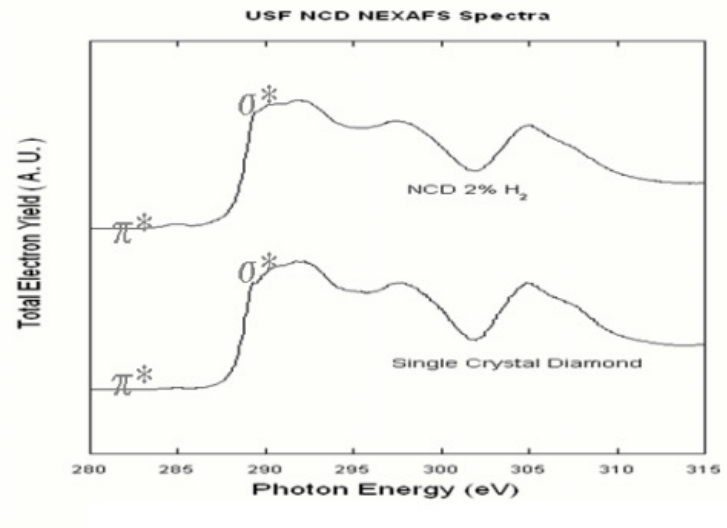

(b)

Figure 2.14: Raman (a) and NEXAFS (b) absorption fine structure scans of NCD deposited on (100)3C-SiC. Raman courtesy of H. Gomez, USF, and NEXAFS courtesy of Dr. J. Sathyaharish SRI International.

Figure 2.14(a) indicates that the NCD film possesses 95 – 98% sp^3 bonded carbon atoms. The NEXAFS spectrum obtained for the NCD deposited on 3C-SiC indicates a similar type of graph as single crystal diamond, suggesting NCD film is phase diamond.

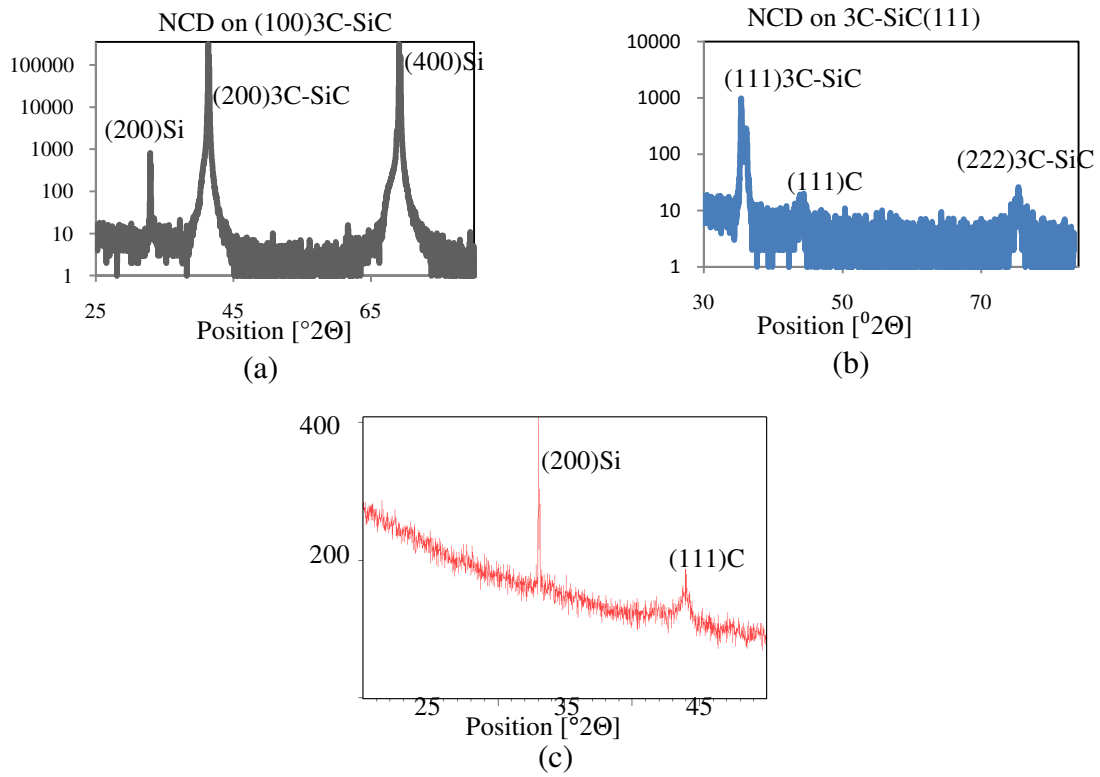

Figure 2.15: XRD θ-2θ diffraction surveys for the NCD films deposited on (a) (100)3C-SiC, (b) (111)3C-SiC and (c) (100)Si substrates. XRD measurements courtesy of H. Gomez of USF.

XRD θ-2θ diffraction surveys were utilized to collaborate the presence of diamond on the surface of the different substrates and to quantify the crystal orientation of the NCD film. Figure 2.15(a) shows the θ-2θ diffraction surveys measured at CuKα emission from 25° - 80° for the NCD grown on (100)3C-SiC. The (100)3C-SiC and (100)Si substrate beneath the NCD film are detected as indicated by the peaks at 41.5° for the (200)3C-SiC, and 32.95° and 69.1° for (200)Si and (400)Si respectively. The peaks normally associated with (100) diamond, 51.17° for (200)C, are not present within this measurement, and any (111) diamond, 43.9°, would be lost within the broad 3C-SiC peak. Figure 2.15(b) shows the θ-2θ diffraction surveys measured at CuKα emission

from 30° - 85° for the NCD grown on (111)3C-SiC. Two major peaks which are associated with (111)3C-SiC are located at 35.7° and 75.7°. A (111) diamond peak is present in this measurement, and its low, broad peak suggests the polycrystalline alignment of the nanoparticle diamonds on the surface. The (111) Si peaks located at 58.85° were not present with this measurement and more investigation into the cause of this is needed. Figure 2.15(c) shows the θ-2θ diffraction surveys measured at CuKα emission from 20° - 50° for the NCD grown on (100) Si. A large (100)Si peak is present at 32.95°, and the (111) diamond peak at 43.9° is much more sharp in comparison to the peak of the NCD on (111)3C-SiC. A repeat of this measurement, increasing the sweep of Θ to at least 80° should be done to examine if (200) diamond is present in the NCD.

Our initial probing into the deposition of NCD on 3C-SiC has shown us that the resulting material is different than that deposited on Si using the same process. The grains and defective clusters are smaller with the NCD deposited on 3C-SiC than that of the NCD deposited on Si. The difficulties of the (200)3C-SiC peak overlapping the (111)C diamond peak requires the use of another measurement for crystal quality. Selected area electron diffraction (SAED) TEM should be performed on the samples to quantify the crystal orientation. Dark field and bright field imaging techniques can be used to obtain information on the grain quality as well. We are currently examining the films with the TEM, but have not generated enough quality evidence as of yet to present in this work.

2.5 Summary of Chapter

3C-SiC, unlike other forms of SiC, is a material with little material development. Our group at USF has been recognized as a world leader with the growth of 3C-SiC and has developed methods to decrease defects inherent with its epitaxial growth. We have developed a low pressure method which decreased the interfacial defects present in 3C-SiC, and hydrogen etching treatments which reduce defects and create atomically flat terraces on the surface of the semiconductor. Our improvements in the crystal quality of 3C-SiC will improve the quality of a MEMS device that would be required to interact with the CNS. Another requirement of the implantable neural prosthetic would require a high quality, biocompatible insulating material to enable the generation of field effect devices. NCD may be the biocompatible material that would achieve this purpose, and our investigation into the integration of this material with Si and 3C-SiC revealed defects that would decrease electrical operation. Continued study of the integration of these materials is required for the generation of a final neural implantation device and shall be discussed in chapter 5. The focus of the next chapter is to evaluate the biocompatibility of monocrystalline 3C-SiC and NCD using *in vitro* methodology, which is clearly integral to the development of an eventual *in vivo* neuronal implant device.

Chapter 3: Neural Biocompatibility of SiC and NCD

3.1 Chapter Introduction

The central nervous system, or CNS, is one of the most complicated systems in the body and consists of a dense network of neurons and glial cells. Due to the very nature of this system it is very difficult to interact externally with the CNS, either through the use of drugs or externally interfaced biomedical devices. The blood-brain barrier and the actions of glial cells, more specifically the astrocytes, effectively prevent antibodies and many drugs treatments from reaching their intended targets within the CNS [26]. Fortunately implantation of a biomedical device into the CNS makes direct interaction with the cells possible and effectively bypasses the blood-brain barrier, but the construction materials can activate microglia and astrocytes which react with the foreign material to induce gliosis, which is the glial scar response [30, 31, 116, 117]. Devices which can interact electrically with the cells were discussed in (§ 1.4), but these devices could also be utilized as a platform for drug delivery to specific CNS areas or to transport neural factors or even other cells to the CNS to repair the system damaged by glial scarring [116, 117]. These devices can offer solutions to many problems that are currently untreatable by conventional medicine, but their implantation has led to the initiation of glial scarring instead of providing the therapies that they were designed for.

Studies have shown that damage caused by the insertion of devices into the brain can be minimized by a carefully designed device; the smaller in dimension and sharper the device is, the lower the probability of initiating glial scarring immediately after insertion [118]. The damage from the insertion itself is not the source of glial cell activation, but is caused instead by another factor which leads to long term inflammatory response [118]. The greatest factor that prevents the use of proposed CNS interaction devices arises from the interaction between the device materials and the multitude of cells, fluids, and chemicals within the CNS, which is simply an effect commonly known as material biocompatibility [6, 31]. Of the many materials used to date and incorporated within the CNS system, few have shown the level of biocompatibility necessary for incorporation or for proper long term successful operation of the device. In (§ 1.5-1.6), two materials were introduced as possible candidates for the construction of a neural implantation device based on the fact that amorphous or polycrystalline forms of these materials had shown good biocompatibility along with chemical and mechanical resilience. Within this section, we will cover the research we have done to investigate the biocompatibility of 3C-SiC and NCD with immortalized neural and CNS cell lines. (§ 3.2) will explain how the living cell can interact at a molecular level with inanimate materials, methods to test for biocompatibility of the materials, and the experiments that were used to determine the degree of biocompatibility. (§ 3.3) details the results obtained from these experiments, and (§ 3.4) will discuss the results and offer some possible explanations for these results.

3.2 Foreign Material and Living Cell Surface Interaction

The cell to substrate interaction is a very important consideration for determining a material's performance for biomedical implant applications. Neurons and many glial cells, like many cells in the mammalian body, must attach to an external surface or they will experience programmed cell death or apoptosis. Generally a cell will attach to a substrate surface through physiochemical interaction between the cells cytoskeleton, cell membrane, extracellular proteins, substrate ions, hydration compounds, and molecules [119, 120]. Macroscopically cells on biocompatible surfaces will interact with the substrate by increasing their attached area and will have greater viability than cells interacting with unsuitable or toxic surfaces [119]. Thus, cell morphology and viability can be used as measures of surface biocompatibility.

Another measurement of surface biocompatibility is to evaluate the extension of lamellipodia or filopodia from motile cells onto a substrate surface [121]. Neurons and many glial cells experience different levels of motility during their lifetimes [122, 123]. During the developmental stage of the brain the cells are fully motile and travel down radial glial cells to predetermined locations where their somata firmly attach to the extracellular matrix [122, 123]. The attached somata of the neurons extend microtubule-filled growth cones that are the backbone for the dynamic formation of dendritic spines and axons [121]. The growth cone is guided by peripheral extensions of actin filled cytoplasmic lamellipodia and spike-like filopodia [121]. Astrocytes and other glial cells also extrude lamellipodia or filopodia which actively seek to interact with neurons, endothelial cells, or other glial cells [122]. The lamellipodia or filopodia are attracted

and repulsed by chemical and contact-mediated cues which influence how the structures connect to the outside world [121, 122]. If an external surface is repulsive to the cells, the lamellipodia or filopodia will not couple with the surface and actin filaments flow back into the central core, but if the substance is attractive, the lamellipodia or filopodia couple strongly with the surface and new actin fibers flow to the leading edge of the cell extension [121]. Using the actions of lamellipodia or filopodia structures, a surface can be considered permissive to the cells if it produces an attraction of the lamellipodia and filopodia, and non-permissive if it repels them [121].

3.2.1 SiC Biocompatibility

One method for increasing the chronic implantation time for the implantable neural device is to increase the level of biocompatibility of the device. One method of improving the biocompatibility of a device is to add surface coatings [31, 116, 117]. Many coatings have been used such as biocompatible material, inorganic or organic polymers, or chemical complexes and enzymes [31, 116, 117]. Although these coatings can make the device much more biocompatible, many major difficulties arise from this approach. Devices that utilize electrical interconnections with cells and have coatings added to their surfaces also have additional complex electrical impedance factors which decrease the electrical operational capabilities of the device [3, 4, 13, 14, 40]. Many of the proposed coatings are also temporary, and when the base material is exposed to the body these coatings fail. What is clearly preferred is a material that is biocompatible without the use of coatings, particularly for devices which must sense the biological

system electrically. 3C-SiC, which our group has actively tested *in vitro* with skin and bone cell lines to evaluate its general biocompatibility with the goal of demonstrating if the material is a suitable candidate for use in electrically active biological sensors, may be just that material [124].

The biocompatibility of 3C-SiC was determined by using the methods for testing of biomedical devices which are outlined in ISO 10993. Initial testing techniques outlined in this standard follow *in vitro* testing of bulk and surface materials involved in the creation of the device with cultures of cells. Specifically, for Coletti *et al.* the growth of selected cell lines on specific tested materials was monitored using fluorescence microscopy. Optical microscopy allows for qualitative determination of cell morphology and cell attachment over populations of cells. Cell viability on these surfaces was determined quantitatively using yellow MTT, (3-(4,5-Dimethylthiazol-2-yl)-2,5-diphenyltetrazolium bromide), assays [125]. Coletti *et al.* compared the three major polytypes of SiC, namely 3C-SiC, 4H-SiC, and 6H-SiC, with Si and used polystyrene, PSt, as a control. The immortalized mammalian cells cultured on the semiconducting substrates were: B16-F10 mouse melanoma cells (ATCC CRL6475); BJ human fibroblasts (ATCC CRL2522); and human keratinocytes cells (HaCaT). All cells were cultured initially into 75 mm^2 flasks and incubated at 37 ºC in an air atmosphere containing 5% CO_2 and 95% relative humidity. For each test, cells were collected from the flasks through trypsinization, and enumerated using a Hemocytometer to determine the number of cells per ml.

The results obtained clearly show that SiC is, in all of its tested phases, a high-quality surface for cell culture with significantly better performance than Si and nearly as good a performance as the PSt control. No statistically significant differences were found among the cell proliferation values on the different SiC polytypes [124]. An extremely satisfying proliferation was observed for BJ fibroblast cells on SiC, which were on average the same obtained for the culture-well readings, and a slight bioactivity of the SiC substrate could even be hypothesized from the results [124]. A smaller difference in B16 cell proliferation was observed between Si and SiC substrates, but can be easily justified by the nature of the cell line [124]. B16 melanoma cells are, in fact, extremely aggressive cancer cells capable of indifferently adhering to substrates of diverse biocompatibility: therefore a reduced selectivity was expected. A secondary set of MTT assays was performed on only the Si, 3C-SiC, and 4H-SiC samples using the HaCaT cell line which was evaluated on the first and eighth day of HaCaT cell culture [126]. Although proliferation values for each substrate are comparable on the first day after seeding, cell proliferation was greater on both polytypes of SiC and significantly decreased on Si surfaces after eight days of culture [126]. The lowered viability of SiC during the short term suggests a difficulty of the material to absorb proteins, but the study by Coletti *et al*. was not designed to verify this result [126].

Cell proliferation on the tested substrates was quantified using MTT assays. For this proliferation assay, cells were cultured on the testing substrates and yellow MTT was added after a predetermined time [125]. MTT is only metabolized by living mitochondria to produce purple formazan, insoluble in water but soluble in dimethyl sulfoxide, DMSO,

and subsequently quantified the assay by using a spectrophotometer measuring the index of refraction with a wavelength in the range of 500 to 600 nm [125]. Testing cellular morphology and its permissiveness to a particular substrate has many well established methods, one of which is fluorescence microscopy. Another very selective measurement technique for cell attachment is total internal reflection fluorescence (TIRF), which can image the cell interface within 200 nm from the surface; however this technique nominally requires a substrate that allows evanescent and internal reflection wave generation, such as silica, and substrates like SiC, Si, and NCD are either opaque or translucent and will not easily allow for the internal reflection [127]. Confocal microscopy, a technique which is gaining prevalence in biological examination, generates point illumination of a sample through a combination of filters, beam splitters, and gratings to eliminate out-of-focus light thereby detecting light within a focal plane, and raster scanning can then be used to generate detailed two and three dimensional images [128]. Unfortunately, confocal microscopes are very expensive, and many of the models used for biology are designed with inverted microscopes and are not suitable for opaque substrates. AFM uses a laser reflected off a cantilever to gather quantitative morphological surface information. This technique can image living cells on opaque surfaces, and costs much less than a confocal microscope. Although it cannot provide information about the surface interaction underneath a cell, or information from inside the cell, it can provide detailed information on cell spread and morphology on almost any surface. The methodology for AFM measurements will be covered in detail in (§ 3.2.4).

3.2.2 Sample and Cleaning Protocol

In this study we report on research to evaluate the biocompatibility of SiC, NCD, and Si with neuron cell lines and utilize polystyrene (PSt) and amorphous glass from glass microscope slides as control materials. Unlike Coletti *et al.*, the growth of 3C-SiC had progressed onto another crystalline face, so we tested (100)Si as well as (111)Si. Using the methods covered in (§2.2), (100)3C-SiC and (111)3C-SiC was homoepitaxially grown on (100)Si and (111)Si wafers in the MF2 CVD reactor at the University of South Florida. 4H-SiC and 6H-SiC samples were obtained from wafers purchased from Cree Inc. NCD was deposited on (100)Si wafers using a Cyrannus Iplas MPECVD NCD Reactor utilizing growth methods covered in (§2.4). Amorphous glass cover slips and sterile Corning Cellbind® treated polystyrene Petri dishes (Fisher 07-202-514) were utilized for the control materials.

The semiconductor samples were further subdivided by bulk doping levels. The Si samples were intentionally negatively doped with phosphorus, while the 3C-SiC was unintentionally negatively doped due to a small presence of nitrogen during growth. The NCD, which was deposited at a much lower pressure than the 3C-SiC, would be intrinsic with hydrogen surface termination. There was n-type, p-type, and intrinsic samples available of both the hexagonal forms of SiC. All samples used in the study were diced into dimensions of 8 mm x 10 mm to facilitate insertion into 12-well and 24-well tissue culture treated polystyrene plates (USA Scientific # 5666-5180 and 5666-2160). After dicing, the semiconductor and glass samples were ultrasonically cleaned in solvent baths of acetone, methanol, and isopropanol for 5 minutes each to remove dicing particulates

and disinfect the surfaces. The semiconductor samples were then cleaned using the standard RCA cleaning process. The cleaning steps of this procedure were as follows: a 1:1:6 mixture of NH_4OH:H_2O_2:H_2O heated to 65°C for 10 minutes; followed by a 50:1 H_2O:HF for 30 seconds and by a 1:1:6 mixture of HCl:H_2O_2:H_2O heated to 65°C for 10 minutes [124]. All H_2O was deionized (DI) with $\rho > 16$ MΩ·cm. The diced PSt samples were used only for the AFM analysis and were diced within a class II A/B3 biological safety cabinet followed with brief immersion in 70% (v/v) ethanol to remove any particulates.

Before cell plating, the semiconductor samples were cleaned using a piranha solution (2:1 H_2SO_4:H_2O_2) with 10 minutes of immersion and then rinsed three times in DI H_2O. This was followed by a 5 minute immersion in a solution of HCl (2:1 HCl:H_2O) to remove any remnant sulfur, a known cytotoxic element to neurons, from the surface. After rinsing the sample once again in DI H_2O, the substrates were dipped in 50:1 H_2O:HF for 2 minutes to remove any native oxides and rinsed three times in DI H_2O. The samples were dried using pressurized N_2 and placed into ethanol to prevent both bacterial growth and surface oxidation. The glass substrates were autoclaved in 121 °C water steam for 30 minutes prior to cell deposition. Due to the high cost of CVD crystal growth and time required to generate these films, the same SiC and NCD samples were reused for multiple experiments. The results of the study by [124] showed that 3C-SiC becomes silicon rich from loss of carbon due to multiple cleanings in piranha solution, so to maintain surfaces representative with 'as grown' characteristics, which contains both

silicon and carbon on the surface, we replaced the 3C-SiC and NCD with fresh samples after 3 cleanings [124].

3.2.3 Cell Culture and MTT Assay Protocol

Two neural cell lines obtained from American Type Culture Collection, ATCC, in Manassas, MD were used for this study; H4 human neuroglioma (ATCC #HTB-148), and PC12 Rat pheochromocytoma (ATCC #CRL-1721). The H4 cell line is neuron derived from a CNS glial tumor in the frontal cortex, and the PC12 is a peripheral neural modeling cell derived from the adrenal gland [129]. The H4 cell line was cultured in advanced Dulbecco's Modified Eagle's Medium (DMEM) (Invitrogen #12491-015) without L-glutamine supplemented with 10% fetal bovine serum, FBS (Invitrogen #26140-087), 2.2 mM L-glutamine GlutaMAX-1 supplement (Invitrogen #35050-061), and 1% penicillin-streptomycin (Sigma #P4458-100ML). The PC12 line was grown in Kaighn's F-12K Media (Invitrogen # 21127-030) supplemented with 2.5 % FBS, 15% horse serum (Invitrogen #16050-122), and 1% penicillin-streptomycin. The cells were cultured in Corning® Cellbind® 75 mm^2 flasks (Fisher # 07-202-515) to approximately 90% confluence, collected through trypsinization, and enumerated using a Hemocytometer to determine the number of cells per ml.

Cleaned substrate samples were seeded with cells by first drying the ethanol on the samples using a hand held bulb. Each sample was placed into one well of a 12-well plate. Initial experimentation had determined that $1x10^5$ H4 cells and $5x10^5$ PC12 cells would be seeded in each well, followed with the addition of 3 ml of the appropriate

media, to achieve the level of cell coverage necessary for the assay. After 96 hours, the MTT assay was performed in accordance with the procedures outlined in [124, 125], with each assay repeated in triplicate for three individual samples from each tested substrate along with the PSt control. The results from these tests were normalized with respect to the PSt control readings and expressed as the sampling distribution of the mean ($\bar{x}$) ± standard error of the mean (σ_M) as reported in the next section. Amorphous glass was not tested in the MTT analysis due to the fact that it already has been determined to have a low biocompatibility level [10].

3.2.4 AFM Methodology for Cell Morphology and Substrate Permissiveness

AFM measurement, using a Park Systems XE-100 AFM, for each substrate and cell line was conducted to provide quantitative analysis of cell morphology and permissiveness. Cells were plated on each of the substrates using the plating procedures described in (§3.2.3) and allowed to incubate for at least 48 hours. The AFM of living cells was performed in phosphate buffered solution, PBS, provided the basis for a quantification of cell height, total surface area of the cell, angle of attachment, and the full extension of the lamellipodia/filopodia. After the living cell scans, the cells were then fixed using 4% paraformaldehyde for 20 minutes to immobilize the lamellipodia and filopodia structures so we could measure an overall progression or regression over the surface of the substrate. As each cell studied in the AFM had slightly different physical dimensions, the measurements were therefore expressed as ratios or percentages to provide a basis for comparison. The ratio of cell height to cell area and the angle of

attachment, which is the slope of the membrane to the substrate surface, were used to evaluate the attachment level of the cell to the substrate. Analysis of the AFM images was performed with Park Systems XEI image analysis software. Figure 3.1(a) shows an example of line scan analysis which was used to determine maximal cell height and angle of attachment. Figure 3.1(a) also shows that area analysis is possible by selecting the image pixel height and was used to determine the surface area of the cell. Although the topographical measurement provided by AFM will not image the internal actin meshwork associated with lamellipodia and filopodia, these structures can still be identified and measured. It is the consensus view that filopodia are the cell vanguard for probing the local environment which is then followed by the generation of lamellipodia [130]. By examining the outer extremities of the cell, we identified the spike-like filopodia structures, as shown in Figure 3.1(b), and used them to identify the lamellipodia structure through line scan analysis since the lamellipodia are known to be a thin membrane layer 100 – 200 nm thick and parallel to the substrate surface [130]. Once identified, these features were measured using XEI area analysis on both the living cell and the fixed cell observations, normalized as a percentage of total cell attachment area, and the subsequent loss (or gain) percentage in area was used to quantitatively express the cell permissiveness to the substrate. Due to the fact that many hours were required for the analysis and measurement of the cells, three cells were randomly selected from each surface studied. The results were then analyzed and mean results used to make the final comparison between surfaces.

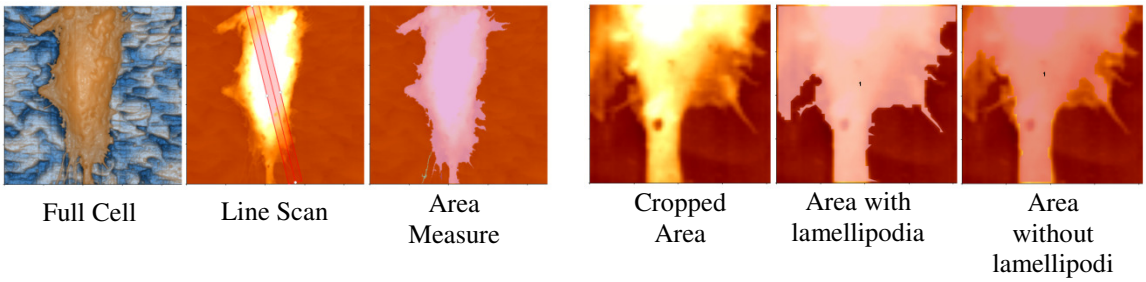

Figure 3.1: Depiction of various AFM measurements utilized for the determination of cell permissiveness on the substrates tested in this study. (a) From left to right: a 45 x 45 µm AFM micrograph of a cell displayed in enhanced color, a line evaluation of the same cell to determine cell height and the angle of attachment to the substrate, and a total surface area measurement. (b) From left to right: a cropped section of the original AFM micrograph with (a) 10 x 10 µm size depicting filopodia/ lamellipodia, an area measurement of the filopodia/ lamellipodia including the cell body, and an area measurement of the cell body only eliminating the filopodia/ lamellipodia to determine the percentage of total cell surface area that is composed of these features.

3.3 Experimental Results

The MTT analysis results for both the H4 and PC12 cell lines are displayed in Figure 3.2. The H4 cell line shows a viability level of approximately 80% ± 5% as compared to the PSt control for all samples excluding (111)Si which performed at 108% ± 9%, and 6H-SiC p-type 47.4% ± 5%. This result is confirmed through the use of Tukey's pairs of means test on a sample population, which shows that all surfaces are statistically similar, except (111)Si which is similar to PSt, and 6H-SiC p-type which is different from all surfaces. The PC12 line displays results with the (100)Si substrate that were very similar to Coletti *et al.* [124], however the (111)Si has excellent viability which is equal to that of the 3C-SiC samples. Tukey's pairs of means test indicates that the 3C-SiC samples and (111)Si possess a statistically similar level of viability to the PSt control. This large discrepancy between the Si substrates is very noteworthy, and will be discussed in more detail within (§3.2.4).

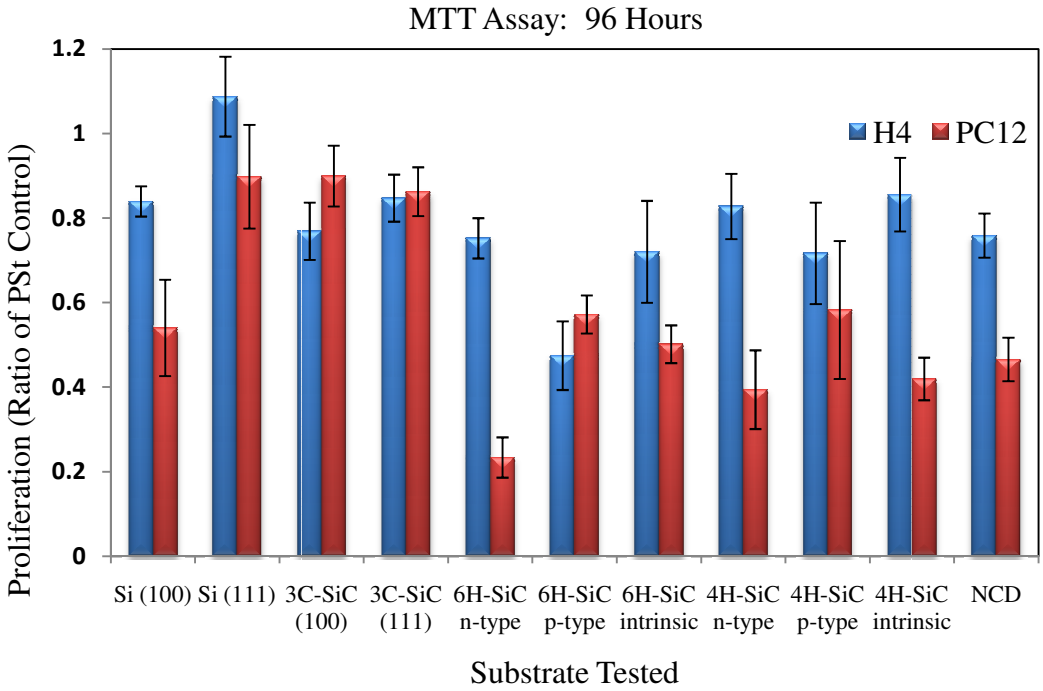

Figure 3.2: H4 and PC12 cell proliferation on Si and SiC substrates measured via MTT on the fourth day of culture normalized to the PSt control and expressed as $\bar{x} \pm \sigma_m$. Unlike the previous MTT experiments with fibroblasts and skin cells, Si maintains high levels of viability with the H4 cell line and a low level with the PC12 cell line. There is a similar difference between (100) and (111) face materials. But surprisingly, 4H-SiC and 6H-SiC do not show the same level of viability as 3C-SiC, and definite patterns emerge due to the doping of the semiconductors.

The hexagonal polytypes of SiC along with the NCD samples show a very poor viability with the PC12 cell line compared to less than 60% of the PSt. The lowest viability for these materials is for n-type bulk doping, with 6H-SiC sample lower than the 4H-SiC sample. Viability increases slightly for intrinsic material and shows a greater increase with p-type material. As we did not have the ability to grow p-type 3C-SiC, and did not possess p-type Si at the time of this study, we could not determine if the viability patterns due to semiconductor material doping continued, but as the trend was followed

by both hexagonal substrates, it is likely that this trend would be consistent for p-type Si and 3C-SiC as well.

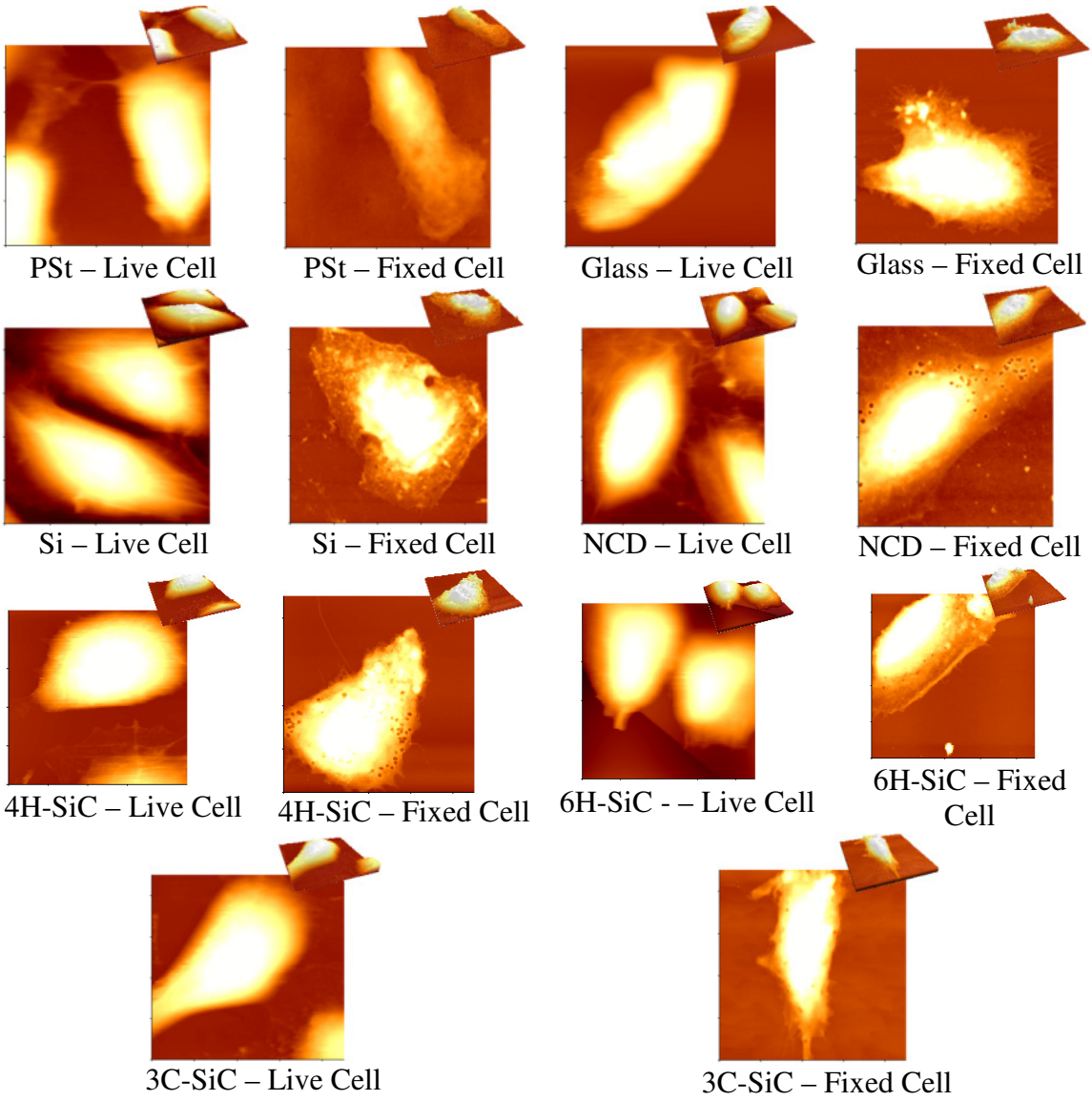

Figure 3.3: Selected 45 x 45 µm AFM micrographs of H4 cells seeded on the substrates tested in this study. Each micrograph possesses a pseudo three dimentional insert in the upper right hand corner to give some perspective on cell morphology in relation to the surface of the substrate. Underneath each micrgraph is the type of substrate and the condition of the cell. AFM data taken in contact mode.

The morphology and lamellipodia attachment quality of the H4 cells were evaluated with AFM analysis. Figure 3.3 displays two selected AFM micrograph scans of the H4 cell line incubated on each of the tested substrates, with one scan showing a living cell and the other a fixed cell. The H4 cells on PSt show a low level of attachment to the surface, possessing an average height to surface area ratio of 5.40×10^{-3} and a steep angle of attachment of 30.6°. The micrograph shows that the H4 cells on PSt have microtubule extensions which are connecting with neighboring cells, and the average lamellipodia extensions from three micrographs consist of about 28.9% of the total cell area while the cell was measured alive. The fixed cells show an average decrease in the lamellipodia area, constituting only 15.4% of the cell area, which is a reduction of 13.5% as compared to the living cell measurements. The H4 cells on glass react in a similar manner when compared to the cells on PSt. The average height to surface area ratio is 7.04×10^{-3} and the angle of attachment is 23.8°, indicating that the cells are retracting from the surface. Although there are large expanses of lamellipodia present with many of the cells on the glass substrate, they show very little attachment to the surface, and therefore little permissiveness, constituting an average of 45.5% of the cell area while measured alive and only an average of 8.43% of the cell after fixation which is a 27% reduction. The H4 cells on the surface of Si and on NCD possess similar levels of cell attachment to the surface, but they show differences in the lamellipodia permissiveness. The H4 cells flatten and expand over a larger surface area on these substrates, with ratios of 3.11×10^{-3}, and 3.82×10^{-3} for Si and NCD, respectively. The angles of attachment, measured at 15.2° and 13.8° respectively, also indicate that the cell cytoskeletons attach to the surface at

many points causing the cell to spread and flatten over the surface. The H4 cell on Si has small microtubule extensions and shows the lamellipodia extending from multiple parts of the cell. These extensions account for an average of 36.4% of the cell area when measured alive and 26.4% after fixation. NCD shows a slightly better lamellipodia extension, possessing an attachment level with 30.5% of the cell area before fixation and 22.4% cell area after fixation, and display some very large microtubule extensions which suggest a good permissiveness to this surface. Overall, the lamellipodia reduction level for Si and NCD collected from the averaged readings was 10% and 8.1%, respectively.

The AFM scans for H4 cells on the surfaces of 3C-SiC, 4H-SiC, and 6H-SiC show very different morphologies, indicating that the biocompatibility of SiC cannot be treated as a single material as was previously suggested, but must be examined on the basis of the different polytypes [18-20]. The H4 cells on 3C-SiC flatten, expand and elongate over a large surface area showing an average height to area ratio of 4.58×10^{-3} μm^{-1} and an angle of attachment of 16.3°. For 3C-SiC large microtubule extensions on many of the cells were evident with multiple smaller extensions present. The lamellipodia, which measured 15.1% of the living cellular area, was the only sample group tested with the H4 cell line that had an average increase in area percentage with an average area measurement of 15.4% after the cell was fixed. This is indicative of a lightly permissive substrate and explains the presence of the multiple microtubule extensions, which are a normal function of the H4 cell, and suggests that the surface of 3C-SiC possesses innate molecular characteristics required by these cells. The H4 cells seeded on 4H-SiC are morphologically rounded or slightly triangular with an average

height to area ratio of 4.21×10^{-3} μm^{-1} and an angle of attachment of 17.3°. Microtubule extensions are either non-existent or of very short length from the soma, and the lamellipodia that measured 17.3% of the living cellular area reduced to 8.4% after the cell was fixed, showing a decrease of 8.9% in area. This indicates that the surface of 4H-SiC is not as permissive to these cells as was seen with the 3C-SiC polytype, and surface science investigation of the differences between the surface could shed light on the physical cues that the cells use for membrane attachment. The cells on 6H-SiC show slightly different characteristics than their 4H-SiC counterpart with a more elongated, ellipsoidal morphology and multiple small microtubule extensions. The cells are elevated from the substrate, possessing an average height to area ratio of 4.78×10^{-3} μm^{-1} and an angle of attachment of 19.9°, but the lamellipodia, which have smaller extensions, show an attachment measuring 5.8% of the living cellular area while it was 2.35% after the cell was fixed, which is a small decrease of 3.5% in area. The presence of the microtubules and the smaller lamellipodia retreat indicate that the surface of 6H-SiC possesses better surface characteristics than that of 4H-SiC, but the lack of large microtubule extensions and the better lamellipodia extensions show that 3C-SiC has better biocompatibility than 6H-SiC.

The PC12 cells have much different attachment characteristics than the H4 cells which may be most likely due to the fact that they are derived from adrenal cells and are a neuronal modeling line. This cell does not change into a peripheral neuron without the addition of neural growth factor (NGF), an expensive neural factor that would have made this study cost prohibitive. The Glass, Si, and NCD substrates show lower attachment

characteristics for this cell line. The cell height to area ratios are $6.85x10^{-3}$, $5.14x10^{-3}$, and $5.88x10^{-3}$ for the glass, Si, and NCD, and their angles of attachment are 31.2°, 31.5° and 29.9°, indicating the cells are trying to minimize their contact with these substrates. This analysis has further confirmation as each of these substrates show poor lamellipodia attachment. Glass had few or no microtubule extensions but extensive lamellipodia extensions covering 45.9% to cell area when measured alive and only 21.1% after fixation, a reduction of 24.8%. NCD was similar to glass in that it had few microtubule extensions and also had many extensions of lamellipodia covering 37.6% area for the living cell and 18.1% cell area for the fixed cell with a reduction of 19.5%. Although Si displayed good extensions of microtubules, it has a lamellipodia area reduction of 10.2 % as indicated for the 25.0% and 14.8% live cell and fixed cell lamellipodia measurements. The PC12 cells showed a good permissiveness with PSt having a height to surface area ratio of $2.65x10^{-3}$ and an angle of attachment of 22.6°. This material allows the cell to project multiple microtubule extensions and had a 3.3% increase in lamellipodia attachment area due to the living cell area lamellipodia percentages were 25.9% and 29.2% for the living and fixed cells, respectively.

As with the H4 cells, the PC12 cell line had very different attachment and morphology statistics over the three tested polytypes of SiC. The PC12 cells on 3C-SiC have a slightly lower height to surface area ratio of $4.80x10^{-3}$ μm^{-1} and a higher angle of attachment of 25.8° when compared to the PSt, but the morphologies of the cells were very similar. The cells show elongated ellipsoidal shape with two or more extensions of microtubules. The lamellipodia showed an attachment factor composing 29.3% of the

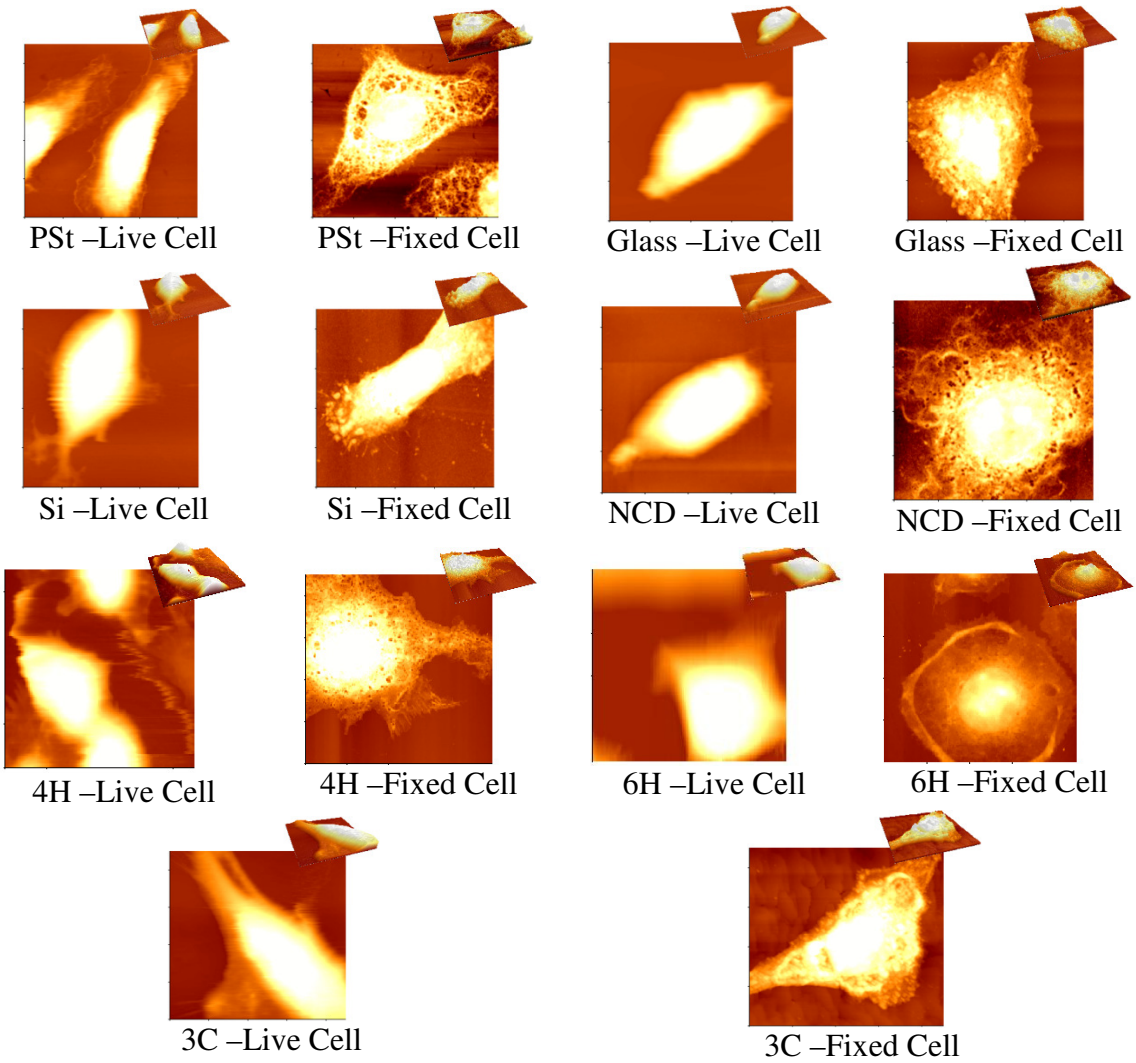

Figure 3.4: Selected 45 x 45 µm AFM micrographs of PC12 cells deposited on the substrates tested in this study. Each micrograph possesses a pseudo three dimentional insert in the upper right hand corner to give some perspective on cell morphology in relation to the surface of the substrate. Underneath each micrgraph is the type of substrate and the condition of the cell.

cell area for the living cell and 24.8% of the cell area for the fixed cells which amounts to a reduction of only 4.5%. Although this is not as good as the permissiveness shown with the H4 cell line, it is still relatively good and indicates that 3C-SiC is a good biomaterial with good permissiveness. The AFM measurements for 4H-SiC show that the PC12 cell line does not have good biocompatibility with this surface. The cells show a similar

attachment to this surface when compared to Si and 3C-SiC, possessing a height to area ratio of 4.71×10^{-3} μm^{-1} and an angle of attachment of 24.2°. The cells show an extremely rounded morphology and possess smaller microtubule extensions than 3C-SiC. The lamellipodia show similar reactions to this surface with Si, composing 19.2% of the cell area for the living cell and 8.8% of the cell area for the fixed cells. This reduction of 10.4% shows that the surface is not as permissive to this cell line as PSt and may not be suitable for long term implants. PC12 cells seeded on 6H-SiC show generally rounded cell morphologies with few microtubule extensions. The cells show an average height to area ratio of 7.40×10^{-3} μm^{-1} and an angle of attachment of 42.4° which indicates that they do attach well to the surface of this material. The PC12 cells show extensions of lamellipodia from many parts of the cell, but they are small in comparison with the entire cell body. The living cells show lamellipodia that composed about 4.24% of the cell area when measured alive, and this value reduced to 3.51% when the cell had been fixed. The values measured by the AFM and the MTT viability values show that 6H-SiC is not a suitable material for long term implants.

During the AFM measurement of both cell lines deposited on the various substrates, the Si surface was observed to suffer physical damage. Figure 3.5 displays AFM micrographs of the surfaces of three tested semiconductor substrates before cell deposition and their morphology after the cells had been deposited for a time of 48 hours. For each of the substrates seeded with cells, any cellular remnants and extracellular proteins were completely removed through the piranha cleaning method described in the material and methods section (§ 3.2.2). Figure 3.5(a) displays an AFM micrograph of the

Si surface after the initial RCA cleaning and subsequent piranha cleaning that occurs before the seeding of the cells. Commercial Si surfaces are chemical-mechanical polished (CMP) to an atomically flat surface, indicated in Figure 3.5(a), which shows a surface morphology marked by atomic-scale deep polishing scratches, and it possesses a surface root mean square roughness, r_q, within a 5 x 5 µm scan size of 0.137 nm RMS. The surface of the Si after cell seeding and removal shows many large elliptical depressions approximately 100 – 200 µm long which roughly correlate to the shapes of the H4 or PC12 cells as seen in Figure 3.3 and Figure 3.4 The surface within these depressions, which is displayed in Figure 3.5(b), shows numerous small, rounded surface pits with diameters of 500 to 700 nm and 30 to 70 nm deep. The 5 x 5 µm scan size r_q had increased to 18 nm RMS from 0.137 nm RMS.

3C-SiC and NCD are known to be chemically inert materials and they therefore do not display the changes seen on the surface of the Si substrates. The 'as-grown' surface of 3C-SiC, displayed in Figure 3.5(c), shows a rough, mosaic surface due to defects caused by the 20% lattice mismatch between 3C-SiC and Si, and it possesses a 5 x 5 µm scan size r_q of 2.46 nm RMS. The deposited NCD on Si surface displayed in Figure 3.5(e) has many approximately 50 – 100 nm diameter crystallites marked with larger 1 µm long boulder defects. The NCD 5 x 5 µm scan size r_q of 17.79 nm RMS was a direct result of the uneven nature of this surface. Figure 3.5(d) and Figure 3.5(f) show the 3C-SiC and NCD surfaces after cell removal, and the surface seemed to have little effect on the cells. The 5 x 5 µm scan size r_q of the 3C-SiC was 2.46 nm RMS and of the NCD was 13.42 nm RMS, showing little change in roughness, and was only different as

it is difficult to find the same area of measurement after the initial scan has been performed and the sample removed from the AFM stage..

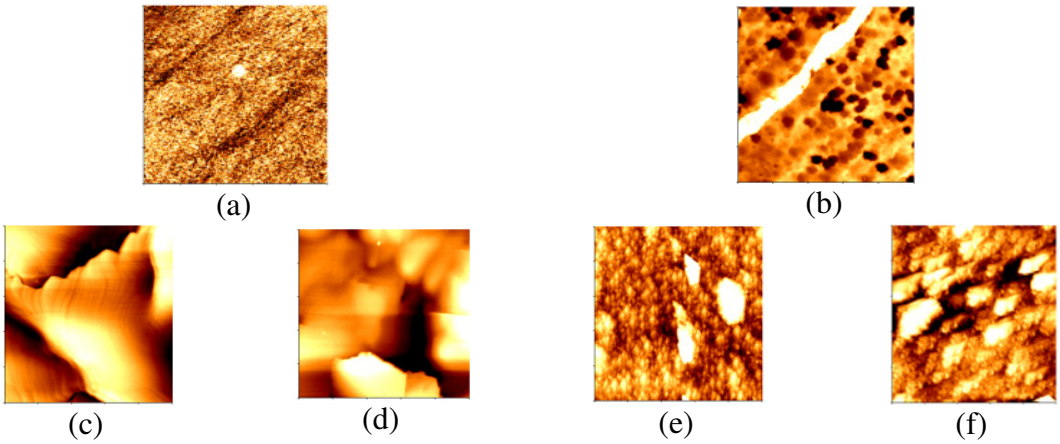

Figure 3.5: 5 x 5 µm AFM micrographs of the surfaces of the three tested semiconductors. The micrographs are presented with the first column displaying the morphology of the semiconductors before cell seeding and the second column represents the morphology of the semiconductors after cell removal and subsequent cleaning. (a) and (b) are the Si surfaces, (c) and (d) represent the 3C-SiC surfaces, and (e) and (f) are the NCD surfaces.

3.4 Discussion of Results

Table 3.1: Compiled values representing the cell interaction with the tested substrates as measured through AFM techniques. Each cell line is listed followed by a qualitative ranking of each substrate for negative and positive cell interaction.

Cell Interaction with Substrate	Negative Interaction → → Positive Interaction						
H4 Cell Line	Glass	PSt	Si	4H-SiC	NCD	6H-SiC	3C-SiC
Live Cell Height/ Area (10^{-3} µm^2)	7.04	5.40	3.11	4.21	3.82	4.78	4.58
Angle of Attachment (^{0})	23.8	30.6	15.2	17.3	13.8	19.9	16.3
% Area: Lamellipodia and Filopodia Reduction	27	13.5	10	8.9	8.1	3.5	-0.3*
PC12 Cell Line	Glass	NCD	6H-SiC	4H-SiC	Si	3C-SiC	PSt
Live Cell Height/ Area (10^{-3} µm^2)	6.85	5.88	7.40	4.71	5.14	4.80	2.65
Angle of Attachment (^{0})	31.2	29.9	42.4	24.2	31.5	25.8	22.6
% Area: Lamellipodia and Filopodia Reduction	24.8	19.5	12.7	10.4	10.2	4.5	-3.3*
* Note: Negative numbers indicate an increase in lamellipodia and filopodia area.							

This study focused on gaining insight into the biocompatibility of bare, untreated substrates with neuronal cell lines, and primarily used two factors to determine the level of biocompatibility. MTT assays, shown in Figure 3.2, were used to determine cell proliferation and viability, and AFM measurements, presented in (§ 3.3) and summarized in Table 3.1, were used to determine cell permissiveness to the substrate. AFM measurements quantified both the cell to substrate interaction and the permissiveness of the substrate.

Cell proliferation and subsequent membrane attachment on substrates is dependent on a complex combination of physical, electrical, and chemical reactions which are influenced by both surface and bulk substrate properties and the cell membrane structure [119, 120]. Cellular attachment to a substrate involves the absorption of proteins contained within the media serum to its surface followed by receptors within the cellular membrane binding to the absorbed proteins [131]. Subsequent membrane attachment, membrane spread, cytoskeleton polymerization, and cellular growth are controlled by the internal cellular cues initiated by these intracellular receptors involved in substrate-cell binding, and it has been demonstrated that this is heavily mediated by surface wet-ability and charge [131, 132]. Hydrophilic and charged surfaces allow extracellular proteins, like fibronectin (Fn) which are involved in cell membrane to surface binding, to unravel and elongate as it is absorbed onto the surface, whereas hydrophobic surfaces show Fn is absorbed in natural soluble form which is compact and rounded [133]. Cells show little reactivity with Fn in solution, so the chain elongation is one important factor for cell membrane reactions to occur [133]. Furthermore, cell

charge and surface wet-ability have been observed to be very influential factors for both surface interaction and neurite growth and guidance. Growth cone formation and filopodia/ lamellipodia guidance have been shown to favor a more hydrophobic surface [134]. Neurite formation and extension are also influenced by substrate charge, with this growth favoring positive charge over negative charge, and neutral charges produces almost no neurite outgrowth [135-138].

PSt treated through oxygenation for optimal cell attachment was used as a normalizing control for the MTT assay test and as a comparison for cell attachment and permissiveness in the AFM analysis. Proliferation of the H4 and PC12 cells was higher than the tested substrates with the exception of (111)Si for the H4 cells. The level of attachment of the cells to the PSt substrate showed some variation in that the AFM analysis indicated that the PC12s showed a low surface profile and large surface area spread for the cell membrane, while the H4 cells have a large angle of attachment, a subsequent high surface profile, and less surface area membrane attachment. The lamellipodia permissiveness was also much better for the PC12 cells than the H4 cells on this surface. This material has been shown to be normally hydrophilic, as indicated by Kim *et al*., and the material data sheet provided by the supplier, Corning Inc., specifies a H_20 contact angle of 12.3° - 16.3° [132]. This material has been also shown to often possess a negative surface charge [133]. The hydrophilic surface and the negative charge of this material would allow for elongation of attached proteins, and therefore could be a reason the cells have high proliferation to this particular surface. The negative charge could also be a reason for the improved cell attachment and lamellipodia extensions for

the PC12 cells, as was also found by Fine *et al.* and Schmidt *et al.* [133, 138]. However Clark *et al*. showed evidence that CNS neurite growth was more sensitive to charge when compared to membrane attachment and favored a more positively charged environment, and this may be a reason for the decreased H4 cell and lamellipodia attachment [134].

The untreated amorphous glass substrate surface was evaluated in this study as it has been used in traditional neural MEMS devices and is more hydrophobic than 3C-SiC and slightly less hydrophobic than Si, PSt and NCD, respectively, as seen by Sklodowska *et al.* which reports a contact angle of 51.05° [139]. Amorphous glass would also not provide a net substrate charge as it is an insulating material, but any charges that contact the surface would potentially remain in place as glass is a good insulator. AFM analysis showed that both cell lines tended to greatly minimize their contact with this substrate and have little lamellipodia surface attachment, although cells on this substrate displayed the largest areas of overall lamellipodia probing. The performance of the cells on this substrate is consistent with the previously discussed study results in that the extracellular proteins would probably remain in a natural form as they are absorbed onto the surface, therefore providing a lower number of membrane binding points [10, 133]. The neutral charged surface could be a large factor in inhibiting the neurite expansion, as was shown by previous studies [135-138].

Both faces of Si, which had been cleaned using the protocols discussed in the methods section, have been shown by Coletti *et al*. to have a measured contact angle of 65.85°, indicating a weakly hydrophobic surface [124]. The samples used in this study were doped with phosphorus which provides a negative charge potential within the bulk

of the material. The H4 cell line showed good viability for both Si surfaces with (111)Si showing a higher viability level than (100)Si to both cell lines. The H4 cells displayed a good level of cell membrane attachment but only a moderate lamellipodia attachment. A contradiction in the results was seen with the PC12 cell line interactions with the Si surfaces which indicated poor cell viability for (100)Si, but excellent cell viability for (111)Si. The AFM results support the MTT findings for (100)Si with a high cell profile, a large angle of attachment, and moderate lamellipodia attachment, but these same results does not support the MTT assay findings for Si(111). As Si is nearly as hydrophobic as natural PSt, and the samples would possess the same negative charge potential, the differences between the reactions of the cells to these two substrates may be due instead to the chemical properties of their surfaces. The evidence that this may be a plausible assumption is displayed in Figure 3.5(b), which indicates some chemical reaction between the cell membrane and the Si which has pitted the surface. Both of the Si substrates tested have different surface elemental Si concentrations, where (111)Si has three exposed but bonded Si atoms compared to the single bonded Si atom on (100)Si. Also, studies have indicated the presence of Si compounds present in the extracellular matrix of the CNS, and Si compounds are also found in blood plasma [11, 77]. The results of this study indicate that both cell lines may have a preference to bond with Si compounds, which may be the reason for the much higher proliferation on the (111)Si substrate than the (100)Si substrate, and the H4 cell line shows a preference to the (111)Si substrate that rivals PSt with higher viability and tight surface attachment. The lower viability of the PC12s on (100)Si is not so easily explained, but a lower membrane

attachment was shown by the AFM analysis which indicates that this substrate is not entirely favorable for this particular cell line. It is well known in the semiconductor industry that (100)Si reacts at much higher rates with many reagents than (111)Si, and the Si substrate immersed in solutes like water form silicic acid, which can have a negative effect on the cell viability when present in large quantities [9-11, 77]. The moderate lamellipodia attachment to these substrates is most likely due to the negative charge of the substrate, and mirrors the results seen by Fine, Makohliso, Young, and Schmidt *et al.*, but attachment of the lamellipodia may have been altered due to the hydrophobic substrate surface [134-138].

Intrinsic NCD showed a similar performance profile with the H4 cells as (100)Si by possessing a good level of viability, and the AFM scans showed a good level of cellular membrane expansion and attachment to this substrate. Alternatively, also like Si (100), there was a poor level of viability with the PC12 line and the high cell profile shows it does not favor this surface. The results of the lamellipodia attachment show this material has similarities to (100)Si as well. H4 cells had a moderate level of lamellipodia attachment while the PC12s showed a very poor level of lamellipodia attachment. Hydrogen treated NCD has been shown by Ostrovskaya *et al.* (via contact angle measurements of 75° - 95°) to be a hydrophobic surface which is mainly due to the large amount of sp^2 bonded graphitic defects along the crystal grain boundaries [140]. As this material is intrinsic like glass, there should be no appreciable surface charge, but some random charges may be present along defect boundaries and may be attracted by capacitive forces to the surface from charges in the Si semiconductor substrate. The

PC12s follow the previous studies of Rouhi and Kim *et al*. which show a low level of cellular viability and attachment due to a hydrophilic surface [131, 132]. The low level of lamellipodia attachment, almost equal to the level of amorphous glass, may be due to the intrinsic nature of the substrate as was seen in previous studies [135-138]. These conclusions do not account for the cellular attachment and viability seen by the H4 cell line. These cells should not be attracted to a surface as hydrophobic as NCD, but as the surface was grown in hydrogen ambient, the proteins may actually be attaching to the hydrogen on the surface instead of the carbon beneath. Protein and polymer surface modification has used hydrogen or O-H bonded surface terminations to attach specific proteins to the surface of semiconductors, and it may be that proteins in the media are attaching to the H-bonded surface of the NCD [31, 116, 117]. Further exploration into the surface properties of NCD and how this material interacts with extracellular proteins would be necessary to confirm this hypothesis.

Both crystal orientations of 3C-SiC, unlike Si, have high proliferation values with both cell lines when compared with the PSt control and the surface, shown in Figure 3.5(d), showed no adverse effects or surface degradation through cellular interaction. AFM indicated that the H4 cells have good cellular spread and low profile when deposited on the surface, and excellent lamellipodia permissiveness. A low angle of attachment and moderate level of cell spread was observed with the PC12 cells, and a relatively good level of lamellipodia attachment was also observed. The same discrepancy in the level of viability that was observed between the different crystal orientations of Si samples also exists between (100) 3C-SiC and (111) 3C-SiC, although

it is not as pronounced. Coletti *et al*. has shown the USF 'as grown' 3C-SiC has a contact angle of 52.53°, and Yakimova *et al*. indicated that 3C-SiC contains both hydrophilic and hydrophobic sites due to its alternating elemental surface from both island nucleation and defect structures [20, 124]. C rich 3C-SiC surfaces are extremely hydrophobic and Si rich 3C-SiC is hydrophilic [124]. It should be noted that these substrates were negatively charged throughout their bulk by the incorporation of nitrogen present during the growth process, although at a level much lower than the intentionally doped Si substrates. The fact that this substance is a hydrophilic material does not alter the viability level significantly from Si, which was hydrophobic; along with the observation that there is a similar viability contrast between the crystal orientations suggest that the cellular membrane may have some competing bonding principals.

Our earlier hypothesis is that Si provides greater protein absorption and is utilized in the extracellular matrix [9-11]. 3C-SiC, like Si, has more atoms per unit cell on the (111) face than the (100) face, and if the cell membrane prefers to attach to Si, the viability will be higher on the (111) face. As indicated by Figure 3.2, both Si and 3C-SiC possess this pattern difference in the viability between the two crystal orientations, but 3C-SiC has slightly lower viability than Si. NCD has lower viability than both 3C-SiC and Si, and is also a cubic faced material. NCD possesses wither C or C-H bonds on the surface, and a lower viability level than the (100)Si and (100) 3C-SiC faces, suggesting that membrane affinity is lower for elemental C than Si. As 3C-SiC falls between the two mono-elemental surfaces, the viability difference may be due to the different membrane affinities to the alternating Si-C bonds on the surface. 3C-SiC, like the PSt

and Si tested in this study, possesses a negative material charge, and presence of hydrophobic sites from Si on 3C-SiC surface would generate good lamellipodia extension, but the greater attachment of the lamellipodia may be due to the hydrophobic C sites on the surface.

The hexagonal polytypes of SiC, 4H-SiC and 6H-SiC, do not behave like their 3C-SiC counterpart with either cell line. Although 4H-SiC has a statistically equivalent viability level when compared to the 3C-SiC polytype for the H4 cell line, the AFM analysis shows circular to slightly elongated cells with a slightly elevated angle of attachment. The cells possessed small microtubule extensions and had a moderate surface permissiveness when compared to 3C-SiC. The PC12 cell line had a much lower viability with 4H-SiC than with 3C-SiC, which was more statistically comparable with the NCD and (100)Si substrates. Cells show more membrane attachment to this surface than many of the other substrates, but the lamellipodia attachment to the surface was poor. The other hexagonal substrate, 6H-SiC, had the worst performance of all the materials tested, which is contrary to Yakimova's *et al*. findings which shows this material had a good biocompatibility level [20]. The viability of H4 cells was lower than that on 4H-SiC and this material had the lowest viability with PC12 cells. AFM shows that the cells on both of these substrates were rounded to elliptical in shape with small microtubule extensions. The H4 cells had few extensions of the lamellipodia, but they were relatively firmly attached to the surface. The PC12 cell line showed little lamellipodia extensions as well, but this surface did not have the same level of permissiveness as the H4 cells did.

Although 4H-SiC and 6H-SiC did not show the same level of biocompatibility as was displayed by 3C-SiC, they display the effects of bulk charge on each of the cell lines. As seen in Figure 3.2, both substrates follow the same patterns when viewed by charge in respect to viability, and both cell lines have very different preferences. The H4 Cells show little difference between surfaces charged negatively or which are neutral, but have a definite dislike of positively charged materials. PC12s, on the other hand, favor positively charged material, and to a slightly lesser degree, intrinsic (neutral) material, but has a dislike of negative charged surfaces. It is interesting to note that both the Si and 3C-SiC substrates are negatively charged and still possess high viability. Later experimentation should be conducted to determine the charge effect with 3C-SiC and Si surfaces.

The fact that 4H-SiC and 6H-SiC react with the neural lines much differently than 3C-SiC is very difficult to explain. Ideally, 3C-SiC, 4H-SiC, and 6H-SiC all possess the same surface characteristics with the exception of unit cell spacing which would only affect the atomic step spacing as detailed in (§ 2.2). The Si-C bi-layer stacking of all the polytypes ideally create on the on-axis surface of the semiconductor a pure layer of Si atoms only, commonly designated the Si-face, and the opposite surface is C atoms only, or the C-face. Commercially available SiC, 4H-SiC and 6H-SiC, indicate these surfaces as both faces have different properties and processing techniques [141]. The samples utilized in this study are Si-face 4H-SiC and 6H-SiC, which was the same type covered in Coletti *et al.*, and should have a very hydrophilic surface with contact angles in the range of 20.3° for 4H-SiC and 25.2° for 6H-SiC [124]. The reaction of the SiC n-type surfaces

is similar to the reaction of both (100)Si and NCD, two materials much less hydrophilic than SiC. The contradictions of these two materials as compared with the previous findings used for this study warrant more study into the nature of the semiconductor surface in relation to the surface of a cellular membrane. As n-type 6H-SiC produced the lowest reaction, this material is an excellent candidate for future studies.

3.5 Summary of Chapter

This initial study of neural cell interaction with 3C-SiC and NCD has provided evidence that these materials may be suitable for use in an implantable BMI device. The results of this study indicate that 3C-SiC is very biocompatible to both cell lines and showed a relatively high level of cellular viability as compared to PSt treated for optimal cell growth. Cell morphology results showed that the cells attach very well to the surface of 3C-SiC and displayed excellent lamellipodia permissiveness, which is an important quality for BMI devices. Furthermore, the chemical resilience of 3C-SiC demonstrates that this material resists the surface degradation that was observed on the Si surfaces which resulted from cellular interaction with its surface. The as-grown NCD showed good viability and moderate permissiveness for the H4 cell line, but has a poor performance with the PC12 line. This result may be due to the fact that the NCD is hydrogen rich at the surface, but further investigation is needed to examine the neuron cell reaction on this substrate. Many of the neural reactions we observed to these substrates are similar to previous studies; however, many of the explanations utilized to explain the results are conjuncture and will have to be verified.

Future exploration which is proposed in (§ 4.2) will explore the surfaces of SiC and NCD and (§ 4.3) will propose an exploration of neural molecular interaction with 3C-SiC surfaces by examining the bonding of extracellular proteins to substrates. Experiments with alternative substrates or the utilization of surface modification with different processes will be used to explain the surface interaction. Verification of the charge effect on the cellular attachment using intrinsic, n-type and p-type doped Si and 3C-SiC substrates would provide more data for the reaction of the cells membrane attachment and lamellipodia attachment to different charge factors within the bulk substrate. Ostrovskaya *et al*. shows that the hydrophobic / hydrophilic nature of NCD can be modified through hydrogen and oxygen treatment after growth, so establishing an oxidation method for our NCD without etching would help give further evidence for the cell membrane reactivity with [140]. Finally, an examination of the extracellular remnants that remain after cell removal by AFM, XPS, and FTIR, then removal by centrifuge for examination using Western blot, or another protein separation test, could provide evidence as to the molecular interactions of the cell membrane and the substrate.

Chapter 4: Biocompatibility Improvement and Device Interactions

4.1 Introduction

Thousands of people are suffering from irreparable damage to the CNS which has one response to damage regardless of the cause - the glial scar. The glial scar restores the blood-brain barrier, the system that protects the CNS from external viral attacks. Unfortunately, the scarring process does not repair the neural signal pathways, inevitably leading to loss of body functionality and leaving the individual permanently handicapped. A proven therapy is available for the treatment of some of these conditions, the BMI, and implantable systems allow two-way communication with targeted individual neurons. Implantable BMI devices have shown that this technology can provide treatment for many problems with the CNS, but unfortunately it has one major Achilles heel. The implantable neural interface has limited lifetime due to the very process it is trying to repair, the glial scar. Science has agreed that the major cause of this problem is that the biocompatibility of the device and the materials of construction lead to a foreign body response from microglia and astrocyte cells. Finding a biocompatible material for these devices has become paramount for their continued application in the treatment of problems with the CNS system and this dissertation research has been focused on this goal.

3C-SiC, or cubic silicon carbide, and NCD, nanocrystalline diamond, are two possible materials for BMI construction. Both of these materials have properties that make them ideal for use as a permanent neural implant for the BMI system. The materials are mechanically resilient, chemically inert, and can be deposited on many different substrates. These materials are semiconductors which allow the customization of bulk electrical charge. One problem with the use of these materials is that they possess many crystalline defects that limit the electrical performance of electronic devices such as transistors and diodes. We have shown in (§ 2.2) that the quality of 3C-SiC was drastically increased utilizing low pressure CVD methods we developed. More importantly, we have also shown in (§ 3) through biocompatibility tests suggested by ISO 10993 that 3C-SiC shows an innate biocompatibility which is statistically comparable to cell treated polystyrene, PSt, with human CNS glial cells, and rat cells derived from the adrenal gland that correspond with cells that connect the CNS to the PNS. The same tests show that NCD is a good material for interacting with the CNS glial cells, but has some problems interacting with the adrenal cells. These same tests revealed some unexpected cellular behavior on the Si substrate and the alternative forms of SiC, 4H-SiC and 6H-SiC. Our conclusions from the tests have suggested that future investigations must be conducted before an implantable 3C-SiC/ NCD device can be constructed and tested *in vivo*.

The first set of proposed experiments will involve a substrate which showed the lowest biocompatibility, 6H-SiC. 6H-SiC was tested using the same protocols as placed upon the materials tested in (§ 3). (§ 4.2) will detail methodology to modify the surface

of 6H-SiC, and utilizing methodology covered in (§ 3), we will determine if any of the proposed modifications improves biocompatibility. (§ 4.3) will describe our work with primary cultures of mouse cortical neurons, which will be the first direct CNS neuron we have evaluated. The cells used for the work presented in (§ 3) were derived from cancerous cells, and thus have the ability to proliferate, but it is well known that these cells react slightly differently to electrical stimulus than primary, animal derived non-cancerous cells. Finally, in order to show that 3C-SiC and NCD are materials that can provide interaction with neurons, (§ 4.4) will detail our current experiments involving the neural activation device, or NAD. The NAD will utilize 3C-SiC as the base of an electrode-based device modeled after the Michigan planar probe as a basis, and will be used to send signals to neurons in order to elicit an action potential. The data obtained from the initial NAD, namely the electrical characterization and interaction statistics with neural cells, will allow for the design of a new generation of NAD's utilizing field effect devices instead of the electrode devices which is the subject of future work in (§ 5).

4.2 Semiconductor Surface Modification and Exploration

(§ 3.3) detailed the results of the MTT assay viability tests along with the cell morphology and lamellipodia permissiveness to the substrate evaluation as assessed by AFM. The results for many of the substrates tested were inconclusive as to the exact mechanisms that led to the observed results. Clearly, more exacting measures were needed to evaluate how proteins were interacting with the surface of the semiconductor and, in turn, how the cells themselves interacted with the absorbed proteins. The results

contained in (§ 3.3) and the literature supported explanations in (§ 3.4) detail that proteins absorb onto the surface of a foreign material based on its chemical composition, which dictates reactivity and surface wettability, and water retention. Another important factor for protein absorption and activation is the influence of electrical charge. As the materials we were testing are semiconductors, it is possible to alter the electrical characteristics by changing the doping impurity levels either during growth or through the addition of dopants during epitaxial growth. The goal of the next aspect of this work was to modify the surface chemical composition of the tested substrates to better understand how cells attach to the surface of these materials. With better knowledge of how the surface state influences cell attachment and viability, we can design specific modifications that will improve the biocompatibility of SiC with neural cells.

For many years, it has been recognized that the establishment of an inorganic/ organic interface is necessary for biological sensor applications, and this environment is more important still with any implantable device which will interact with the body for an extended period [4 – 6]. Thus studying the behavior of cells and proteins at a molecular level is crucial to our understanding of this interface. One method that has been gaining interest is the use of modified surfaces to test the cell or protein interaction. Specific covalent attachment and subsequent surface functionalization of organic molecules on inorganic semiconductor devices enable the targeting of specific factors that cause cancer, lead to heart attacks, and a myriad of other biomarkers that would allow early detection and prevention of many diseases. Stutzmann *et al.* at the Walter Schottky Institut (WSI) within the Technische Universität München in Germany has been

functionalizing semiconductor surfaces using self aligning organic molecules [142]. Stutzmann *et al.* utilizes a hydrogen-terminated semiconductor to covalently bond organic molecules in solution to the surface [142]. Predominately, Si has been utilized due to the ease of terminating the surface with hydrogen; however Stutzmann *et al.* theorized that SiC is electrically matched to organic systems because of its band gap size and position, and would make an interesting inorganic/ organic heterojunction [142]. Beginning in January 2009, we started a research collaboration with this WSI group in order to study the functionalization and subsequent improvement of the biocompatibility of SiC. (§ 4.2.1) explains the current work on the functionalization of 6H-SiC using covalent bonding of organic molecules, while (§ 4.2.2) will detail the results of the initial biocompatibility testing of these surface modifications.

4.2.1 6H-SiC Surface Modification Characterization

6H-SiC was tested using the same methodology as presented in (§ 3). Along with n-type semiconductor samples of the 6H-SiC, we were able to secure CMP polished p-type, n-type and intrinsic 4H-SiC samples for this study. The results, presented in Figure 3.2, were quite surprising in that 6H-SiC and 4H-SiC had either lower or extremely low viability levels with the two tested cell lines. Another interesting difference was the effect of semiconductor bulk charge which produced different results with the two cell lines. The H4 cell line seems to be in favor of n-type doped and intrinsic SiC, while the PC-12 cell line clearly favors p-type over intrinsic or n-type material. These trends were similar with both 4H-SiC and 6H-SiC, but at this time we have not correlated the viability

trend with Si or 3C-SiC; however that work is being conducted presently by A. Oliveros in our laboratory with S. Schoell at WSI and will be reported when complete..

Negatively doped (i.e., n-type) 6H-SiC was shown in our MTT assays and AFM analysis to have the lowest viability with both of our neuronal cell lines and very poor cell attachment, and virtually no lamellipodia extension for the PC12 cell line. This material is under study for surface modification by Schoell *et al*. at WSI, and the results of their recent research was presented at the European Conference on Silicon Carbide and Related Materials (ECSCRM) conference in Barcelona, Spain in September 2008 [143]. Our two groups decided to functionalize the surface of 6H-SiC and test it with these two cell lines.

To functionalize the surface of a semiconductor with a covalently bonded organic molecule, one needs either a hydrogen or hydroxide terminated surface. Hydrogen terminated Si surfaces have been achieved through surface treatment with diluted hydrofluoric acid or through high purity hydrogen etching [144, 145]. A monolayer of self assembled molecules (SAM) can be added covalently to the surface of the semiconductor using processes known as hydrosilylation or silanization. Hydrosilylation involves reacting long chain alkenes to the surface of the semiconductor through reactions with the hydrogen terminations at the surface, which breaks the alkyne double bond into an alkyl radical, and this radical forms a Si-C covalent bond with the surface [143, 146]. Silanization is a similar process but instead involves the surface and is terminated with a hydroxide which then interacts with organosilicon molecule chains which has one end of the chain containing Si bonded to alkoxyl groups. O-H

terminations react with the bonded alkoxyl groups, releasing the hydrogen to the alkoxyl groups, reducing them to Si-O-SI covalent bonds at the surface and between the end groups [143, 147]. These layers are relatively stable and can be further manipulated using lithographic techniques [143]. Oxygen plasma can be used to remove the molecules from the surface, and other biological molecules can be attached to the end groups of the SAM [143].

The methods of hydrosilylation or silanization can be used to terminate a SiC surface with a SAM, but certain differences are evident. First, treating (0001) 6H-SiC (i.e., the Si face) with HF does not create a hydrogen terminated surface as seen with Si, but creates a weakly O-H terminated surface which deteriorates in a matter of hours [148]. (000-1)6H-SiC (i.e., the C face) surfaces show a mix of O-H terminated and H terminated surfaces [148]. O-H termination is ideal for silanization, and hydrosilylation is still possible, but the reaction leads to a less stable, non-interfacial Si-O-C bonding condition, and can lead to possible defective bonding at the C site from CH_x species [143]. A more ideal condition for hydrosilylation is achieved through the H termination that emerges from hydrogen etching [110-113]. This process first generates a well ordered, atomically flat surface free of defects from CMP scratches through the hydrogen etching process covered in (§2.3), and subsequent cooling of the sample in ultrapurified hydrogen [110-113] terminates dangling bonds on the ordered surface with hydrogen bonds. 6H-SiC(0001) terminated in this manner has been shown to be relatively stable for at least 2 days, however Si(000-1) have shown increasing hydrocarbon contamination after only a few hours [148].

Schoell *et al*. have used diluted HF to O-H terminate the surface of (0001) 6H-SiC, and hydrosilylation the surface was achieved using an alkyl molecule, 1-octadecene ($C_{18}H_{36}$)which is based off their previous work with Ge [149]. Our hydrogen etching process and subsequent H termination of 3C-SiC should provide an optimal surface for the hydrosilylation of 6H-SiC [110-113]. Schoell sent us samples of (0001) 6H-SiC and (000-1) for hydrogen etching. We etched the samples using the parameters listed in Table 2.2, and cooled them in purified H_2 at 150 Torr to well below 400 ºC (which is our pyrometer's lowest temperature reading value) before performing an Ar purge and re-pressurization of the system to 760 Torr.

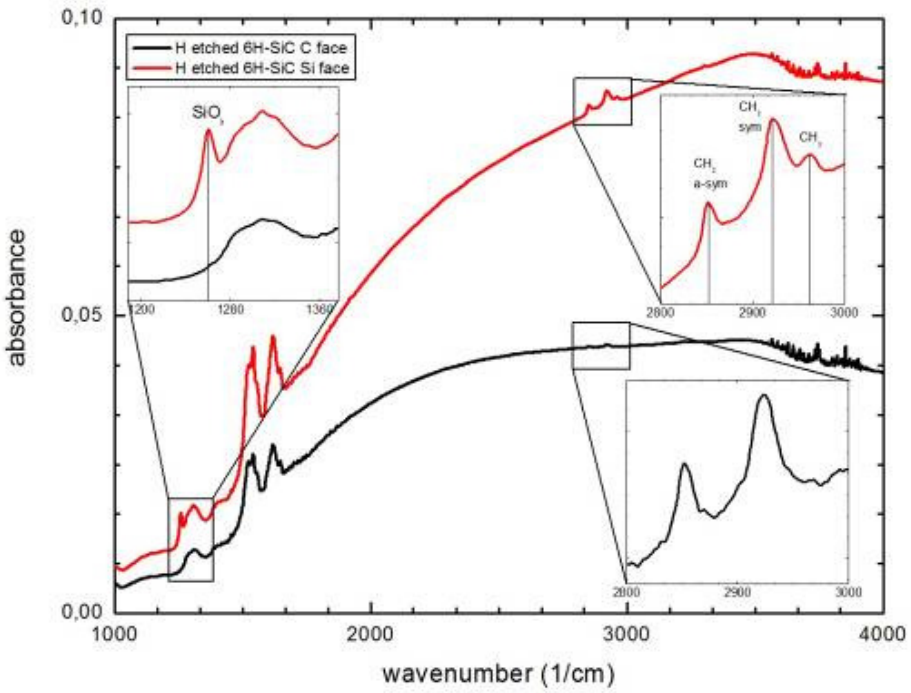

Figure 4.1: ATR-FTIR measurements of (0001) and (000-1)6H-SiC surfaces that have been hydrogen etched and terminated. After two weeks the (0001)6H-SiC shows oxide formation, however, the (000-1)6H-SiC shows an ordered hydrocarbon termination and no oxide formation. ATR-FTIR courtesy of M. Hoeb of the Walter Schottky Institut.

The samples were immediately removed, carefully stored in individual sample cases, and placed in an air-tight container which was purged with N_2 for 1 minute before sealing. The samples were delivered to WSI and measured using attenuated total reflection Fourier transform infrared (ATR-FTIR) spectroscopy. The measured results in Figure 4.1 show some very interesting results that differ from that presented in the work of Tsuchida *et al*. [148]. First, the (0001)6H-SiC surface, or the Si face, shows a definite oxide peak and shows considerable contamination from hydrocarbons as seen from the CH_3 vibrational peak. The (000-1)6H-SiC surface, or C face, has much different results and seems to present a more stable H terminated surface. This surface does not have a visible oxide peak, and does not have an appreciable CH_3 peak which would indicate hydrocarbon contamination. The CH_2 peaks, one indicator of C-H bonding, are present instead. This is significant because the samples were in transit for over 2 weeks, and it was unknown if the container was opened in transit by customs authorities which would have resulted in air exposure of the surface.

The electrical contact potential difference, or CPD, measured on hydrogen etched 3C-SiC surfaces by Coletti *et al*. shows a surface potential flat-band condition after our etching process which suggested that we had achieved H termination. In addition this surface electrical potential was completely stable for ~ 10 hours [111]. The surface potential was observed to slowly degenerate over ~ 1000 hours after termination, stabilizing at a surface potential of ~ -30 mV instead of returning to the surface potential of -160 to -191 mV present after HF treatment [111]. We had inconclusive XPS evidence leading us to believe that the surface was not Si-H terminated but instead C-H terminated.

We etched a (100)3C-SiC wafer, USF1-09-007, using the new low pressure process developed in (§2.3), and transported the wafer to Walter Schottky Institut in the same manner as mentioned for the 6H-SiC samples. The ATR-FTIR results are displayed in Figure 4.2, and show similar results to the (000-1)6H-SiC surface. The SiO_x peak is completely nonexistent, indicating that there is either a thin layer or no oxide present at all on the surface. There are the characteristic CH_2 peaks as seen in the 6H-SiC sample; also present is the CH_3 peak of contaminating hydrocarbons. The middle graph shows the peak wavenumber for C-Si-H bonds which provide an indication of the degree of hydrogen termination, but this peak is absent. Although we cannot be sure that the surface is terminated with hydrogen bonds, the surface nonetheless remained oxide free.

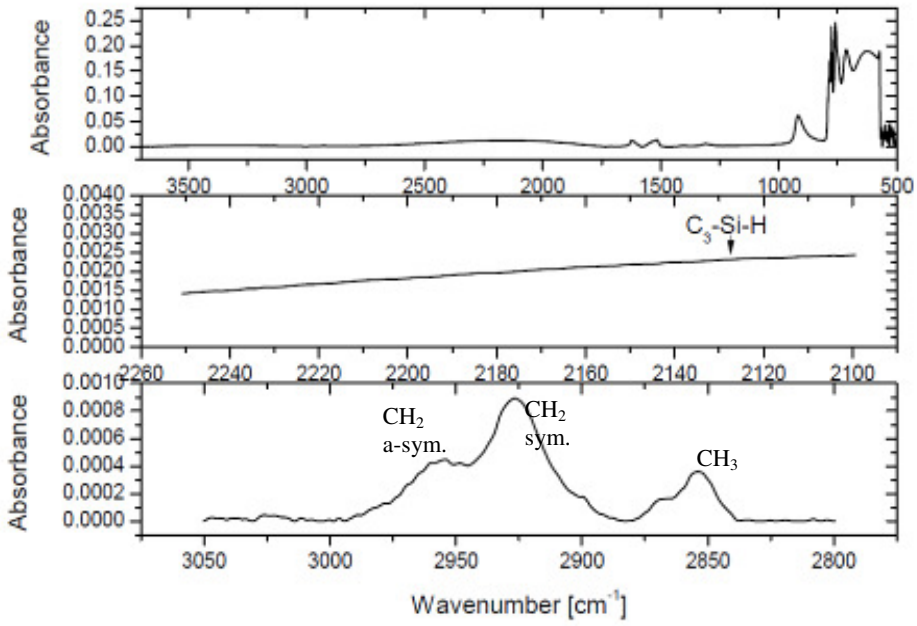

Figure 4.2: ATR-FTIR measurements of (001) 3C-SiC that had been hydrogen etched and terminated. The 3C-SiC shows no oxide formation and C-H termination, but has some CH_3 contamination. ATR-FTIR courtesy of M. Hoeb of the Walter Schottky Institut.

One notable difference indicated by this experiment was due to difficulties arising from sample transportation. The terminated 3C-SiC wafer was sitting for 40 days before ATR-FTIR measurement could be conducted, which puts this surface into the 1000 hour measurement time period in the work of Coletti *et al.* [111]. The ATR-FTIR measurements indicating a hydrocarbon terminated surface instead of an oxidized surface may be a reason why the original tested surfaces did not return to their original surface potential value long after hydrogen etching and termination.

We have obtained two Cree (0001)6H-SiC n-type wafers (3.43º off-axis, ρ = 0.055 Ω-cm, 420 µm thick) single side polished on the Si face. The Si face wafer was diced into 5 x 5 cm squares and hydrogen etched and terminated, but we sent the other wafer to NovaSiC Inc. for CMP polishing of the C-face side. The goal was to hydrogen etch and terminate both wafers at the University of South Florida and send the wafers to WSI where they will be subjected to hydrosilylation. Although it is unlikely that the hydrosilylation process will work properly with our H terminated (0001)6H-SiC surface due to the oxide as shown in Figure 4.1, we took extra precautions to try and deliver the samples with the termination intact to the WSI. The samples were placed in sealed boxes within zip-lock bags inside air-tight containers, and all were filled with N_2 gas. When the samples were received, they were immersed in neat 1-octadecence for 60 min at 200°C and subsequently cleaned in hexane, chloroform and methanol for 10 min each. The samples were then transported back to USF for cell viability testing via MTT assays. Contact angles, measured by Schoell, on the samples were slightly lower than expected, falling within the 80° range instead of ranges measured previously that were greater than

90° [149]. To see the affect of an increased hydrophobic surface on cell viability, we tested the functionalized samples using MTT assays. As we had information about the viability of the cells on CMP polished 6H-SiC, we tested hydrogen etched and terminated 6H-SiC samples alongside the functionalized samples which then served as controls.

4.2.2 Biocompatibility Testing of Modified Surfaces

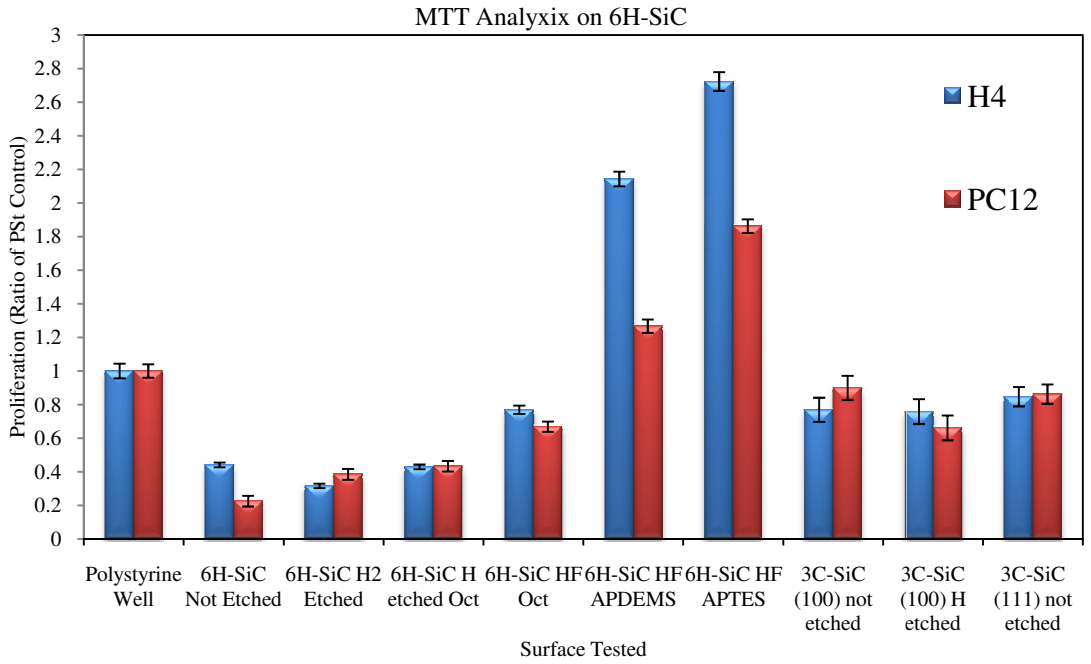

Figure 4.3: A bar graph displaying the results of the MTT analysis on 6H-SiC samples, normalized to the PSt control and then expressed as $\bar{x} \pm \sigma_m$. The results for the viability of PSt and 3C-SiC are included as benchmarks for comparison.

We repeated the MTT assay viability tests from (§3.2) on H_2 etched and terminated 6H-SiC samples as well as the 6H-SiC samples modified by hydrosilylation. As both surfaces of the semiconductors were specifically functionalized, we transferred the H_2 etched surfaces directly from the reactor to the MTT testing well and rinsed the hydrosilylation treated surface with ethanol before placing the sample in the PSt testing

well. After cell plating and the 96 hour proliferation time period, the MTT assay was performed. Figure 4.3 shows the results from the original 6H-SiC surface, the 6H-SiC surface that was H_2 etched and terminated and the 6H-SiC hydrosilylation processed surface treated with 1-octadecence on the H_2 etched and terminated surfaces. The results were not incredibly different for the H4 cell line, but there was a definite change in the viability level with the PC12 cell line. The H4 cell line prefers an un-etched surface and 1-octadecence treated surfaces over the H-terminated surface, while the PC 12 has greater viability on the 1-octadecence surface and just slightly less on the H-terminated surface. As was theorized before, proteins normally attach better to a hydrophobic surface, so a dramatic difference should have existed between the H etched surface, which would have a static water contact angle of 10 – 20 °C and the 1-octadecence static water contact angle of 80°. The effects were not dramatic, and mainly inconclusive, indicating that the surfaces of the 6H-SiC that were treated may not have been ideal. As we specified before, the surface may have had pinhole coverage due to the deterioration of the H-termination on the 6H-SiC Si face, which would have created patches of both H terminated and O_2 surfaces which would have prevented the surface reaction from occurring over the entire surface.

Next the 6H-SiC samples were cleaned using the piranha cleaning method and returned to WSI for the 1-octadecence treatment, again using a different surface termination structure. The surface was O_2 plasma etched two times followed by immersion in 5% HF solution. This creates the OH terminated surface that is immediately processed with the 1-octadecence. These samples were returned to USF and

evaluated using the MTT assay method. Figure 4.3 shows that this surface performed as anticipated. The levels of viability increased to almost to the same level as seen with the untreated (100) and (111)3C-SiC surfaces. This was almost a 50% increase in viability for both lines, which suggests that an extremely hydrophobic surface is better for cell viability.

Silanization of the (0001)6H-SiC samples was the next logical surface modification due to the inability to successfully maintain a long-term H surface termination. The process utilizes the easily obtainable OH terminated surface that was used for the previous functionalization experiments using 1-octadecence. The process uses our standard cleaning procedure explained thoroughly in (§3.2.2). The samples are then placed in 5% HF solution for five minutes followed by a thorough rinse with DI water to ensure removal of any fluorine radicals. The samples were then immersed in a solution of toluene and one of two aminosilane molecules. The first aminosilane molecule is (3-aminopropyl)-diethoxy-methylsilane, known commonly as APDEMS, and the second is (3-aminopropyl)-triethoxysilane, known commonly as APTES. For APTES, one end of the molecule's chain has multiple methoxy radicals, CH_3O, molecules bound to a Si atom, while an amine, NH_2, is bonded to the last electron site available on the center Si atom. APDEMS has almost the same structure possessing two methoxy molecules and a single methyl, CH_3, molecule linked to the Si atom through a Si-C bond. The coating solution is mixed at (100:1) toluene to aminosilane. The samples must be prepared inside of a fume hood as the reaction releases gaseous methanol, H_3COH, which is both a flammable hydrocarbon and can cause blindness and skin

irritation. After 90 minutes, the samples were removed and cleaned in toluene and isopropanol for 20 minutes each within an ultrasonic bath to remove physisorbed molecules from the surface. The samples were then dried with nitrogen and immersed in ethanol until cell seeding was initiated.

The results from the MTT assay were considerably better than for any of the surfaces tested to date. The H4 Cell line had a viability of a little better than two times that of cell treated PSt with the APDEMS, and was approaching three times that of APTES. The PC12 line was a little less volatile, displaying a viability of 1.2 and 1.9 times that of cell treated PSt. These results were anticipated as these functionalization molecules have an amine molecule on the end of the chain which reacts readily with reactive amino acids and proteins. The MTT suggests the amine better viability and proliferation. The surface is much less hydrophobic than the 1-octadecence treated surface, and static water contact angles measured at WSI were approximately 50° [143]. Another observation is the APDEMS, which contains one less oxygen bound to the Si atom, has lower viability with both cell lines than the surface of APTES. It should also be noted that these results are preliminary and not conclusive. The previous experiment detailed in (§3) requires that other independent measurements must be performed to assess a cell reaction to the surface. As we have performed measurements of the cell's surface morphology and lamellipodia permissiveness on previous samples, we will repeat the AFM measurements again to allow comparison with the earlier study. Also, the tests only evaluated chemical changes to the surface, and neglected the charge differences caused by the capacitance of the new layers or charges introduced by the layers

themselves. It has been shown that these modified surfaces do alter the surface charge, and we need to measure and account for these changes before making any real conclusions [143, 149].

4.3 Mouse Primary Cortical Neurons (CTX) on 3C-SiC

Experimentation for the determination of the bulk biocompatibility of neural cell lines has been performed by our group; however the cells utilized were from immortalized cell lines. Generally, immortalized cell lines do not behave in the same manner as their *in vivo* counterparts due to the fact that many of these cells are derived from cancer cells. Immortalized cells have an advantage in the fact that many of them are easy to maintain, and they have the ability to proliferate quickly on promoting surfaces. The H4 and PC12 cell lines are no exception to this fact, as both were derived from cancerous tissue, and unlike healthy neurons, they do proliferate. For completeness to this research, and to further our understanding of the cell-semiconductor interaction, neural and glial cellular attachment to our surfaces needs to be evaluated with cells obtained from primary sources. We have begun a collaboration with Dr. Maj-Linda B Selenica, a biochemist at USF who is currently extracting cortical neural cell cultures from mice for modeling chemicals and enzymes in the CNS. Nominally, the cells are collected from embryonic mice from approximately the 15^{th} to 18^{th} day of gestation (E15-18) and plated for 7 days to allow for cell adhesion and neural differentiation. The eighth day marks the first day of neural maturity and testing nominally begins at that point. Dr. Selenica normally has more cells than is necessary for her experimental needs, so we

proposed to repeat the MTT and cell attachment experiments from (§3.2) using mouse primary cortical neurons, CTX.

4.3.1 Cortical Cell Biocompatibility Testing

Primary neural cultures are much more delicate than the immortalized cell lines utilized in our previous studies. The initial experiment involved cells plated in a 96 well plate that was left over from a previous experiment. They had been plated with a count of 125,000 in poly-L-lysine wells, and at day 7 we attempted to collect them using 5% trypsin. The cells were re-plated on our semiconductor surfaces in accordance with the processes described earlier in (§3.2). The bare substrates that were compared in this study were the (100) and (111) faces of Si and 3C-SiC/ Si along with deposited NCD. The MTT assays were not readable for any of the substrates tested including PSt, indicating that the trypsin process most likely killed the delicate cells. The decision was made to plate the embryonic cells directly on the semiconductor samples for the next experiment.

The second attempt for gathering the CTX cells began with an unpleasant revelation. The pregnant mouse that was to be used for the experiment had given birth to pups. We only had the E15-18 protocol, so it was utilized to collect primary 1-2 day postnatal CTX cells. After 12 days (8 for the cell maturation, attachment and differentiation plus 4 days for the assay), we performed an MTT analysis. The resulting data collected, seen in Figure 4.4(a), indicates that (111)3C-SiC has great viability with the CTX cells and equal to that of the PSt control. (100)3C-SiC however was just above

40%, and the rest of the samples were at less than 20%. These cells were not usable for Dr. Selenica, as the statistical population was too low to make any legitimate claims, and replication of this experiment will not be possible in the near future. The results served as motivation only to develop a protocol for the CTX cells that allows experimental repetition. As a point of reference pure neuron cultures of post natal cells have a limited lifetime potential of about two weeks as reported in the literature [153].

Neuronal plating media contains horse serum, but this media is replaced 2-4 hours after plating, at which time the media is without serum. As we were using non-coated 3C-SiC, serum was thought to be critical for cell surface adhesion and viability. We repeated the MTT experiment on the semiconductor surface and added a new testing surface, Kapton® tape, a brand name for polyimide. As polyimide is the current leading construction material for neural interface devices, inclusion and comparison of its biocompatibility is paramount to establishing the biocompatibility level of 3C-SiC. The third plating, using E15-18 CTX cells, was maintained for the maturation and MTT time requirement, and the results of the assay are displayed in Figure 4.4(b). A noticeable improvement is seen between the Si and NCD surfaces which are double than the previous experiment, but still around half that of 3C-SiC. However, there are viability differences between the crystal faces, as the (100) face has greater viability than (111) for both 3C-SiC and Si substrates. Also observed is that the new additional tested substrate, Kapton tape, shows slightly more viability than (100)3C-SiC.

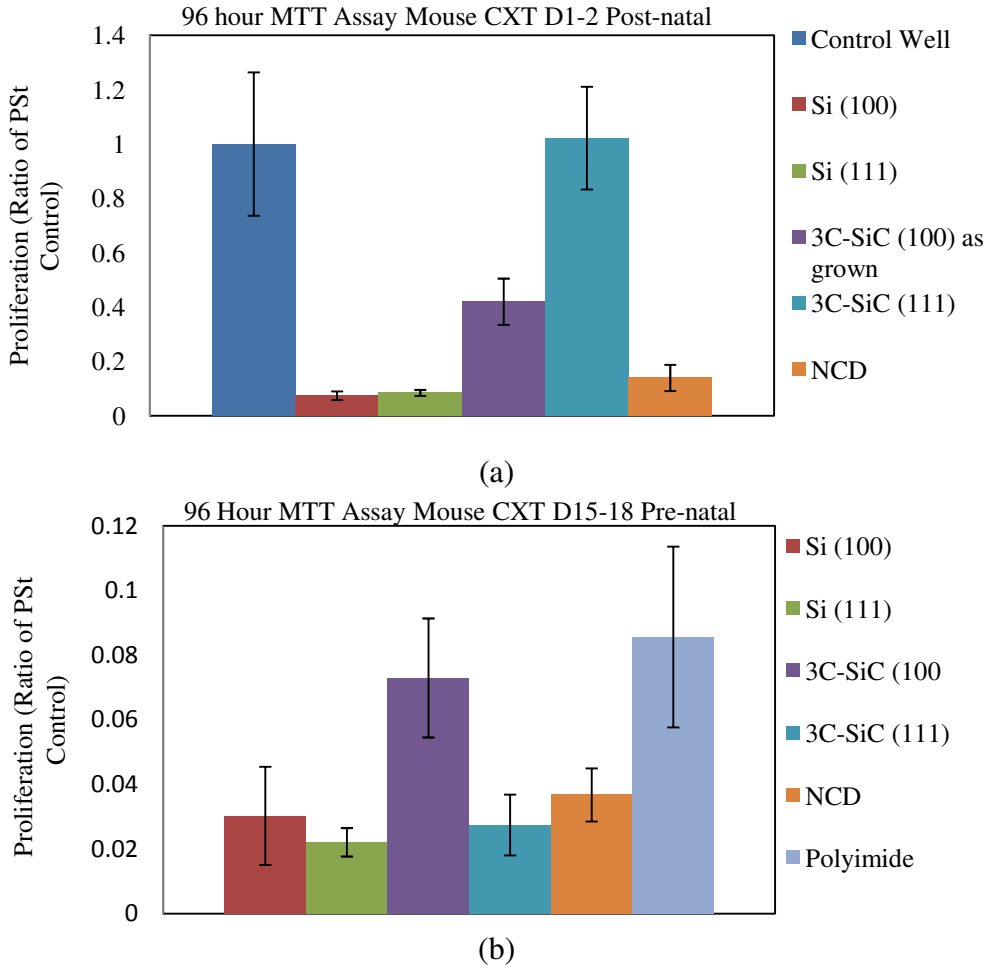

Figure 4.4: The results of single MTT assays performed with triplicate samples expressed as $\bar{x} \pm \sigma_m$. The graph of (a) displays the resulting MTT of D1-2 post-natal CTX cells plated in 96 well plates and seeded on semiconductor samples. (b) shows the MTT results of E15-18 prenatal cells plated directly on the samples after their collection and dissolution from the mouse cortex. (a) is normalized to a polystyrene control, whereas (b) did not have enough cells for a complete MTT and the PSt was not seeded.

One major discovery is that after the eight days the cells were not showing signs of neural differentiation. Although a few cells show spontaneous axon or dendritic extensions, many still appear rounded with no extensions whatsoever. Literature research points to two factors that cause differentiation in cortex cells. One is a surface with the proper chemical factors, such as the amino acid poly-lysine, and the other is a surface

from actual plated astrocytes [154, 155]. The next preliminary experiment involved investigating the neural differentiation on the surfaces of the semiconductor. We plated half of our samples with poly-L-lysine, PLL, and the others were left with their natural surface chemistry. We then examined the cells every day to monitor cell morphology, adhesion, and the differentiation process through the 8 day period after seeding. AFM and SEM were to be utilized to visualize the cells, quantify their morphologies, examine the cells for lamellipodia extension, and evaluate dendritic, or axon, extensions. The images from the SEM in Figure 4.5(a, b) and AFM in Figure 4.5(c, d) show examples of fixed cells on the surface of PLL treated PSt.

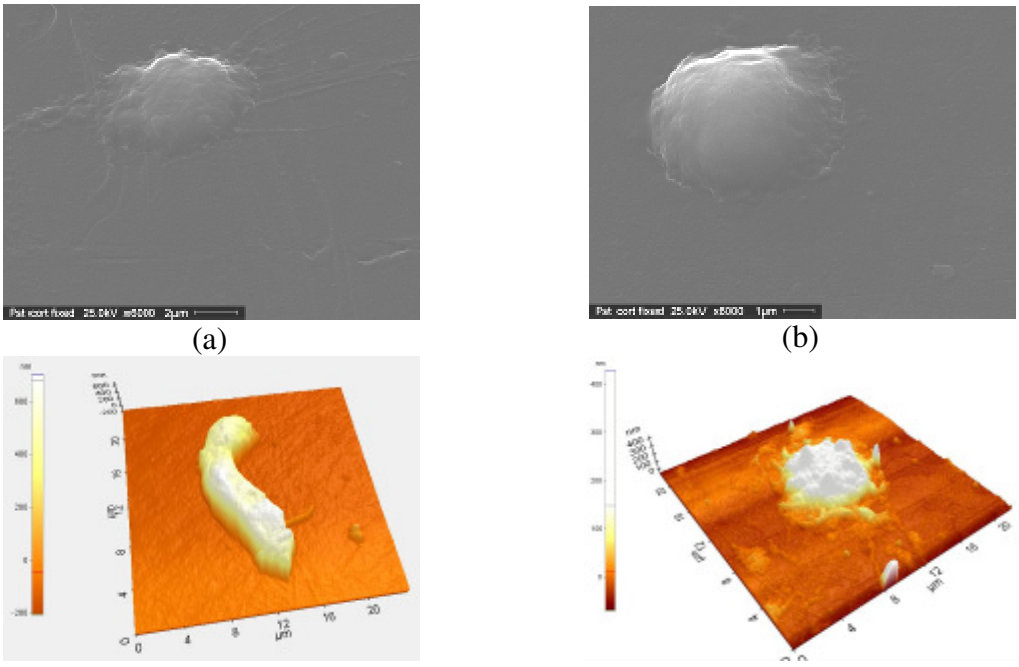

Figure 4.5: SEM micrographs of PLL coated PSt sample (a) with cortical cell imaged at 25KV and 8000X (scale bar 1um) and (b) a cortical cell at 25KV and 6000X (scale bar 2um). (c) shows a three dimensional image of CTX on PSt, bare substrate at day 6 and (d) shows the CTX on a (100)3C-SiC PLL coated substrate at day 8. SEM and AFM courtesy of S. Saddow and A. Oliveros, SiC group at USF, respectively.

The resulting section has shown preliminary results of this ongoing research. Our first goal is to create protocols that produce the same CTX cell quality, with repeatability between harvests, so as to produce statistically relevant results. The future work for this portion of this research will be covered in (§5.4).

4.4 Neural Activation Device (NAD): Generation 0

The ultimate goal of this research is to demonstrate action potential stimulation in neuronal cells via a SiC-based electrical stimulation device, which we have called a neuronal activation device, or simply NAD. Before discussing details of this preliminary work, it is instructive to look at the general principles involved in neuronal cell/electrical stimulation and for this discussion we divide the story into two parts. The first part is what is called a conductive or electrode-based device, which is the principal behind devices like the Michigan probe. The second type of device relies on the use of an electric field that is applied via a capacitor, with no metal necessarily contacting the intracellular fluid (aka media). Figure 4.6 depicts the electrical situation for these two types of stimulation by first showing the semiconductor/media model (left side of figure) depicting ion position, the Helmholtz electrical layer, etc. Next, the figure depicts the equivalent electrical circuit followed by a plot of the required stimulation waveform that must be applied to induce an action potential in a neuron. Figure 4.6(a) outlines the situation for an electrode based device and Figure 4.6 (b) for a capacitive based device.

This research has been primarily focused on the growth improvement, as seen in (§2), and biocompatibility of 3C-SiC and NCD with neural cells, as explained in (§3) and

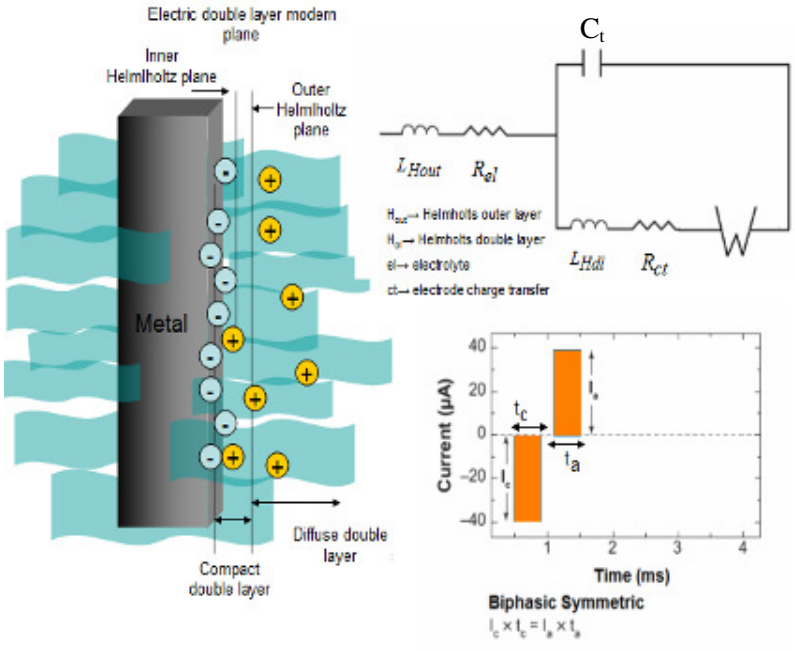

(a)

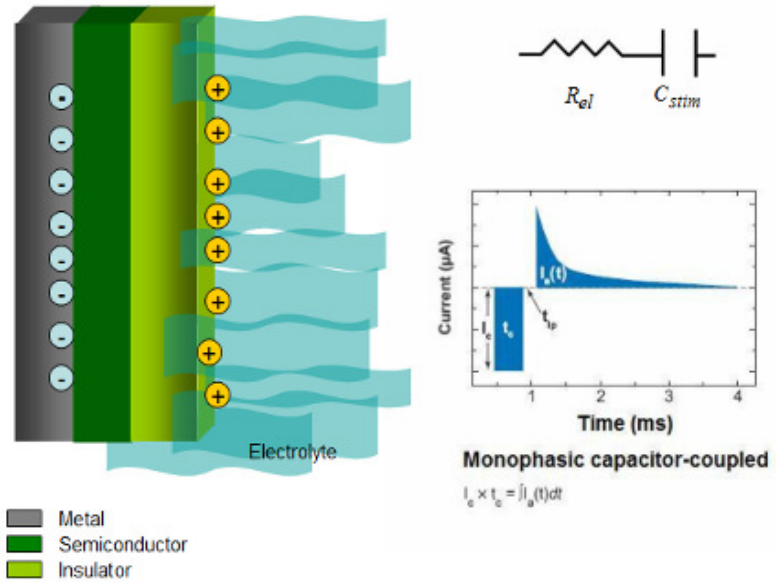

(b)

Figure 4.6: Simplified cartoon representations of an (a) electrode-electrolyte interface and a (b) metal-insulator-semiconductor (MIS) capacitor device and an electrolyte which was covered in detail within (§ 1.3.4 and 1.3.5). Included for reference are the simplified interactions occurring between the interface of the metal or insulation and the electrolyte. Insets show representation of a time current graph for the signals necessary to safely initiate an action potential in a neuron.

the previous sections of this chapter, but the goal of these experiments was to establish the use of these materials for eventual utilization in an implantable neural interface that would be the basis of a BMI device. The NAD device was designed as a testing platform to explore the electrical interface between the semiconductor and the neuron. The first NAD device, called NAD Generation 0, or NAD0, is a simple electrode based device which has been electrically characterized since the initial Michigan probe was created in 1970 [1-5, 13, 14]. Because 3C-SiC contains defects from the growth process, and normal growth at low pressure generates highly resistive material, this device will consist simply of 3C-SiC base layer, metal electrodes, and an SU8 insulation layer to prevent electrical cross-talk between adjacent conductors. This device will interact with the cell through the extracellular media through complicated electrochemical reactions of a metal electrode in electrolytes as explained in (§ 1.3.4) and displayed in Figure 4.6(a). NAD0 will use gold as the metal contacts with a thin layer of titanium underneath which provides contact adhesion to the semiconductor.

4.4.1 NAD0 Activation of a Neural Action Potential

The generation of the NAD0 device began in December 2008. The circular contact and wire dimensions were based on the PC12 and H4 average cell sizes obtained by AFM measurements in (§3.3) which were observed to be on average typically 30 µm wide by 60 µm long. Unfortunately, as money was an issue, we had to settle for a larger mask design on an acrylic film which had a minimum feature size of 50 µm. The final NAD0 device is an array of 64 cell interaction pads, 100 µm in diameter, connected with

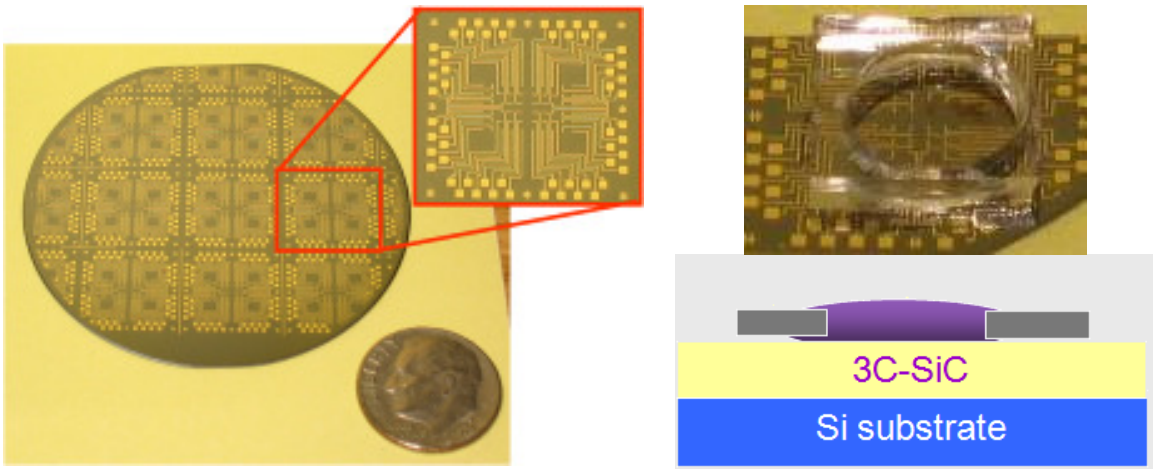

(a) (b)

Figure 4.7: The NAD0 device generated on 3C-SiC consisting of gold leads and a polyethylene gasket. (a) displays a 50 mm wafer with multiple devices and a dime to indicate the size of the device. (b) shows a photograph of the completed NAD0 device with the polyethylene well added and a cartoon representation of the device with media within the well. Device fabrication performed by A. Oliveros and S. Saddow, USF SiC Group. PDMS provided by S. Dupont, USF Chemical Engineering Dept.

50 µm leads to 500 µm square contact pads for eventual wire bonding to a package. Signatone SLM micropositioner metal probes would initially provide electrical connection between the contacts and the signal generator which would be utilized to send the biphasic square-wave pulse between two adjacent electrodes. The device was simply created from two masks. The first was the mask for positive photoresist designed for the metal lift off process to define the metal electrode contact geometry. The second mask was for the negative SU8 photoresist layer to provide electrical insulation and isolation between adjacent wires once the cell media was deposited on the structure. The mask was simply 300 µm diameter holes centered on the cell interaction pads to isolate each electrode. Figure 4.7 shows the completed NAD0 device layout which was fabricated from a two (2) inch 3C-SiC film grown on (100)Si. A piece of PDMS was used as a cell

media containment well, and the PDMS was provided by Samuel Dupont of Dr. R. Toomey's group in the USF Chemical Engineering Department.

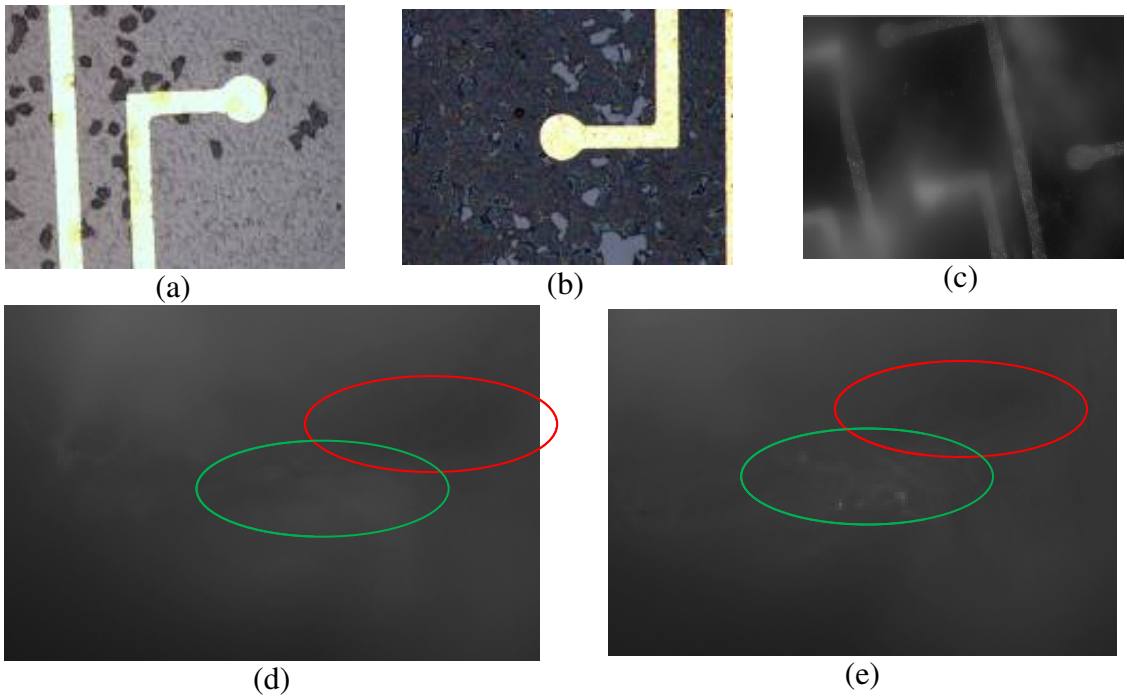

Figure 4.8: Electrical activation of cell action potential via the SiC NAD0. Optical microscope images showing undifferentiated PC12 cells seeded on the NAD fixed with formaldehyde. Image (a) shows proliferation after 1 day and (b) indicates that the PC12 cells proliferate across the entire device after 5 days. (c) shows differentiated PC12 which have become peripheral neurons. (d) and (e) show the device before biphasic wave activation and after the pulsing had began. As few cells fired, we have added a red circle to indicate the same, less populated area on each image, and a green oval to indicate the area where the AP activated cells originated.

The NAD0 die were diced by C. Locke of our USF SiC group, which yielded about 7 complete die with a total of 12 usable die. A NAD0 die was selected for experimentation on which we seeded cells to evaluate their size in relation to the electrodes. Figure 4.8 (a) and (b) show the difficulty in estimating the amount of cells to seed. 200,000 cells were seeded in Figure 4.8(a) and measured the next day with little

change in cell population; however, after 5-6 days, the PC12 and H4 cells proliferated across the surface of the device. We then seeded 50,000 cells in a 2" Corning Cellbind® Petri dish and added NGF at 20 ng/ ml to the media to induce differentiation of the cells into peripheral neurons. The cells were allowed to mature for approximately seven days in an incubator until they differentiated, then they were collected and plated on the device. As the cells continue to proliferate until differentiation, the result was a tissue-like mass of interconnected peripheral neuron cells which would not disassociate even with 100% trypsin. After the best disassociation possible, the cells were plated on the NAD0 device and a Ca^{2+} sensing dye, Rhod-2, was added to the media and incubated for 60 min to allow dye uptake and cell surface attachment. Figure 4.8(d) shows the cells on the surface of the NAD0 device, and the cloudy appearance of the photograph is due to the dense population of cells on the surface.

Following the incubation uptake period, the NAD0 was placed under a microscope in Dr. Weeber's laboratory at the USF Byrd center equipped with fluorescent filters that was housed in a Faraday cage for electrical noise reduction, and electrical connection to a waveform generator located outside the cage was made. We activated the NAD0 with an alternating, balanced, biphasic square wave electrical pulse consisting of a cathode phase followed by a slight hold sequence and an anodal pulse. This stimulus was made between two electrodes. The pulse frequency was set to 1 KHz, and pulse amplitude started at 10 mV and was increased manually in 10 mV increments approximately every second. During action potential firing, voltage-gated calcium channels (VGCC) will open and allow Ca^{+2} exchange into the cell, which is then

hydrolyzed to Rhod-2 by endogenous esterases producing a change in fluorescence. The increase in fluorescent excitation was captured by a camera attached to the microscope. At peak to peak voltages of ~300 mV, the neurons went from a non-active status seen in Figure 4.8(d), to active action potential as seen in Figure 4.8(e). It should be noted that only the cells nearest or in actual contact with the edge of the electrodes experienced action potential activation and only a few cells experienced the activation that were in contact with the electrode. This may be due to the fact that cells above and adjacent to the activated cells were not synaptically connected and would not have the proper neurotropic factors delivered to them from the adjacent neurons. As of the time of this work, we are still investigating the activation of neural action potentials by the NAD0.

The success and failure of NAD0, our first attempt to activate a neuronal action potential with a microelectronic device; has nonetheless shown that 3C-SiC can be utilized as a support for an electrode device for neural activation. Device redesign with smaller electrodes, easier electrical interface capabilities to external equipment, and better biological cellular protocols are all necessary and have been planned. A field effect NAD and a control electrode NAD constructed from Si will also be constructed to provide alternative and comparative data. Eventually, we will utilize primary cortical and hippocampal cell cultures, which contain cells directly from the CNS, instead of the immortalized PC12 cell line. We will also use (via the USF electrophysiology core; Dr. E. Weeber, Director) whole-cell current clamp methods so we can quantitatively measure the cell membrane current and voltage changes [156]. Different pulse widths and current densities will be evaluated to determine the complete device characterization and cell

reactions for eventual computer and biological modeling purposes. Cross talk, noise levels, signal loss across the ionic media, distance of signal transmission, and the levels of electrical excitation that create irreversible Faradic reactions at the metal-electrolyte interface will be explored for the NADs. Through the use of the whole cell current clamp, we can examine and quantify the reactions of the neuron to the electrical stimulations.

The results of this future study will determine if 3C-SiC is a material that can act as the basis for a neural prosthetic, and more importantly, it can show that this material can be used for a capacitive based device instead of an electrode device. The potential of this demonstration is enormous in that not only can we extend the life of neuronal implants using 3C-SiC, a biocompatible material, but with the MIScap field effect device which we can tailor specific and controlled electrical fields, allowing for more efficient and controlled activation of neural action potentials. Not only is the cost of patient care likely to be reduced with successful BMI applications, but the quality of life will be significantly improved. No longer will non-neuronal compatible materials be surgically implanted in the brain only to wait for device failure in the near term.

4.5 Summary of Chapter

While in (§2) the focus was on material development of both 3C-SiC and the combination of NCD on 3C-SiC, and (§3) specifically focused on the *in vitro* biocompatibility of the bulk materials, this chapter shows the division of our research into three new parallel tracts. These new areas of research are focused on the generation of a device that will interact with neurons indefinitely within the human body.

The first new investigation was the modification of our surfaces to generate better interaction between the biological cells and manmade semiconductor materials. Through silanization of 6H-SiC surfaces, this goal was achieved, and that material showed drastic increased biocompatibility. Our second investigation was to begin to work with cells directly obtained from an animal donor instead of from immortalized, cancerous cell lines. The initial results of this work are even more promising, showing that 3C-SiC has good biocompatibility comparable to Kapton® polyimide, which is utilized in long term neural implants currently to solve the biocompatibility problem of silicon implants. Our third investigation begins to demonstrate 3C-SiC's ability to be utilized as a platform for neural communication. The NAD0 device was able to activate differentiated PC12 cells, although many improvements to both the device and cell protocol must be made before action potential activation is truly confirmed The chapter (§5) will detail the future work our group is proposing to accomplish.

Chapter 5: Future Work

5.1 Introduction

The future work outlined in this chapter details the problems that must be overcome for the development of a successful neural implant and later the development of an entire BMI device system. The first hurdle is the ever present biocompatibility issue. We recently began to study biocompatibility by utilizing surface functionalization and will continue to work along this route. We will include not only the immortalized cell lines we have used in the past studies, but move on to a more relevant primary cell line derived from the brain itself. (§5.2) will detail future work and exploration of various surface modifications, and we will be performing these modifications in conjunction with WSI. The combination of the new cell lines and surfaces should assist in quantifying and modeling cellular response to inorganic surfaces, a benefit that will help not only neural implants but all implantable biomedical devices. (§5.3) will detail future plans for continuing biocompatibility testing with not only primary mouse cortical cells, CTX, but the addition of primary mouse astrocytes, microglia, and the eventual culture of hippocampal tissue slices. NAD0 successfully activated an action potential of a cultured neuron. (§5.4) will detail our plans for new NAD generations which will eventually provide true two-way communication between electronic semiconductor devices and CNS neurons. More importantly, we will begin utilizing a higher order

tissue for these new experiments which not only can provide additional electrical data, but also indicate the level of bioreactivity from multiple integrated cells. The exploration outlined in this section will be exciting and illuminating for the 'dark horse' of the silicon carbide polytypes, cubic silicon carbide, and will have the ultimate goal of producing a BMI interface which will be suitable for extended implantation *in vivo*.

5.2 Cell to Substrate Interaction Study

The results of the MTT assays from the silanization of the surface of 6H-SiC shows that we can increase the biocompatibility of a substance using SAM, but extensive research is required before we can incorporate this technique into a device, or use the method to better understand the mechanics behind the chemical interactions involved in cell membrane attachment to a surface. The next step in understanding the ability of the SAM to coat a surface uniformly is to use (000-1) 6H-SiC (i.e., C-face) substrates with the process. The C-face of SiC has been shown to have more defects and surface abnormalities, and the OH termination generated by HF immersion has been shown to possess interdispersals of H terminations [143]. This will decrease the SAM monolayer generation from silanization, but the results from our H_2 etching displayed in Figure 4.1 show promising results for the long term hydrogen termination, which may lead to a better surface from hydrosilylation. Testing the viability of the H4 and PC12 cells using MTT assay on the (000-1)6H-SiC samples is the next stage of this exploration. We need to include unetched H terminated, 1-octadecence hydrosilylation and silanization samples using APDEMS and APTES.

5.2.1 Surface Modification and Biocompatibility Improvement

Surface charge has been shown to affect the activation of proteins absorbed on the surface of inorganic substances, and we have shown that the viability of cells is affected by bulk charge within a semiconductor as was evident with the results displayed within Figure 3.2. The advantage of using SAM termination of the surface is that it has been shown to prevent native oxidation of a substrate, and therefore modify the charging characteristics of the surface [149]. Silicon carbide has a thin layer of native oxide, but it tends to be of less quality than the oxide on Si due to the effects of C which either incorporate at the oxide interface as a defect or becomes a vacancy by forming CO_2 [150]. We need to perform charge profiles of the surface for the SAM coated substrates in air and within the cellular media, characterizing the material using CPD measurements, capacitance - voltage (CV), and current - voltage (IV) profiling. The final substrates that need to be included to complete the charge profiling study are intrinsic and positively bulk doped (i.e., p-type) 6H-SiC. Understanding the changes that these surfaces make to the charge level will help us understand the protein and viability changes seen with the MTT assays and develop methods to use the SAM layers to manipulate not only the surface wettability, but surface charge as well.

The MTT analysis and surface characterization are not complete without inspection of the cell morphology and lamellipodia extension permissiveness analysis. As with our earlier experiment, AFM of both living and fixed cells on the evaluated substrates provided quantitative information that can be used directly for this type of inspection. The difficulty that AFM has is that it can only look at a single cell or part of

two cells. As it was difficult for us to obtain fluorescence microscopy measurements due to the substrates being opaque, we will use the SEM to investigate multiple cell populations. Coating the sample with a few nanometers of gold after measurement of the fixed cells in the AFM allows us to utilize the electron microscope (SEM) to examine the surface of the semiconductor on a larger scale. The arrangement of cell populations will show if cells are establishing connections between one another, which for neural and glial cells is another measurement of the natural cell evolution.

Cell adhesion to foreign materials is not well documented or quantified, and much of what is known has been gathered from the cell adhesion studies to glass substrates possessing surface modifications [120-124, 127]. Using both the SAM layers and untreated substrates, we will attempt to examine the adhesion of proteins that enable cells to adhere to materials, and we will attempt to identify specific adhesion proteins used by the cellular membranes to attach to the substrates. The first experiment is to look at surfaces that have been immersed in media with serum with the AFM and ATR-FTIR. The AFM not only measures surface morphological differences, but can be used to detect changes in surface friction, and can be used to perform force microscopy [151, 152]. Bergkvist *et al*. has shown that the AFM can be used to detect changes in proteins absorbed on a surface, and Dufrêne *et al*. has shown that force microscopy using surface modified cantilevers can identify certain protein characteristics [151, 152]. We will utilize similar AFM techniques to attempt to identify the proteins that absorb to the surface of the 6H-SiC from the serum media, and we will attempt to determine if the proteins are activated and elongated, or compact and unreactive. We will then utilize the

ATR-FTIR and XPS to examine and characterize the chemical composition of the protein absorbed surfaces. The next stage will be to remove the cells by scraping and trypsinization to examine the protein complexes left on the surface. Using the same techniques, we can attempt to characterize which proteins and cellular complexes have been left behind, and correlate information from the different surfaces to observe changes in cell adhesion. Another method for cellular attachment is to utilize fluorescent molecules attached to the aminosilanization modified surfaces. Schoell attached an amino acid, glutaric dialdehyde, to the amine at the end of the silanization chain, and utilized the amino acid to attach Alexa488 fluorescent labeled BSA proteins [143]. We can utilize the same process and allow the cells to attach to the surface. Potentially, the cell will displace the BSA proteins and attach to the surface, and we will be able to utilize fluorescence microscopy to quantify the cytoskeleton focal points. The utilization of the cell morphology, protein attachment, and viability will enable us to develop a more concrete vision of the attachment of cell membranes to SiC and SAM modified surfaces. This knowledge can be used to help formulate a device which can be recognized as part of the extracellular matrix instead of a foreign object.

5.3 Primary Mouse Cortical and Astrocyte Cell Biocompatibility Study

Clearly, the results obtained in (§4.3.1), while showing lots of promise, are still within the developmental stage. Although we can produce the primary neural cell lines, they have not reacted in the same manner regarding the same stimulus as the immortalized PC12 and H4 cell lines. The first order of business will be to establish a

proper protocol for the generation of CTX cells which produces comparable cells between different experiments, and these CTX cells will experience differentiation into neurons after 6 days. This type of experimentation unfortunately requires more empirical experimentation than calculations, and may require multiple experiments to confirm.

Once a repeatable cell line protocol has been developed, the second experiment will be to determine the reaction of the CTX cells to both poly-lysine treated and natural or untreated surfaces. The cell reaction to the untreated surface is paramount for baseline biocompatibility comparisons, while treatment allows options for improving the biocompatibility. Ideally, we can include some of the new surfaces covered in (§4.2) and (§5.2). The experiment will begin by plating the E16-18 CTX cells on the tested substrates. We will then perform live and fixed cell AFM measurements each day of the test in order to monitor changes in the cell morphology, attachment, and differentiation quality. This research would be used to characterize the interaction of the neuron with the semiconductor surface or chemical treatments so as best to determine coatings for possible long term neural implants.

Another proposed biocompatibility test should include primary astrocytes and microglia in order to evaluate their reactivity with the surface of the semiconductors. As these are the two primary cells involved in glial scarring, establishing their reaction to the device material is paramount in determining the outcome of long term implantation within the CNS. Although we have found that the H4 cell line, which has been derived from a glial tumor, shows good biocompatibility and viability with 3C-SiC and NCD, this cell is derived from a cancerous tumor. We need to evaluate how normal, non-cancerous

cells would react to these materials. As was discussed in (§1.2.3), normal astrocytes and microglia cells experience physical and chemical changes when they are activated by damage to the CNS system or when they identify a foreign material. These changes eventually lead to the formation of the glial scar encapsulation around the material. Testing our material to evaluate if the glial cells actually react positively or negatively is paramount for the continuation of our biocompatibility study. We will use the primary glial cells for experiments similar to the experiments explained in (§3), and the discoveries made with these cells, will dictate if 3C-SiC or NCD are materials that potentially can be tested in vivo.

5.4 NAD Experimental Approach

Our first generation of NAD devices, NAD0, proved to be successful by activating neuron action potentials, but it is necessary to redesign the device to address many problems. NAD generation 1, or NAD1, will address these issues and involves the creation of three separate devices. The devices will be constructed and tested as part of the future research effort to achieve two-way communication between CNS neural cells and an electronic device. NAD1 will have smaller contacts 20 μm in diameter that are insulated from one another. Device packaging will be added to improve interface to both the signaling and measurement equipment.

The first NAD1 is an electrode device using Si as the base substrate material (Si-NAD). The device will consist of highly resistive Si, a layer of oxide to provide insulation, metal electrodes, and a secondary insulation layer, SU8, which is a

photosensitive biocompatible polymer. If necessary we can try to utilize another suitable insulating polymer as insulation between electrodes if SU8 is unavailable or does not fit the device requirements. The second NAD1 will be another electrode device similar in make to the first, but will instead utilize highly resistive 3C-SiC as a base material (SiC-NAD). Because 3C-SiC contains defects from the growth process, and normal growth at low pressure generates highly resistive material, this device will consist simply of 3C-SiC base, metal electrodes, and the SU8 insulation layer. A semiconductor material, like 3C-SiC, allows for another device with a different interface which is the metal-insulator-semiconductor capacitor device (MIScap or C-NAD). MIScaps interact with the neurons using electric fields to interact with ions in the extracellular media instead of through the complicated electrochemical reactions of a metal electrode in electrolytes as seen explained in (§ 1.3.4 and 1.3.5) and in Figure 4.6. The C-NAD device will be a MIScap device with conductive, n-type 3C-SiC as the base material which is then coated in electrically insulating NCD material. Metal is added to the backside of the device for connection of the MIScaps devices to the electronics, but the insulator remains uncoated at the cellular interface. All three devices will use gold, or platinum if available, as metal contacts. A thin layer of titanium will provide for contact adhesion. The NAD1's will have gold wires bound to the contact pads, which will be insulated by a coating of SU8. All device wiring will be gold bonded and soldered to insulated copper wiring which can be easily connected to external electronics which will be required for neural activation and signal processing. After the devices are created, they will be fully characterized

electrically in both air and within a buffered salt solution environment to confirm their functionality.

5.4.1 NAD Signal Reception from Neuron Action Potentials

The advantage of implantable neuronal prosthetics for the realization of BMI interfaces over non-invasive EEG type neuronal interfaces is the ability of implantable devices to have two-way communication with the CNS via the sending and receiving of electrical signals. Unlike signal transmission, the current density for signals transmitted by cells is in the tens of microvolt range; therefore electrical noise becomes a very important factor. Current microelectrode devices from Si or polyimide can receive signals from up to 100 μm away [14]. We would like to use the new NAD1 device as signal receiving as well as transmitting devices. An important consideration that may need to be included is external amplification and filtering of the signals due to the small 50–100 μV initial signal amplitudes. To determine these levels and set a baseline for the experiments, we will plate cortical cells onto the surfaces of the NAD1 and a control set within Petri dishes. A whole-cell voltage clamp will then be used to depolarize the membrane. Once depolarized, VGCC's will open allowing Ca^{2+} into the cell and the resulting currents will be recorded. Fortunately neuronal VGCC properties sitting on Petri dishes have been well characterized, and we have much to compare our results with [157-167]. The current characteristics of the neurons on the dishes will be used as a control and VGCC currents obtained from the neurons plated on the NADs will be compared to determine if the neuronal properties differ. The current characteristics will

also be utilized to determine the levels of signal amplification and filtration that would be required by the NAD1s to intercept signals from neurons.

The next stage for the NAD1 will be to combine the receiving and sending of signals to achieve two-way communication with the neural cell. A whole cell current clamp will again be used and the electrodes nearest to the cells will be connected to the amplification electronics and an oscilloscope. The current clamp will be used to elicit an action potential which will be subsequently received by the nearest electrode(s). The signals received on all of the NAD1s will be evaluated against the recorded patch clamp signals to establish signal integrity. The NAD1s will then be used to both elicit and receive a signal from a neuron simultaneously. For the electrode NAD1s (Si-NAD and SiC-NAD), two electrodes are selected as the cathode and anode signaling electrodes while a third electrode in the immediate area will be utilized as the signal recording site. The C-NAD device will require the use of only 2 sites, one capacitor for stimulation and the second for signal reception. The whole-cell current clamp will again be used with a neuron within the targeted signaling field to verify the action potentials. For the Si-NAD and SiC-NAD, a biphasic signal will be passed between the two electrodes, and the C-NAD will use a monophasic signal on its single capacitor. Once an action potential has been produced, the resulting signal will be recorded by both the clamp and the receiving electrode. The two signals will then be compared.

The generation of the proof of concept for a BMI device will be the next goal to evaluate the NAD1's BMI potentiality. The configuration, displayed in Figure 5.1, will use two NAD1s of similar electrical characteristics which will be selected and

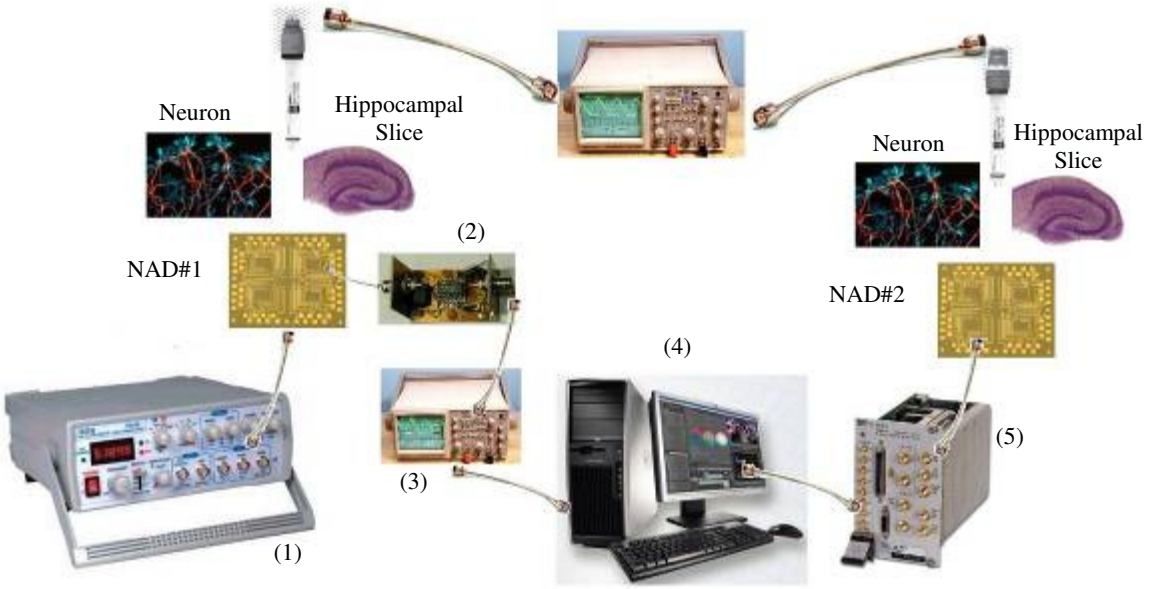

Figure 5.1: Cartoon representation of the proposed BMI that will be demonstrated by 2 NADs of the same material construction (NAD#1 and NAD#2). The NADs will be seeded with primary neuron cultures or organotypic hippocampal slice cultures and a signal generated from the wave generator (1) will be delivered to the NAD device to elicit an action potential from the cultured cells. An electrode intercepts the resulting action potential signal and transmits it to filtering and amplification electronics (2). An oscilloscope (3) is utilized to analyze and send the resulting signal to the control computer (4). The computer analyzes the input and activates another wave generator (5) to elicit an action potential on the second device. Whole-cell current clamp using glass electrodes will provide conformation of action potential activation (6).

interconnected through computer controlled electronics. The first NAD1 device will be connected to a wave generator, and the signal receiving NAD1 will be connected to amplification and filtration electronics. The amplification electronics will be connected to an oscilloscope which is controlled by a computer. Computer programs will be used to detect the signal spikes generated during an action potential, and then the signals will be characterized. The computer will send a signal to a second wave generator connected to the second NAD1 device. Neuron cultures will be cultured on both of the separated NAD1s, and whole-cell current clamps will be attached to target neurons on both devices.

The first NAD1 will be used to stimulate neurons, receive the subsequent signals and send signals to the computer. The computer will then send a corresponding signal to the second NAD1, which will stimulate the cultured neurons. The results will be verified through the whole-cell current clamps on both devices. The NAD1s will then be compared to determine differences between them.

The strength of implantable neuronal devices is fast two-way connection with target neurons, and the device mode for the NAD1s must be proven before clinical trials can be started. The final experiment detailed in (§.5.4.2) will also establish the ability of this type of platform to act as a bridge BMI device, an important factor for the restoration of individuals with brain damage and the resulting loss of motility. Also, this work will serve a secondary purpose in that they allow the electrical characterization of a MIScap device constructed from diamond and cubic silicon carbide which, to date, has only been proposed theoretically.

5.4.2 NAD2 Interaction with a Hippocampus Slice

The CNS medial temporal lobe, which includes the hippocampus, is important for cognitive function and memory formation. The underlying mechanisms believed to affect memory formation in this area of the brain involve changes in synaptic plasticity, specifically long term plasticity (LTP). The cornu ammonis (CA region), which is filled with densely packed pyramidal neurons not unlike those located within the cortex, is divided into four regions and is regularly used to examine LTP [168-170]. The CA1 region of the hippocampus displays several types of synaptic plasticity, including two

forms of LTP and at least one form of long-term depression (LTD) [168-171]. All forms can be initiated by electrical stimulation of varying degrees and are measured in the CA1 as an increase (LTP) or decrease (LTD) in the slope of field excitatory postsynaptic potentials (fEPSPs). Not surprisingly, lesions to the hippocampus impair performance on hippocampal-dependent tasks [172, 173]. Because lesions to the hippocampus disrupt normal learning and memory, a NAD that has the ability to be inserted into the hippocampus and reconnect a broken circuit would be of great benefit not only to the scientific community, but in neurology and neuroscience.

The eventual long-term goal is to build man-made neural networks to repair large portions of damaged brain and CNS tissue, and clearly the first step is to interact with a well established brain network model, such as organotypic hippocampal slice cultures. These hippocampal cultures maintain their tri-synaptic circuitry following plating and are electrically plastic, making them an appropriate tissue model for restoring brain function. Also, this higher level tissue contains both neurons and glial cells and will give us the opportunity to test the biocompatibility of our materials, specifically 3C-SiC and NCD, with more accuracy than the single cell *in vitro* methodology. A new NAD construction, NAD generation 2 which is based on the previous NAD generations, will be designed and fabricated to specifically interact with the hippocampal tri-synaptic neuronal network so as to provide a model for *ex vivo* communication. To establish a baseline comparison, we will plate hippocampal slices on the NAD2 and stimulate the CA2/3 Schaffer's collaterals using electrodes or capacitive devices on the NAD2. Subsequent fEPSPs will be

recorded from the stratum radiatum CA1 region of the hippocampal slice using the NAD2s and glass recording electrodes, which will act as a control for signal comparison.

The NAD2s will then be utilized to demonstrate the principal of a bridge BMI device. Hippocampal slices will be cut along the Schaffer's collaterals and through the dentate gyrus, creating two halves. The principal BMI operation will be utilized to allow communication of signals between the separated networks of the same hippocampus. Each part of the hippocampus will be placed on separate devices which are electrically connected through computer controlled electronics. A glass electrode will be placed in the CA1 region of the hippocampal slice to provide signal verification. The hippocampal slice containing the CA2/3 region will be stimulated with a biphasic stimulating electrode and the subsequent potentials will be recorded by the NAD2. The NAD2 will transmit the signals to the computer where they will be processed using the spike detection software. A secondary signal will be transmitted from the computer to the second NAD2 device. The second NAD2 device will then be used to excite a signal in the CA1 region of the separated hippocampal slice, and this signal will be confirmed through the glass electrode.

The final demonstration will use the NAD2 device not only to bridge between separated neurons, but to show that these devices can be utilized to perform physiological actions by eliciting LTP in organotypic hippocampal slice cultures. Hippocampal slices will be separated as previously described and plated on dual NAD2s connected to computer controlled electronics. First, we will establish baseline fEPSP responses to stimulation from a bipolar stimulating electrode. Following baseline, we will induce LTP

in the CA1 region of the separated hippocampal slice halves through high frequency stimulation (HFS) of the CA2/3 regions in the other half of the hippocampus. Following HFS, we will record fEPSPs again at baseline protocols for an additional 60 min. The NAD2 will be used to detect and transmit excitatory signals from the CA2/3 regions of the hippocampus to the computer. The second NAD2 will be used to receive signals from the computer and deliver those signals to the CA1 region of the hippocampus. This will not only demonstrate that NAD2s can act as a gate between severed circuits, but also become a physiological circuit itself in the CNS.

This is clearly the last critical hurdle before fully-functional NADs based on SiC are developed for clinical trials. Therefore, it is essential that a demonstration of device interaction with brain slices, such as the hippocampus, be made thus clearing the way for a continuation of this work. Successful demonstration of the therapeutic and two way communication ability of the NAD will pave the way for long-term animal implantation trials.

5.5 Conclusion

Many people currently are suffering from many problems that are the direct result of damage to their central nervous system. This is due to the fact that glial scarring, although protecting the undamaged part of the brain, does not readily allow the regeneration of synaptic pathways. However, it has been shown that microelectronic devices can be implanted that allow the reconnection of these synaptic pathways, thereby restoring functionality of the lost bodily functions. The major problem with these devices

is that they cause the generation of the very problem they are trying to resolve. The material of these devices activate astrocyes and microglia cells, the primary cells of the CNS immune system, and therefore cause the generation of another glial scar. Different materials need to be tested that will allow these devices to work indefinitely in the CNS.

This dissertation concentrated on two materials that may be the solution of this problem. 3C-SiC and NCD are two semiconductor materials that we have tested using *in vitro* methodology and have shown an excellent level of biocompatibility. One of these materials, 3C-SiC, was utilized to activate an action potential in neural cells. These two initial results show great promise for these materials for the development of a long term implantable neural prosthetic, however much work remains to be done before an *in vivo* device can be tested.

We have divided the research toward a neural implant device into three distinct experiments. The first set of proposed experiments is to further explore the interaction of the surface of SiC and NCD with the CNS cells through chemical modification. The modifications will inevitably lead to greater understanding of the molecular interactions between the proteins of the cells membranes and the molecular and atoms on the surface of the substrate. The second set of proposed experiments expands the biocompatibility testing to including primary cell lines. The immortalized cell lines used in the previous studies have been derived from cancerous tumors and may not be perfect models for cellular reactions to these materials. Healthy neurons, astrocytes, and microglia need to be tested with 3C-SiC and NCD before *in vivo* methods can be attempted. Finally, we propose using these materials to construct both electrode and field effect devices that will

interact with neurons. These new devices will not only activate action potentials, which we have already accomplished, but allow true two-way communication through the interception of action potential signals as well. The data collected from these devices will be used to model another generation of more complicated devices that can interact with a hippocampal tissue slice. Not only will this new device allow two-way communication, but will induce plasticity in the synaptic pathways of the hippocampal slices. If this research is successful, the material will be ready for *in vivo* testing and may be ready for clinical trials in the near future.

References

[1] J. Vidal, "Toward direct brain-computer communication", in *Annual Review of Biophysics and Bioengineering*, L. J. Mullins, Ed. Palo Alto, CA, USA: Annual Reviews, Inc., 1973, pp. 157 – 180.

[2] M. A. Lebedev, and M. A. L. Nicolelis, "Brain-machine interfaces: past, present and future", *Trends Neurosci.*, vol. 29, no. 9, pp. 536 – 546, 2006.

[3] K. D. Wise, A. M. Sodagar, Y. Yao, M. N. Gulari, G. E. Perlin, and K. Najafi, "Microelectrodes, microelectronics, and implantable neural microsystems", *Proceedings of the IEEE*, vol. 96,no. 7, pp. 1184 – 1202, 2008.

[4] C. Richards-Grayson, R. S. Shawgo, and A. M. Johnson, "A bioMEMS review: MEMS technology for physiologically integrated devices", *Proceedings of the IEEE*, vol. 92, no.1, pp. 6 – 21, 2004.

[5] T. James, M. S, Mannoor, and D. V. Ivanov, "BioMEMS – advancing the frontiers of medicine", *Sensors*, vol. 8, no. 9, pp. 6077 – 6107, 2008.

[6] D. F. Williams, "On the mechanisms of biocompatibility", *Biomaterials*, vol. 29, no. 20, pp. 2941 – 2953, 2008.

[7] S. C. Bayliss, L. D. Buckberry, P. J. Harris, and M. Tobin, "Nature of the silicon-animal cell interface", *Journal of Porous Materials*, vol. 7, no. 1 – 3, pp. 191 – 195, 2000.

[8] J. D. Birshall and A. W. Espie, "Biological implications of the interaction (via silanol groups) of silicon with metal ions" in *Ciba Foundation Symposium 121 - Silicon Biochemistry*, D. Evered and M. O'Connor, Eds. Chichester, UK: John Wiley & Sons, 1986, pp. 140 – 159.

[9] C. O'Neil, P. Jordan, T. Bhatt, and R. Newman, "Silica and oesophageal cancer" " in *Ciba Foundation Symposium 121 - Silicon Biochemistry*, D. Evered and M. O'Connor, Eds. Chichester, UK: John Wiley & Sons, 1986, pp. 214 – 230.

[10] L. L. Hench and J. Wilson, "Biocompatibility of silicates for medical use" " in *Ciba Foundation Symposium 121 - Silicon Biochemistry*, D. Evered and M. O'Connor, Eds. Chichester, UK: John Wiley & Sons, 1986, pp. 231 – 253.

[11] J. D. Birchall, and J. S. Chappel, "The chemistry of aluminum and silicon in relation to Alzheimer's disease", *Clin. Chem.*, vol. 34, no. 2, pp. 265 – 267, 1988.

[12] F. Beaudoin, M. Simard-Normandin, and M. Meunier, "Metallic contamination from wafer handling" in *Silicon Recombination Lifetime Characterization Methods*, D. C. Gupta, F. Bacher, and W. H. Hugh, Eds. West Conshohocken, PA, USA: American Society for Testing Materials, 1998, pp. 219 – 225.

[13] K. D. Wise, J. B. Angell, and A. Starr, "An integrated-circuit approach to extracellular microelectrodes", *IEEE Transactions on Bio-medical engineering* vol. BME-17, no. 3, pp. 238 – 247, 1970.

[14] S. F. Cogan, "Neural stimulation and recording electrodes", *Annu. Rev. Biomed*., vol. 10, pp. 275 – 309, August 2008.

[15] P. Fromherz, "Neuroelectronic interfacing: semiconductor chips with ion channels, nerve cells, and brain" in *Nanoelectronics and Information Technology: Advanced Electronic Materials and Novel Devices*, R. Waser, Ed., Berlin, DE: Wiley-VCH, 2003, pp. 781 – 810.

[16] X. Li, X. Wang, R. Bondokov, J. Morris, Y. H. An, and T. S. Sudarshan, "Micro/nanoscale mechanical and tribological characterization of SiC for orthopedic applications", *J. Biomed. Mater. Res. B Appl. Biomater.,* vol. 72, no. 2, pp. 353 – 361, 2005.

[17] U. Kalnins, A. Erglis, I. Dinne, I. Kumsars, and S. Jegere, "Clinical outcomes of silicon carbide coated stents in patient with coronary disease", *Med. Sci. Monit*., vol. 8, no. 2, pp. 16 – 20, 2002.

[18] S. Santavirta, M. Takagi, L. Nordsletten, A. Anttila, R. Lappalainen, and Y. T. Konttinen, "Biocompatibility of silicon carbide in colony formation test *in vitro*: A promising new ceramic THR implant coating material", *Arch. Orthop. Trauma Surg.*, vol. 118, no. 1 – 2, pp. 89 – 91, 1998.

[19] A. Naji and M. Harmand, "Cytocompatibility of two coating materials, amorphous alumina and silicon carbide, using human differentiated cell cultures", *Biomaterials*, vol. 12, no. 7, pp. 690 – 694, 1991.

[20] R. Yakimova, R. M. Petoral Jr, R. M. Yazdi, G. R. Vahlberg, C. L. Spetz, and A. K. Uvdal, "Surface functionalization and biomedical applications based on SiC" *J. Phys. D: Appl. Phys.*, vol. 40, pp. 6435 – 6442, October 2007.

[21] O. Kordina and S. E. Saddow. “Silicon carbide overview” in *Advances in Silicon Carbide Processing and Applications*, S. E. Saddow and A. Agarwal, Eds., Boston, MA, USA :Artech House, Inc., 2004, pp. 2 – 3, 7 – 8, 18.

[22] M. Reyes, Y. Shishkin, S. Harvey, and S. E. Saddow, “Development of a high-growth rate 3C-SiC on Si CVD process”, in *Mater. Res. Soc. Symp. Proc.*, vol. 911, 2006, pp. 79 – 84.

[23] S. E. Saddow, M. Lang, T. Dalibor, and G. Pensl. "Thermal capacitance spectroscopy of epitaxial 3C and 6H-SiC pn junction diodes grown side by side on a 6H-SiC substrate", *Appl. Phys. Lett.*, vol. 66, no. 26, pp. 3612 – 3614, 1995.

[24] K. Das, “Diamond and silicon carbide heterojunction bipolar transistor”, U. S. Patent 5,285,089, February 8, 1994.

[25] National Institute on Aging, “Inside the human brain”. [Online]. Available: http://www.nia.nih.gov/Alzheimers/Publications/Unraveling/Part1/inside.htm. [Accessed: May 20, 2009].

[26] C. N. Svendsen, "The amazing astrocyte", *Nature*, vol. 417, no. 2, pp. 29 – 32, 2002.

[27] M. Santello and A. Volterra, "Synaptic modulation by astrocytes via Ca^{2+} dependent glutamate release", *Neuroscience*, vol. 158, no. 1, pp. 253 – 259, 2009.

[28] K. J. Tomaselli, K. M. Neugebauer, J. L. Bixby, J. Lilien, and L. F. Reichardt, "N-cadherin and integrins: two receptor systems that mediate neuronal process outgrowth on astrocyte surfaces", *Neuron*, vol. 60, no. 3, pp. 398 – 399, 2008.

[29] T. Ishibashi, K. Dakin, B. Stevens, P. Lee, S. Kozlov, C. Stewart, and R. Fields, "Astrocytes promote myelination in response to electrical impulses". *Neuron*, vol. 49, no. 6, pp. 823 – 832, 2006.

[30] J. W. Fawcett and R. A. Asher, “The glial scar and central nervous system repair”, *Brain Research Bulletin*, vol. 49, no. 6, pp. 377 – 391, 1999.

[31] V. S. Polikov, P. A. Tresco, and W. M. Reichert, “Response of brain tissue to chronically implanted neural electrodes”, *J. of Neuroscience Methods,* vol. 148, pp. 1 – 18, August 2005.

[32] L. Olsen, “Regeneration in the adult nervous system: experimental repair strategies”, *Nature Medicine*, vol. 3, no. 12, pp. 1329 – 1335, 1997.

[33] A. L. Hodgkin and A. F. Huxley, “Currents carried by sodium and potassium ions through the membrane of the giant axon of Loligo”, *J. Phusiol. (Lond.)*, vol. 116, no. 4, pp. 449 – 472, 1952.

[34] A. L. Hodgkin and A. F. Huxley, “The components of membrane conductance in the giant axon of Loligo”, *J. Phusiol (Lond.)*, vol. 116, no. 4, pp. 473 – 496, 1952.

[35] A. L. Hodgkin and A. F. Huxley, “The dual effect of membrane potential on sodium conductance in the giant axon of Loligo”, *J. Phusiol (Lond.)*, vol. 116, no. 4, pp. 497 – 506, 1952.

[36] A. L. Hodgkin and A. F. Huxley, “A quantitative description of membrane current and its application to conduction and excitation in nerve”, *J. Phusiol (Lond.)*, vol. 117, no. 4, pp. 500 – 544, 1952.

[37] R. Plonsey, and R. C. Barr, “Action potential characteristics” in *Bioelectricity: A quantitative approach*, 2nd edition, New York, NY, USA: Kluwer Academic/ Plenum Publishers, 2000, pp. 125 – 127.

[38] D. W. Kennard, "Glass microcapillary electrodes used for measuring potential in living tissue," in *Electronic Apparatus for Biological Research*, P. E. K. Donaldson, Ed. New York, NY, USA: Academic Press, 1958, pp. 534 – 567.

[39] D. H. Hubel, “Tungsten microelectrode for recording from single units”, *Science*, vol. 125, no. 3247, pp. 549 – 550, 1957.

[40] D. A. Robinson, “The electrical properties of metal microelectrodes”, *Proc. IEEE*, vol. 56, no. 6, pp. 1065 – 1071, 1968.

[41] S. Martinoia, P. Massobrio, M. Bove, and G. Massobrio, "Cultured neurons coupled to microelectrode arrays: circuit models, simulations and experimental data", *IEEE Transactions on Biomedical Engineering*, vol. 51, no. 5, pp. 859 – 864, 2004.

[42] P. Fromherz, C.O. Muller, and R. Weis, "Neuron transistor: electrical transfer function measured by the patch-clamp technique," *Physical Review Letters*, vol. 71, no. 24, pp. 4079 – 4082, 1993.

[43] D. Braun, and P. Fromherz, “Fast voltage transients in capacitive silicon-to-cell stimulation detected with a luminescent molecular electronic probe”, *Phys. Rev. Lett.*, vol. 86, no. 13, pp. 2905 – 2908, 2001.

[44] I. Schoen, and P. Fromherz, “Extracellular stimulation of mammalian neurons through repetitive activation of Na^+ channels by weak capacitive currents on a silicon chip”, *J Neurophysiol,* vol. 100, pp. 346 – 357, May 2008.

[45] A. Stett, B. Müller, and P. Fromherz, "Two-way silicon-neuron interface by electrical induction," *Physical Review E*, vol. 55, no. 2, pp. 1779 – 1782, 1997.

[46] D. Feili, M. Schuettler, and T. Stieglitz, “Matrix-addressable, active electrode arrays for neural stimulation using organic semiconductors-cytotoxicity and pilot experiments *in vivo*”, *J. Neural Eng.*, vol. 5, no. 1, pp. 68 – 74, 2008.

[47] M. M. Moore-Jackson, S. G. Mason, and G. E Birch, “Analyzing trends in brain interface technology: A method to compare studies”, *Annals of Biomedical Engineering*, vol. 34, no. 5, pp. 859 – 878, 2006.

[48] R. Patrick, C. Ryan, C. Visser, J. Cruz, and J. Si, “Neurabotics: an integration of neurons, rats, and robots for advanced studies of brain-computer interface systems”, in *Proceedings of the 1st International IEEE EMBS Conference on Neural Engineering*, 2003, pp. 462 – 465.

[49] J. P Donoghue, “Connecting cortex to machines: recent advances in brain interfaces”, *Nature Neuroscience Supplement,* vol. 5 Suppl., pp. 1085 – 1088, November 2002.

[50] C. Guger, H. Ramoser, and G. Pfurtscheller, “Real-time EEG analysis with subject-specific spatial patterns for a brain-computer interface (BCI)”, *IEEE Transaction on Rehabilitation Engineering*, vol. 8, no. 4., pp. 447 – 456, 2000.

[51] M. Shiraishi and H. Sumiya, “Manipulator operation by using brain-wave signals” in *IEEE/ RSJ International Conference on Intelligent Robots and Systems*, 2005, pp. 3105 – 3110.

[52] M. M. Moore-Jackson and U. Dua, “A galvanic skin response interface for people with severe motor disabilities”, in *ACM SIGACCESS Access and Computing*, vol. 77 – 78, 2003, pp. 48 – 54.

[53] J. Wessberg, C. R. Stambaugh, J. D. Kralik, P. D. Beck, M. Laubach, J. K. Chapin, J. Kim, S. J. Biggs, M. A. Srinivasan, and M. A. L. Nicolelis, “Real-time prediction of hand trajectory by ensembles of cortical neurons in primates”, *Nature*, vol. 408, pp. 361 – 365, November 2000.

[54] W. Jensen and P. J. Rousche, “On variability and use of rat primary motor cortex responses in behavioral task discrimination”, *J. Neural Eng.*, vol. 3, no. 1, pp. L7 – L13, 2006.

[55] L. R. Hochberg, M. D. Serruya, G. M. Friehs, J. A. Mukand, M. Saleh, A. H. Caplan, A. Branner, D. Chen, R. D. Penn, and J. P. Donoghue, " Neuronal ensemble control of prosthetic devices by a human with tetraplegia", *Nature*, vol. 422, pp. 164 – 171, June 2006.

[56] R. J. S. Briggs, H. C. Eder, P. M. Seligman, R. S. C. Cowan, K. L. Plant, J. Dalton, D. K. Money, and J. F. Patrick, " Initial clinical experience with a totally implantable cochlear implant research device", *Otology & Neurotology*, vol. 29, no. 2, pp. 114 – 119, 2008.

[57] A. Y. Mogilner, A. L. Benabid, and A. R. Rezai, "Chronic therapeutic brain stimulation: history, current clinical indications, and future prospects", in *Bioelectromagnetic Medicine*. Paul J. Rosh, Ed. New York, NY, USA: Marcel Dekker, 2004, pp. 133 – 151.

[58] P. J. Rousche and R. A. Normann, "Chronic recording capability of the Utah intracortical electrode array in cat sensory cortex", *Journal of Neuroscience Methods*, vol. 82, no. 1, pp. 1 – 15, 1998.

[59] J. C. Williams, R. L. Rennaker, and D. R. Kipke, "Long-term neural recording characteristics of wire microelectrode arrays implanted in cerebral cortex" *Brain Res. Protoc*., vol. 4, no. 3, pp. 303 – 313, 1999.

[60] J. C. Williams, R. L. Rennaker, and D. R. Kipke, "Stability of chronic multichannel neural recordings: implications for a long-term neural interface", *Neurocomputing*, vol. 26 – 27, pp. 1069 – 1076, 1999.

[61] S. A. Boppart, B. C. Wheeler, and C. S. Wallace, "A flexible perforated microelectrode array for extended neural recordings", *IEEE Trans. Biomed. Eng*., vol. 39, no. 1, pp. 37 – 42, 1992.

[62] P. J. Rousche, D. S. Pellinen, D. P. Pivin Jr., J. C. Williams, R. J. Vetter, and D. R. Kipke, "Flexible polyimide-based intracortical electrode arrays with bioactive capability", *IEEE Trans. Biomed. Eng.*, vol. 48, no. 3, pp. 361 – 371, 2001.

[63] A. Jackson and E. E. Fetz, "Compact movable microwire array for long-term chronic unit recording in cerebral cortex of primates", *J. Neurophysiol.*, vol. 98, pp. 3109 – 3118, September 2007.

[64] K. K. Lee, J. P. He, A. Singh, S. Massia, G. Ehteshami, B. Kim, B. Kima, and G. Rauppc, "Polyimide based intracortical neural implant with improved structural stiffness", *J. Micromech. Microeng*., vol. 14, no. 1, pp. 32 – 37, 2004.

[65] J-M. Hsua, P. Tathireddy, L. Rieth, A. R. Normann, and F. Solzbacher, "Characterization of a-SiC_x:H thin films as an encapsulation material for integrated silicon based neural interface devices", *Thin Solid Films*, vol. 516, no. 1, pp. 34 – 41, 2007.

[66] Cree Inc., [Online]. Available: http://www.cree.com, [Accessed: May 20, 2009].

[67] C. M. Tanner, C. Frewin, S. E. Saddow, and J. P. Chang, "Electrical performance of Al_2O_3 gate dielectric films deposited by atomic layer deposition on 4H-SiC", *Appl. Phys. Lett.*, vol. 91, no. 20, pp. 203510-1 – 203510-3, 2007.

[68] P. G. Neudeck, D. J. Larkin, J. E. Starr, J. A. Powell, C. S. Salupo, and L. G. Matus, "Electrical properties of epitaxial 3C- and 6H-SiC p-n junction diodes produced side-by-side on 6H-SiC substrates", *IEEE Transactions on Electron Devices*, vol. 41, no. 5, pp. 826 – 835, 1994.

[69] P. G. Neudeck, A. J. Trunek, D. J. Spry, J. A. Powell, H. Du, M. Skowronski, X. R. Huang, and M. Dudley, "CVD growth of 3C-SiC on 4H/6H mesas", *Chemical Vapor Deposition*, vol. 12, no. 8 – 9, pp. 531 – 540, 2006.

[70] C. A. Zorman, M. Mehregany, "Materials for microelectromechanical systems", in *The MEMS Handbook: Introduction and Fundamentals*, M. Gad-el-Hak, Ed., Boca Raton, FL, USA:CRC Press, 2001, pp. 15 – 23.

[71] Y. Goldberg, M. Levinshtein, and S. Rumyantsev, "Silicon carbide (SiC)", in *Properties of Advanced Semiconductor Materials: GaN, AIN, InN, BN, SiC, SiGe*, M E. Levinshtein, S. L. Rumyantsev, M. S. Shur, Eds., New York, NY, USA: John Wiley and Sons, 2001, pp. 93 – 147.

[72] J. Deva Reddy, A. A. Volinsky, C. Frewin, C. Locke, and S. E. Saddow, "Mechanical properties of single and polycrystalline SiC thin films" in *Mat. Res. Soc. Symp. Proc.*, vol. 1049, 2008, pp. AA03 – AA06.

[73] M. Kuhn and D. Silversmith, "Ionic contamination and transport of mobile ions in MOS structures", *J. Electrochem. Soc.*, vol. 118, no. 6, pp. 966 – 970, 1971.

[74] S. Raider, L. Gregor, and R. Flitsch, "Transfer of mobile ions from aqueous solutions to the silicon dioxide surface", J. *Electrochem. Soc.*, vol. 120, no. 3, pp. 425 – 431, 1973.

[75] E. H. Snow, A. S. Grove, B. E. Deal, and C. T. Sah, "Ion transport phenomena in insulating films", *J. Appl. Phys.*, vol. 36, no. 5, pp. 1664 – 1673, 1965.

[76] B. G. Streetman and S. Banerjee, *Solid State Electronic Devices*, Upper Saddle River, NJ, USA: Prentice Hall, 2000, pp. 274 – 275.

[77] E. M. Carlisle, "Silicon as an essential trace element in animal nutrition" in *Ciba Foundation Symposium 121 - Silicon Biochemistry*, D. Evered and M. O'Connor, Eds., Chichester, UK: John Wiley & Sons, 1986, pp. 123 – 139.

[78] M. Amaral, A. G. Dias, P. S. Gomes, M. A. Lopes, R. F. Silva, J. D. Santos, and M. H. Fernandes, "Nanocrystalline diamond: *In vitro* biocompatibility assessment by MG63 and human bone marrow cells cultures", *J. Biomed. Mater. Res. A*, vol. 87, no. 1, pp. 91 – 99, 2008.

[79] Diamond at Work™, "Properties of Diamond", Knowledge Base: Properties. [Online]. Available: http://www.diamondatwork.com, [Accessed: May 20, 2009].

[80] Kobelco, Kobe Steel, Ltd" Comparison of materials properties between diamond and other semiconducting materials", Properties of Diamond. [Online]. Available: http://www.kobelco.co.jp/p047/products/np0802e/np08022e.htm, [Accessed: May 20, 2009].

[81] Diamond Engineering, "Material properties for MOS cap EM simulation", Microwave Library: MOS Cap EM Models [Online]. Available: http://www.diamondeng.net/library/MOScapEMmodels.pdf, [Accessed: May 20, 2009].

[82] MEMSnet®, "Material: Silicon Dioxide (SiO2), film", Material: Silicon Dioxide (SiO2), film. [Online]. Available: http://www.memsnet.org/material/silicondioxidesio2film, [Accessed: May 20, 2009].

[83] F. K. de Theije, O. Roy, N. J. van der Laagand, and W. J. P. van Enckevort, "Oxidative etching of diamond", *Diamond and Related Materials*, vol. 9, no. 3 – 6, pp. 929 – 934, 2000.

[84] F. Fang, C. A. Hewett, M. G. Fernandez, and S. S. Lau, "Ohmic contacts formed by ion mixing in the Si-Diamond system", *IEEE Transactions on Electronic Devices*, vol. 36, no. 9, pp. 1783 – 1786,1989.

[85] Y. M. Tairov, V. F. Tsvetkov, M. A. Chernov, and V. A. Tarantes, "Investigation of phase transformations and polytype stability of β-SiC", *Phys. Stat. Sol. (a)*, vol. 43, no. 1, pp. 363 – 369, 1977.

[86] W. G. Spitzer, D. A. Kleinman, and C. J. Frosch, "Infrared properties of cubic silicon carbide films", *Physical Review*, vol. 113, no. 1, pp. 133 – 136, 1959.

[87] H. Nakashima, T. Sugano, and H. Yanai, "Epitaxial growth of SiC film on silicon substrate and its crystal structure", *Jap. J. of Appl. Phys.*, vol. 5, no. 10, pp. 874 – 878, 1966.

[88] S. Nishino, H. Suhara, H. Ona, and H. Matsunami, "Epitaxial growth and electric characteristics of cubic SiC on silicon", *J. Appl. Phys.*, vol. 61, no. 10, pp 4889 – 4893, 1987.

[89] J. Yun, T. Takahashi, Y. Ishida, and H. Okumu, "Dependence of stacking fault and twin densities on deposition conditions during 3C-SiC heteroepitaxial growth on on-axis Si(001) substrates", *Journal of Crystal Growth*, vol. 291, no. 1, pp. 140 – 147, 2006.

[90] S. Mahajan and K. S. Sree Harsha, "3.3 Structural characteristics of defects" in *Principals of Growth and Processing of Semiconductors*, Boston, MA, USA: McGraw Hill Companies Inc., 1999, pp. 83 – 113.

[91] Y. Sun, T. Miyasato, J. K. Wigmore, N. Sonoda, and Y. Watari, "Characterization of 3C-SiC films grown on monocrystalline Si by reactive hydrogen plasma sputtering", *J. Appl. Phys.*, vol. 82, no. 5, pp 2234 – 2341, 1997.

[92] J. P. Li and A. J. Steckl, "Nucleation and void formation mechanisms in SiC thin film growth on Si by carbonization", *J. Electrochem. Soc.*, vol. 142, no. 2, pp. 634 – 641, 1995.

[93] V. Papaioannou, H. Moller, M. Rapp, L. Vogelmeier, M. Eickhoff, G. Krotz, and J. Stoemenos, "The evolution of cavities in Si at the 3C-SiC:Si interface during 3C-SiC deposition by LPCVD", *Materials Science and Engineering B*, vol.61 – 62, pp. 539 – 543, July 1999.

[94] O. Kordina, L.-O. Bjorketun, A. Henry, C. Hallin, R. C. Glass, L. Hultman, J.-E. Sundgren, and E. Janen, "Growth of 3C-SiC on on-axis (100)Si substrates by chemical vapor deposition", *Journal of Crystal Growth*, vol. 154, no. 3, pp. 303 – 314, 1995.

[95] C. Frewin, "Design and Implementation of a 200 mm 3C-SiC CVD Reactor", M.S.E.E. Thesis, University of South Florida, Tampa, FL, 2006.

[96] A. Severino, C. Frewin, R. Anzalone, C. Bongiorno, P. Fiorenza, G. D'Arrigo, F. Giannazzo, G. Foti, F. La Via and S. E. Saddow, "Growth of 3C-SiC on Si: Influence of process pressure," in *Materials Science Forum*, vols. 600 – 603, 2009, pp 211 – 214.

[97] C. Locke, R. Anzalone, A. Severino, C. Bongiorno, G. Litrico, F. La Via, and S. E. Saddow, "High quality single crystal 3C-SiC(111) films grown on Si(111)", presented in *European Conf. on SiC and Related Materials*, September 2008, Tu1-2.

[98] G. F. McLane and J. R. Flemish, "High etch rates of SiC in magnetron enhanced SF plasmas", *Appl. Phys. Lett.*, vol. 68, no. 26, pp. 3755 – 3757, 1996.

[99] G. Carter, J. B. Casady, M. Okhuysen, J. D. Scofield, and S. E. Saddow, "Preliminary investigation of 3C-SiC on silicon for biomedical applications," in *Materials Science Forum*, vols. 338 – 342, 2000, pp. 1149 – 1152.

[100] C. Locke, G. Kravchenko, P. Waters, J. Deva Reddy, A. A. Volinsky, C. L. Frewin, and S. E. Saddow, "3C-SiC films on Si for MEMS applications: Mechanical Properties," in *European Conf. on SiC and Related Materials*, September 2008, Late News.

[101] M. Reyes, M. Waits, S. Harvey, Y. Shishkin, B. Geil, J.T. Wolan and S.E. Saddow, "Growth of 3C-SiC on Si Molds for MEMS applications," in *Materials Science Forum*, vols. 527 – 529, 2006, pp. 307 – 313.

[102] S. A. Rosli, A. A. Aziz, and H. A. Hamid, "Characteristics of RIE SF_6/ O_2/ Ar plasmas on n-silicon etching", in *IEEE International Conference on Semiconductor Electronics*, 2006, pp. 851 – 859.

[103] S. Frederico, C. Hilbert, R. Fritschi, P. Fluckiger, P. Renaud, and A. M. Ionescu, "Silicon sacrificial layer dry etching (SSLDE) for free-standing RF MEMS architectures", in *The Sixteenth Annual IEEE International Conference on Micro Electro Mechanical Systems*, 2003, pp 570 – 573.

[104] T. Shimizu, Y. Ishikawa, and N. Shibata, "Epitaxial growth of 3C-SiC on thin silicon-on-insulator substrate by chemical vapor deposition using alternating gas supply", *Jpn. J. Appl. Phys.*, vol. 39, no. 6B, pp. L617 – L619, 2000.

[105] R. L. Myers, S. E. Saddow, S. Rao, K. D. Hobart, M. Fatemi, and F. J. Kub, "Development of 3C-SiC SOI structures using Si on polycrystalline SiC wafer bonded substrates," in *Materials Science Forum*, vols. 457 – 460, 2004, pp. 1511 – 1514.

[106] G. Harbeke, L. Krausbauer, E. F. Steigmeier, A. E. Widmer, H. F. Kappert, G. Neugebauer, "Growth and physical properties of LPCVD polycrystalline silicon films", *J. Electrochem. Soc.*, vol. 131, no. 1 – 2, pp. 675 – 682, 1984.

[107] J. Yang, H. Kahn, A.-Q. He, S. M. Phillips, and A. H. Heuer, "A new technique for producing large-area as-deposited zero-stress LPCVD polysilicon films: the MultiPoly process", *IEEE Journal of Microelectromechanical Systems*, vol. 9, no. 4, pp. 485 – 494, 2000.

[108] C. Locke, C. Frewin, J. Wang, and S. E. Saddow, "Growth of single crystal 3C-SiC(111) on a poly-Si seed layer," in *European Conf. on SiC and Related Materials,* 2008, WeP-5.

[109] S. Dogan, D. Johnstone, F. Yun, S. Sabuktagin, J. Leach, A. A. Baski, H. Morkoç, G. Li, and B. Ganguly, "The effect of hydrogen etching on 6H-SiC studied by temperature-dependent current-voltage and atomic force microscopy", *Appl. Phys. Lett.*, vol. 85, no. 9, pp. 1547 – 1549, 2004.

[110] U. Starke, "Atomic structure of SiC surfaces" in *Silicon Carbide, Recent Major Advances*, W. J. Choyke, H. Matsunami, and G. Pensl, Eds., Berlin, DE: Springer Verlag, 2004, pp. 281 – 316.

[111] C. Coletti, C. L. Frewin, A. M. Hoff and S. E. Saddow, "Electronic passivation of 3C-SiC(001) via hydrogen treatment", *Electrochemical and Solid-State Letters*, vol. 11, no. 10, pp. H285 – H287, 2008.

[112] S. Soubatch, S. E. Saddow, S. P. Rao, W. Y. Lee, M. Konuma, and U. Starke, "Structure and morphology of 4H-SiC wafer surfaces after H_2-etching", *Mater. Sci. Forum*, v*ols.* 483 – 485, 2005, pp. 761 – 764.

[113] C. Coletti, S. E. Saddow, C. L. Frewin, M. Hetzel, C. Virojanadara, and U. Starke, "Surface studies of hydrogen etched 3C-SiC(001) on Si (001)", *Appl. Phys. Lett*. 91, no. 6, pp. 061914 –060916, 2007.

[114] A. Severino, G. D'Arrigo, C. Bongiorno, S. Scalese, F. La Via, and G. Foti, "Thin crystalline 3C-SiC layer growth through carbonization of differently oriented Si substrates", *J. of Applied Physics,* vol. 102, no. 2, pp. 23518 – 23520, 2007.

[115] H. Yoshikawaa, C. Morela, and Y. Kogab, "Synthesis of nanocrystalline diamond films using microwave plasma CVD", *Diamond and Related Materials*, vol. 10, no. 9 – 10, , pp. 1588 – 1591, 2001.

[116] L. Olsen, "Regeneration in the adult nervous system: experimental repair strategies", *Nature Medicine*, vol. 3, no. 12, pp. 1329 – 1335, 1997.

[117] C. C. Stichel and H. W. Müller, "The CNS lesion scar: new vistas on an old regeneration barrier", *Cell Tissue Res.*, vol. 294, no. 1, pp. 1 – 9, 1998.

[118] C. S. Bjornsson, S. J. Oh, Y. A. Al-Kofahi, Y. J. Lim, K. L. Smith, J. N. Turner, S. De, B Roysa, W Shain, S. J. Kim, "Effects of insertion conditions on tissue strain and vascular damage during neuroprosthetic device insertion", *J. Neural Eng.* 3, pp. 196 – 207, September 2006.

[119] R. G. Richards, "The effect of surface roughness on fibroblast adhesion *in vitro*", *Injury*, vol. 27, no. Supl. 3, pp. S-C38 – S-C48, 1996.

[120] T. V. Kumari, U. Vasudev, A. Kumar, and B. Menon, "Cell surface interactions in the study of biocompatibility", *Trend Biomater. Artif. Organs*, vol. 15, no. 2, pp. 37 – 41, 2002.

[121] C. S. Goodman, "Mechanisms and molecules that control growth cone guidance", *Annu. Rev. Neurosci.*, vol. 19, pp. 341 – 77, March 1996.

[122] J. Hirrlinger, S. Hulsmann, and F. Kirchhoff, "Astroglial processes show spontaneous motility at active synaptic terminals in situ", *European Journal of Neuroscience*, vol. 20, no. 8, pp. 2235 – 2239, 2004.

[123] D. J. Solecki, E.-E. Govek, and M. E. Hatten, "mPar6α controls neuronal migration", *The Journal of Neuroscience*, vol. 26, no. 42, pp. 10624 – 10625, 2006.

[124] C. Coletti, M. J. Jaroszeski, A. Pallaoro, A. M. Hoff, S. Iannotta, and S. E. Saddow, "Biocompatibility and wettability of crystalline SiC and Si surfaces", in *IEEE EMBC Proceedings*, vol. 22 – 26, 2007, pp.5849 – 5852.

[125] T. Mosmann, "Rapid colorimetric assay for cellular growth and survival: application to proliferation and cytotoxicity assays", *Journal of immunological methods*, vol. 65, no. 1 – 2, pp. 55 – 63, 1983.

[126] C. Coletti, "Silicon carbide biocompatibility, surface control and electronic cellular interaction for biosensing applications", Ph.D.E.E. dissertation, University of South Florida, Tampa, FL, 2007.

[127] C. A. Easley IV, C. M. Brown, A. F. Horwitz, and R. M. Tombes, "CaMK-II promotes focal adhesion turnover and cell motility by inducing tyrosine dephosphorylation of FAK and paxillin", *Cell Motility and the Cytoskeleton*, vol. 65, no. 8, pp.662 – 674, 2008.

[128] M. J. Booth, R. Ju, and T. Wilson, "Spectral confocal reflection microscopy using a white light source", *Journal of the European Optical Society*, vol. 3, pp. 08026-1 – 08026-6, August 2008.

[129] Y. Wakamatsu, X. Zhao, C. Jin, N. Day, M. Shibahara, N. Nomura, T. Nakahara, T. Murata, K. K. Yokoyama, "Mannosylerythritol lipid induces characteristics of neuronal differentiation in PC12 cells through an ERK-related signal cascade", *Eur. J. Biochem.,* vol. 268, no. 2, pp. 374 – 383, 2001.

[130] P. R. Gordon-Weeks, "Microtubules and growth cone function", *J. Neurobiol.* vol. 58, no. 1, pp. 70 – 83, 2003.

[131] A. Rouhi, "Contemporary biomaterials", *C & EN,* vol. 77, no. 3, pp. 51 – 59, 1999.

[132] K. H. Kim, J.-S. Cho, D.-J. Choi, S.-K Koh, "Hydrophilic group formation and cell culturing on polystyrene Petri-dish modified by ion-assisted reaction", *Nuclear Instruments and Methods in Physics Research B*. vol. 175 – 177, pp. 542 – 547, 2001.

[133] M. Bergkvist, J. Carlsson, J. Oscarsson, "Surface-dependent conformations of human plasma fibronectin adsorbed to silica, mica, and hydrophobic surfaces, studied with use of Atomic Force Microscopy", *J. Biomed. Mater. Res. A*., vol. 64, no. 2, pp. 349 – 356, 2003.

[134] P. Clark, S. Britland, and P. Connolly, "Growth cone guidance and neuron morphology on micropatterned laminin surfaces", *Journal of Cell Science*, vol. 105, no. 1, pp. 203-212, 1993.

[135] E. G. Fine, R. F. Valentini, R. Bellamkonda, and P. Aebischer, "Improved nerve regeneration tooth piezoelectric vinylidenefluoride-truoroetlene copolymer guidance channels", *Biomaterials*, vol. 12, no. 8, pp. 775 – 780, 1991.

[136] S. A. Makohliso, R. F. Valentini, and P. Aebischer, "Magnitude and polarity of a fluoroethylene propylene electrical substrate charge influences neurite outgrowth *in vitro" J. Biomed. Mater. Res.*, vol. 27, no. 8, pp. 1075 – 1085, 1993.

[137] T.-H. Young and C.-H. Hung, "Change in electrophoretic mobility of PC12 cells after culturing on PVA membranes modified with different diamines", *J. Biomed. Mater. Res. A*., vol. 67, no. 4, pp. 1238 – 1244, 2003.

[138] C. E. Schmidt, V. R., Shastri, J. P. Vacanti, and R. Langer, "Stimulation of neurite outgrowth using an electrically conducting polymer", *Proc. Natl. Acad. Sci.*, vol. 94, pp. 8948 – 8953, 1997.

[139] A. Sklodowska, M. Wozniak, R. Matlakowska, "The method of contact angle measurements and estimation of work of adhesion in bioleaching of metals", *Biol. Proc.*, vol. 1, no. 3, pp. 114 – 121, 1999.

[140] L. Ostrovskaya, V. Perevertailo, V. Ralchenko, A. Saveliev, and V. Zhuravlev, "Wettability of nanocrystalline diamond films", *Diamond and Related Materials,* vol. 16, no. 12, pp. 2109 – 2113, 2007.

[141] Cree Inc, "MAT-CATALOG", Materials: Products. [Online]. Available: http:// www.cree.com , [Accessed: May 20, 2009].

[142] M. Stutzmann, J. A. Garrido, M. Eickhoff, and M. S. Brandt, "Direct biofunctionalization of semiconductors: A survey", *Physica Status Solidi (a)*, vol. 203, no. 14, pp. 3424 – 3437, 2006.

[143] S. J. Schoell, M. Hoeb, I. D. Sharp, W. Steins, M. Eickhoff, M. Stutzmann, and M. S. Brandt, "Functionalization of 6H-SiC surfaces with organosilanes", *Appl. Phys. Lett.*, vol. 92, p. 153301-1 – 153301-3, 2008.

[144] G. W. Trucks, K. Raghavachari, G. S. Higashi, and Y. J. Chabal, "Mechanism of HF etching of silicon surfaces: A theoretical understanding of hydrogen passivation", *Phys. Rev. Lett*., vol. 65, no. 4, pp. 504 – 507, 1990.

[145] H. Bender, S. Verhaverbeke, M. Caymax, O. Vatel, and M. M. Heyns, J., "Surface reconstruction of hydrogen annealed (100) silicon", *J. Appl. Phys*., vol. 75, no. 2, pp. 1207 – 1209, 1994.

[146] M. R. Linford, C. E. D. Chidsey, "Alkyl monolayers covalently bonded to silicon surfaces", *J. Am. Chem. Soc*., vol. 115, no. 26, pp. 12631 – 12632, 1993.

[147] M. Hu, S. Noda, T. Okubo, Y. Yamaguchi and H. Komiyama, "Structure and morphology of self-assembled 3-mercaptopropyltrimethoxysilane layers on silicon oxide", *Applied Surface Science*, vol. 181, no. 4, pp. 307 – 316, 2001.

[148] H. Tsuchida, I. Kamata, and K. Izumi, "Infrared attenuated total reflection spectroscopy of 6H–SiC(0001) and (000-1) surfaces", *J. Appl. Phys*., vol. 85, no. 7, pp. 3569 – 3575, 1999.

[149] I. D. Sharp, S. J. Schoell, M. Hoeb, M. S. Brandt, and M. Stutzmann, "Electronic properties of self-assembled alkyl monolayers on Ge surfaces" *Appl. Phys. Lett*., vol. 92, pp. 223306-1 – 223306-3, 2008.

[150] L. A. Lipkin and J. W. Palmour, "Insulator investigation on SiC for improved reliability," *IEEE Trans. Electron* Devices, vol. 46, no. 3, pp. 525 – 532, 1999.

[151] P.-H. Puech1, A. Taubenberger, F. Ulrich, M. Krieg, D. J. Muller, and C.-P. Heisenberg, "Measuring cell adhesion forces of primary gastrulating cells from zebrafish using atomic force microscopy", *Journal of Cell Science*, vol. 118, no. 18, pp. 4199 – 4206, 2005.

[152] Y. F. Dufrêne and P. Hinterdorfer, "Recent progress in AFM molecular recognition studies", *Pflugers Arch. Eur J Physiol*, vol. 456, no. 1, pp. 237 – 245, 2008.

[153] J. E. Huettner and R. W. Baughman, "Primary culture of identified neurons from the visual cortex of postnatal rats", *The Journal of Neuroscience*, vol. 6, no. 10, pp. 3044 – 3060, 1986.

[154] S. Cronier, H. Laude, and J.-M. Peyrin, "Prions can infect primary cultured neurons and astrocytes and promote neuronal cell death", *Proc. Natl. Acad. Sci. USA*, vol. 101, no. 33, pp. 12271 – 12276, 2004.

[155] T. B. Toha, M. J. Chena, A. Armugama, Z. F. Pengb, Q.-T. Lia, K. Jeyaseelana, and N. S. Cheung, "Antioxidants: promising neuroprotection against cardiotoxin-4b-induced cell death which triggers oxidative stress with early calpain activation", *Toxicon*, vol. 51, no. 6, pp. 964 – 973, 2008.

[156] O. P. Hamill, A. Marty, E. Neher, B. Sakmann, and F. J. Sigworth, "Improved patch-clamp techniques for high-resolution current recording from cells and cell-free membrane patches", *Pflugers Arch. Eur. J. Physiol.*, vol. 391, no. 2, pp. 85 – 100, 1981.

[157] P. W. Landfield, L. W. Campbell, S. Y. Hao, and D. S. Kerr, "Aging-related increases in voltage-sensitive, inactivating calcium currents in rat hippocampus. Implications for mechanisms of brain aging and Alzheimer's disease," *Ann. N.Y. Acad. Sci.*, vol. 568, pp. 95 – 105, December 1989.

[158] O. Thibault, N. M. Porter, P. and W. Landfield, "Low Ba^{2+} and Ca^{2+} induce a sustained high probability of repolarization openings of L-type Ca^{2+} channels in hippocampal neurons: physiological implications", *Proc. Natl. Acad. Sci. USA*, vol. 90, pp. 11792 – 11796, December 1993.

[159] L. W. Campbell, Su-Yang Hao, Olivier Thibault, Eric M. Blalock, and Philip W. Landfield, "Aging changes in voltage-gated calcium currents in hippocampal CA1 neurons", *J. Neurosci.*, vol. 16, no. 19, pp. 6286 – 6295, 1996.

[160] O. Thibault and P. W. Landfield, "Increase in single L-type calcium channels in hippocampal neurons during aging", *Science*, vol. 272, no 5264, pp. 1017 – 1020, 1996.

[161] N. M. Porter, O. Thibault, V. Thibault, K.-C. Chen, and P. W. Landfield, "Calcium channel density and hippocampal cell death with age in long-term culture", *J. Neurosci.,* vol. 17, no. 14, pp. 5629 – 5639, 1997.

[162] O. Thibault, R. Hadley, and P. W. Landfield, "Elevated Postsynaptic $[Ca^{2+}]_i$ and L-type calcium channel activity in aged hippocampal neurons: relationship to impaired synaptic plasticity", *J. Neurosci.*, vol. 21, no. 24, pp. 9744 – 9756, 2001.

[163] O. Thibault, M. L. Mazzanti, E. M. Blalock, N. M. Porter and P. W. Landfield, "Single-channel and whole-cell studies of calcium currents in young and aged rat hippocampal slice neurons", *J. of Neuroscience Methods*, vol. 59, no. 1, pp. 77 – 83, 1995.

[164] R. W. Tsien, D. Lipscombe, D. V. Madison, K. R. Bley, and A. P. Fox, "Multiple types of neuronal calcium channels and their selective modulation", Trends Neurosci., vol. 11, no. 10, pp. 431 – 438, 1988.

[165] B. P. Bean, "Classes of calcium channels in vertebrate cells", *Annu Rev Physiol*, vol. 51, pp. 367 – 384, March 1989.

[166] W. A. Catterall, M. J. Seagar, M. Takahashi, and K. Nunoki, "Molecular properties of voltage-sensitive calcium channels", *Adv. Exp. Med. Biol.*, vol. 255, no. 1, pp. 101 – 109, 1989.

[167] W. A. Catterall, M. J. Seagar, M. Takahashi, and K. Nunoki, "Molecular properties of dihydropyridine-sensitive calcium channels", *Ann N Y Acad Sci*, vol. 560, no. 1, pp. 1 – 14, 1989.

[168] L. M. Grover and T. J. Teyler, "Two components of long-term potentiation induced by different patterns of afferent activation", *Nature*, vol. 347, no. 6292, pp. 477 – 479, 1990.

[169] C. M. Norris, S. Halpain, and T. C. Foster, "Reversal of age-related alterations in synaptic plasticity by blockade of L-type Ca^{2+} channels", *J. Neurosci.*, vol. 18, no. 9, pp. 3171 – 3179, 1998.

[170] T. V. Bliss and T. Lomo, "Long-lasting potentiation of synaptic transmission in the dentate area of the anaesthetized rabbit following stimulation of the perforant path", *J. Physiol.,* vol. 232, pp. 331 – 356, July 1973.

[171] C. M. Norris, D. L. Korol, and T. C. Foster, "Increased susceptibility to induction of long-term depression and long-term potentiation reversal during aging", *J. Neurosci.*, vol. 16, no. 17, pp. 5382 – 5392, 1996.

[172] G. Winocur and M. Moscovitch, "Hippocampal and prefrontal cortex contributions to learning and memory: analysis of lesion and aging effects on maze learning in rats ", *Behav. Neurosci.*, vol. 104, no. 4, pp. 544 – 551, 1990.

[173] G. Winocur, "A comparison of normal old rats and young adult rats with lesions to the hippocampus or prefrontal cortex on a test of matching-to-sample", *Neuropsychologia*, vol. 30, no. 9, pp. 769 – 781, 1992.

Bibliography

I. B. Levitan and L. K. Kaczmarek, *The Neuron: Cell and Molecular Biology*, 3rd edition, New York, NY, USA: Oxford University Press, 2002.

D. Purves, G. J. Augustine, D. Fitzpatrick, W. C. Hall, A-S. LaMarta, J. O. McNamara, and L. E. White, Eds., *Neuroscience*, fourth edition, Sunderland, MA, USA: Sinauer Associates, Inc., 2008.

R. Plonsey and R. C. Barr, *Bioelectricity: A Quantitative Approach*, New York, NY, USA: Kluwer Academic / Plenum Publishers, 2000.

About the Author

Christopher Leroy Frewin was born on November 25th, 1970 in Salt Lake City, Utah. He started at the University of South Florida in the summer of 2002 and earned both his bachelor's and master's degree December 2007. During his graduate work, he has collaborated and worked at the Max-Planck-Institut (MPI) of Stuttgart (DE) and the Instituto per la Microelettronica e Microsistemi - Consiglio Nazionale Delle Ricerche (IMM-CNR) in Catania, Italy. He traveled to and performed research at both of these institutions two times each. He is the first author of two peer-reviewed journal papers (one in the *Journal of Molecular Recognition* and the other is in *Journal of Crystal Growth*), is co-author of three other journal papers, and has presented and written articles in proceedings for numerous conferences. A provisional patent, serial no. 61/187808, based on the results of this work has been filed with the US patent office.